

FLUID-STRUCTURE INTERACTION OF STEADY AND PULSATING FLOW THROUGH  
A COLLAPSIBLE THIN-WALLED VESSEL

A Thesis  
Submitted to the Graduate Faculty  
of the  
North Dakota State University  
of Agriculture and Applied Science

By

Sifat Karim Chowdhury

In Partial Fulfillment of the Requirements  
for the Degree of  
MASTER OF SCIENCE

Major Department:  
Mechanical Engineering

February 2024

Fargo, North Dakota

North Dakota State University  
Graduate School

---

**Title**

FLUID-STRUCTURE INTERACTION OF STEADY AND PULSATING  
FLOW THROUGH A COLLAPSIBLE THIN-WALLED VESSEL

---

**By**

Sifat Karim Chowdhury

---

The Supervisory Committee certifies that this *disquisition* complies with North Dakota  
State University's regulations and meets the accepted standards for the degree of

**MASTER OF SCIENCE**

SUPERVISORY COMMITTEE:

Dr. Yan Zhang

---

Chair

Dr. Jordi Estevadeordal

---

Dr. Yildirim Bora Suzen

---

Dr. Zhibin Lin

---

Approved:

03/11/2024

---

Date

Dr. Xiangqing Annie Tangpong

---

Department Chair

## ABSTRACT

An experimental study has been conducted to investigate complex fluid-structure interactions in collapsible tubes under steady and pulsatile flow conditions, which holds significant implications for many physiological fluid transport phenomena. Quantitative analysis of structural deformation and flow field analysis were conducted utilizing Particle Image Velocimetry (PIV) and optical image analysis. The results suggest that the tube wall deformation followed Shapiro's tube law under static and low-Re steady flow conditions. An increase in flow magnitude triggered self-excited oscillation under a critical range of negative transmural pressure. PIV results revealed periodic asymmetric jet downstream alongside velocity fluctuations during self-excited oscillation. Pulsatile flow induced cyclic symmetrical buckling under positive and neutral transmural pressures, while created traveling wave patterns under negative transmural pressures. Under highly negative transmural pressures, tube collapsed during diastole, limiting the mean flow rate. Brief self-excited oscillation was observed under such conditions, amplifying the peak flow rate within a pulsatile cycle.

## ACKNOWLEDGMENTS

I express my deepest gratitude to the Almighty for granting me strength, wisdom, and perseverance throughout this academic journey.

I wish to convey heartfelt appreciation to Dr. Yan Zhang, my advisor, for his unwavering guidance, continuous support, and the invaluable knowledge he shared throughout the years.

I am also deeply thankful to Dr. Jordi Estevadeordal, Dr. Yildirim Bora Suzen, and Dr. Zhibin Lin, the members of my committee, for their time, constructive feedback, helpful suggestions, and thoughtful critiques.

Lastly, I would like to express my heartfelt appreciation to my family and friends for their continuous support and encouragement. Their presence and encouragement have been a constant source of strength, and I am immensely grateful for their belief in me.

## TABLE OF CONTENTS

ABSTRACT.....	iii
ACKNOWLEDGMENTS .....	iv
LIST OF TABLES .....	vii
LIST OF FIGURES .....	viii
LIST OF ABBREVIATIONS.....	xiii
LIST OF SYMBOLS .....	xiv
LIST OF APPENDIX FIGURES.....	xvi
1. INTRODUCTION .....	1
1.1. Background .....	1
1.2. Literature Review .....	3
1.2.1. Theoretical Studies .....	3
1.2.2. Experimental Studies.....	6
1.3. Research Gaps.....	12
1.4. Objectives.....	12
2. RESEARCH METHOD.....	15
2.1. Governing Equations.....	15
2.2. Experimental Materials .....	18
2.3. Experimental Setup and Test Conditions.....	19
2.3.1. Experimental Set-Up of Steady Flow.....	19
2.3.2. Experimental Set-Up of Pulsatile Flow.....	20
2.3.3. PIV Measurements .....	22
2.4. Optical Measurements for Tube Deformations.....	23
3. COLLAPSIBLE TUBE UNDER STEADY FLOW .....	28
3.1. Introduction.....	28

3.2. Test Procedure and Conditions .....	28
3.3. Static Deformation of the Tube: A Validation against Tube Laws.....	31
3.4. Fluid-Structure Interactions under Steady Flows.....	33
3.4.1. Tube Deformation .....	33
3.4.2. Self-Excited Oscillation .....	35
3.4.3. Flow Limitation Effect in Steady Flow .....	42
3.5. Flow Field Analysis Based on PIV Data.....	45
3.5.1. Velocity Fluctuation during Self-Excited Oscillation.....	46
3.5.2. Asymmetrical Downstream Jet .....	50
3.6. Summary .....	53
4. COLLAPSIBLE TUBE UNDER PULSATILE FLOW .....	55
4.1. Introduction .....	55
4.2. Test Procedure and Conditions .....	56
4.3. Fluid-Structure Interactions under Pulsatile Flow Condition .....	58
4.3.1. Effect of Transmural Pressure on Pulsatile Flow .....	58
4.3.2. Effect of Reduced Reynolds and Womersley Numbers on Pulsatile Flow .....	66
4.3.3. Flow Limitation Effect in Pulsatile Flow .....	71
4.4. Summary .....	73
5. CONCLUSIONS.....	75
5.1. Concluding Remarks.....	75
5.2. Future Works.....	79
REFERENCES .....	80
APPENDIX. RAW IMAGES DURING STEADY AND PULSATILE FLOW .....	85

## LIST OF TABLES

<u>Table</u>		<u>Page</u>
1.	Area uncertainty statistics .....	25
2.	Steady flow cases .....	31
3.	Range of $\Pi$ at $\Delta P = 94.3$ mmHg for PIV analysis .....	46
4.	Pulsatile flow cases .....	58

## LIST OF FIGURES

<u>Figure</u>	<u>Page</u>
1. Shapiro’s tube law: Illustrating transmural pressure – area relation [1].....	1
2. Starling Resistor: A collapsible tube placed in a pressurized chamber, which may deform under sufficient external pressure [3].....	2
3. Simulation of collapsible vessel behavior for different wall thickness to diameter ratios [15].....	4
4. (a) Collapsible tube 1D model; (b) Area amplitude during self-excited oscillation [16].....	4
5. Collapse location moved left (toward downstream) for increased external pressure. Augmented degree of collapse was also spotted at $P_e = 116.7$ kPa [21]. .....	6
6. Self-excited oscillation burst under a certain range of Transmural pressure: (a) Self-excited oscillation decayed after $p_2$ dropped to a certain range; (b) Flow rate got independent $p_2$ and notably low during tube collapse [23].....	8
7. Overall scenario of two distinct types of self-excited oscillation: (a) Wall movement in between two extremes; (b) Low amplitude wall movement about either one of the extremes. Extremes are not necessarily axis-symmetric [27].....	8
8. Different types of self-excited oscillation shapes: (a) LU-type; and (b) LD-type [20].....	9
9. Downstream jet velocity during self-excited oscillation by utilizing PIV [30].....	10
10. Flow limitation effect under pulsatile flow compared to a steady flow through a stenosis tube model [31]. .....	11
11. Relationship of distensibility with pressure: (a) Non-linear relation with externally applied pressure [34]; (b) Change in distensibility with transmural pressure. ....	16
12. The tube model before (top) and after (bottom) RI matching. ....	18
13. The collapsible tube model: Dimensions have been provided along with fittings’ and pressure transducers’ locations. ....	19
14. Schematic of the experimental setup during steady flow. ....	20
15. Schematic of the experimental setup during pulsatile flow test. The pulsating pump was controlled by a unit connected to the computer.....	21
16. PIV set-up for steady flow experiment. ....	22



17.	High-speed camera captures images during steady flow experiment. ....	23
18.	Segmentation process using lazy-snapping method. From left to right (a) raw gray-scale image. (b) marking the foreground with a green line and the background with a red circle. (c) segmented black & white image is ready for further analysis.....	24
19.	A sample case from the pulsating flow test used for filter comparison. The flow rate was 1.5 Lpm with a frequency of 60 bpm at $\Pi = -24.8$ . ....	26
20.	Comparison of noise filtration using moving mean filter and S-G filter. $\beta$ is dimensionless axial cross-sectional area.....	27
21.	Schematic of the difference in pressure head of inlet supply and outlet reservoir during steady flow test. ....	29
22.	A black circle was drawn near the downstream to facilitate the optical analysis. ....	30
23.	Images of the cross-sectional shape at the middle of the tube ( $x = 75$ mm) under ‘no-flow’ condition with varied transmural pressures. ....	32
24.	Nondimensional cross-sectional area of collapsible tube vs. $\Pi$ compared with a theoretical model. Letters a through f correspond to the states of deformation illustrated in Figure 23. ....	33
25.	Nondimensional transmural pressure vs area curves under steady flows: $\Delta P = 12.6$ mmHg to 43.0 mmHg, no self-excited oscillation. ....	34
26.	Cross-sectional area was reduced when $\Pi$ went negative with a shape deformation from circle to dumbbell shape at case 5 ( $\Delta P = 43$ mmHg). ....	35
27.	Nondimensional transmural pressure vs area curves under steady flows: $\Delta P = 60.7$ mmHg to 98.0 mmHg, self-excited oscillation observed. ....	36
28.	Images of the cross-section of the collapsible tube during the first cycle of self-excited oscillation at case 10 ( $\Delta P = 94.3$ mmHg) when $\Pi = -30$ . ....	37
29.	Transmural pressure waveforms downstream of the tube showing self-excited oscillations: (a) $\Delta P = 68.6$ mmHg (Irregular waveform); (b) $\Delta P = 71.0$ mmHg; (c) $\Delta P = 87.7$ mmHg. ....	38
30.	Transmural pressure waveforms downstream of the tube during self-excited oscillations continued for even higher-pressure gradients: (a) $\Delta P = 94.3$ mmHg; (b) $\Delta P = 98.0$ mmHg. ....	39
31.	The dominant frequency of self-excited oscillations under different pressure gradients. ....	40

32.	Cross-section area amplitudes during self-excited oscillations: (a) $\Delta P = 87.7$ mmHg; (b) $\Delta P = 94.3$ mmHg; (c) $\Delta P = 98.0$ mmHg.....	42
33.	Change in the flow rate under reduced downstream transmural pressure: (a) Non-oscillating cases; (b) Self-excited oscillatory cases.....	43
34.	Change in the flow resistance: (a) Non-oscillating cases; (b) Self-excited oscillatory cases.....	45
35.	Velocity profiles at different time steps for 1 sec at $\Delta P = 94.3$ mmHg and $\Pi = -19$ case.....	47
36.	Continuous jet through the partially collapsed tube for 1.00 sec at $\Delta P = 94.3$ mmHg and $\Pi = -19$ case. No self-excited oscillation was observed.....	48
37.	Velocity profiles during one cycle of self-excited oscillation at $\Delta P = 94.3$ mmHg and $\Pi = -30$ case.....	49
38.	Periodic jet through the collapsed tube during one cycle of self-excited oscillation $\Delta P = 94.3$ mmHg and $\Pi = -30$ case.....	49
39.	Velocity profiles during one cycle of self-excited oscillation at $\Delta P = 94.3$ mmHg and $\Pi = -39$ case.....	50
40.	Periodic but discontinued jet through the collapsed tube during one cycle of self-excited oscillation at $\Delta P = 94.3$ mmHg and $\Pi = -39$ case.....	50
41.	Velocity profile from $t = 1.60$ sec to $1.87$ sec at $\Delta P = 94.3$ mmHg and $\Pi = -30$ during the third cycle of self-excited oscillation.....	51
42.	An asymmetrical downstream jet (upward) was observed at $t = 1.60$ sec at $\Delta P = 94.3$ mmHg and $\Pi = -30$ during the third cycle of self-excited oscillation.....	52
43.	Velocity profile from $t = 2.33$ sec to $2.60$ sec at $\Delta P = 94.3$ mmHg, $\Pi = -30$ during the fourth cycle of self-excited oscillation.....	53
44.	An asymmetrical downstream jet (downward) was observed at $t = 2.33$ sec at $\Delta P = 94.3$ mmHg and $\Pi = -30$ during the fourth cycle of self-excited oscillation.....	53
45.	Pressure and pump activation waveforms.....	55
46.	Reynolds number of venous flow input mimicking rest condition [52].....	56
47.	Pressure vs. time for baseline case ( $Re = 655$ , $Wo = 10.4$ ) at mean downstream $\Pi = +52.2$ . The dotted line represents the chamber pressure at those cycles.....	59
48.	Area vs. time for baseline case ( $Re = 655$ , $Wo = 10.4$ ) at mean downstream $\Pi = +52.2$ .....	59

49.	PIV results for baseline case ( $Re = 655$ , $Wo = 10.4$ ) at highly positive mean downstream $\Pi = +52.2$ . Left column shows the raw images and right column shows the flow field with streamlines.....	60
50.	Instantaneous velocity before the peak systole at $t = 0.1$ sec (left column) and peak systole $t = 0.2$ sec (right column) for baseline case at $\Pi = +52.2$ (highly positive).....	61
51.	Pressure vs. time for baseline case ( $Re = 655$ , $Wo = 10.4$ ) at mean downstream $\Pi = +6.9$ . The dotted line represents the chamber pressure at those cycles. ....	62
52.	Area vs. time for baseline case ( $Re = 655$ , $Wo = 10.4$ ) at mean downstream $\Pi = +6.9$ . Fluctuation in the area amplitude has been observed. ....	62
53.	PIV results for baseline case ( $Re = 655$ , $Wo = 10.4$ ) at slightly positive mean downstream $\Pi = +6.9$ . Left column shows the raw images and right column shows the flow field with streamlines.....	63
54.	PIV results for baseline case ( $Re = 655$ , $Wo = 10.4$ ) at highly negative mean downstream $\Pi = -36.4$ . Left column shows the raw images and right column shows the flow field with streamlines. At $t = 0.4$ sec, flow reversal was observed with a different color bar.....	64
55.	Area vs. time for baseline case ( $Re = 655$ , $Wo = 10.4$ ) at highly negative mean downstream $\Pi = -36.4$ . Fluctuation in area amplitude has been observed, amplitude went down.....	65
56.	Pressure vs. time for baseline case ( $Re = 655$ , $Wo = 10.4$ ) at mean downstream $\Pi = -36.4$ . Self-excited oscillation triggered in the collapsible tube downstream.....	65
57.	Earlier and prolonged self-excited oscillation triggered at baseline case ( $Re = 655$ , $Wo = 10.4$ ) under $\Pi = -48.9$ .....	66
58.	Area vs. time: (a) Baseline case ( $Re = 655$ , $Wo = 10.4$ ) at $\Pi = +6.9$ ; (b) Half Re case ( $Re = 327$ , $Wo = 10.4$ ) at $\Pi = +6.3$ . ....	67
59.	PIV raw images of the axial cross-sectional area under baseline and altered Re case at similar slightly positive $\Pi$ . ....	67
60.	Velocity map utilizing PIV results under baseline and altered Re case at similar slightly positive $\Pi$ . ....	68
61.	Area vs. time: (a) Baseline case ( $Re = 655$ , $Wo = 10.4$ ) at $\Pi = +6.9$ ; (b) Half frequency case ( $Re = 655$ , $Wo = 7.4$ ) at $\Pi = +6.3$ . ....	69
62.	PIV raw images of the axial cross-sectional area under baseline and altered $Wo$ case at similar slightly positive $\Pi$ . ....	69

63.	Velocity map utilizing PIV results under baseline and altered $Wo$ case at similar slightly positive $\Pi$ .	70
64.	Comparison of self-excited oscillation burst under highly negative mean downstream transmural pressure. Half $Re$ case didn't trigger self-excited oscillation.	71
65.	Mean flow rates under pulsatile flow with different $Re$ and $Wo$ numbers: (a) Reducing $Re$ by half; (b) Reducing frequency by half.	72
66.	Peak flow rates under pulsatile flow with different $Re$ and $Wo$ numbers: (a) Reducing $Re$ by half; (b) Reducing $Wo$ by half.	73

## LIST OF ABBREVIATIONS

FSI.....	Fluid-structure interaction.
PIV .....	Particle image velocimetry.
SEO.....	Self-excited oscillation.
LU .....	Lower frequency oscillation and primarily maintaining cycle above mean pressure.
LD .....	Lower frequency oscillation and primarily maintaining cycle below mean pressure.
LS .....	Large sine.
FFT.....	Fast Fourier transform.
LPM .....	Liters per minute.
BPM .....	Beats per minute.

## LIST OF SYMBOLS

$P$	Internal pressure.
$P_e$	External pressure.
$P_{tm}$	Transmural pressure.
$\Delta P$	Pressure difference across the collapsible tube.
$\rho$	Fluid density.
$t$	Time.
$u$	Longitudinal velocity.
$x$	Longitudinal distance.
$A$	Tube cross-sectional area.
$A_0$	Neutral tube cross-sectional area.
$R$	Flow resistance.
$c$	Wave speed.
$D$	Tube distensibility & tube diameter.
$K_p$	Flexural rigidity.
$u_{cric}$	Critical velocity for initiating self-excited oscillation.
$E$	Elastic modulus.
$\nu$	Poisson's ratio.
$\gamma$	Ratio of tube wall thickness to the inner radius.
$\Pi$	Nondimensional transmural pressure.
$\alpha$	Nondimensional tube cross-sectional area.
$Re$	Reynolds number (based on the mean flow rate and characteristic length of the inner diameter of the tube).
$y/a$	Dimensionless width of flow channel on the measured plane during steady flow PIV.

- $Q$  ..... Flow rate.
- $Q_m$  ..... Mean flow rate of pulsating flow cycle.
- $f$  ..... Friction factor of minor losses.
- $Wo$  ..... Womersley number.
- $\beta$  ..... Dimensionless axial cross-sectional area of collapsible tube.
- $\Omega$  ..... Axial cross-sectional area of the collapsible tube at any condition.
- $\Omega_0$  ..... Axial cross-section area without external pressure on the pressurized chamber and no flow condition.

## LIST OF APPENDIX FIGURES

<u>Figure</u>	<u>Page</u>
A1. Images of the radial cross-section of collapsible tube during the first cycle of self-excited oscillations at case 10 ( $\Delta P = 98$ mmHg) when $\Pi = -30, -52$ & $-78$ correspondingly from top to down.....	85
A2. Pulsatile flow-induced tube collapsing at three different times of the cycle of baseline case for (a) Positive $\Pi$ ; (b) Slightly positive $\Pi$ (c) Slightly negative $\Pi$ ; (d) Negative $\Pi$ .....	86
A3. Pulsatile flow-induced tube collapsing at three different times of a cycle of half Re case for (a) Positive $\Pi$ ; (b) Slightly positive $\Pi$ (c) Slightly negative $\Pi$ ; (d) Negative $\Pi$ . ....	87
A4. Pulsatile flow-induced tube collapsing at three different times of a cycle of half frequency (reduced Wo number) case for (a) Positive $\Pi$ ; (b) Slightly positive $\Pi$ (c) Slightly negative $\Pi$ ; (d) Negative $\Pi$ .....	88



# 1. INTRODUCTION

## 1.1. Background

The study of fluid flow characteristics in collapsible vessels holds a significant role in the field of biofluid mechanics, with examples encompassing the upper airways of the respiratory system to the circulation of blood through veins, capillaries, and arteries. The interplay between the fluid and the surrounding structure becomes particularly crucial in environments where these biological tubes may undergo deformation, manifesting flow limitation and potentially leading to collapse. The extent of the collapse is dependent on the transmural pressure and pressure gradient between the upstream and downstream sections of that vessel for a given Reynolds number. The phenomenon of vessel collapse due to changes in transmural pressure can be explained by the tube law presented by Shapiro [1] as Equation 1.

$$P_{tm} = P - P_e = f(A) \quad (1)$$

where  $P$  is the pressure inside the vessel,  $P_e$  is external pressure and  $A$  is the cross-sectional area of the vessel.  $P_{tm}$  is transmural pressure and deformation of the tube depending on the  $P_{tm}$  can be seen in Figure 1 which is based on the quasi-one-dimensional assumption.

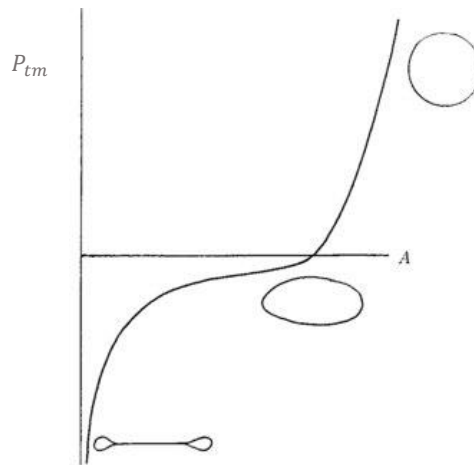


**Figure 1.** Shapiro's tube law: Illustrating transmural pressure – area relation [1].

Self-excited oscillation is another complex phenomenon that could occur in blood and respiratory flows. It is caused by the interaction between the deformation of the blood vessel and the pressure of the fluid acting on the inner wall of the vessel [2]. Specifically, when there is an imbalance between the outside pressure and the hydrostatic pressure in the vessel, the diameter of the vessel undergoes non-linear deformation which interplays with fluid vortex shedding, leading to self-excited oscillations. This phenomenon can be explained using the Starling resistor, which is an experimental collapsible vessel model that has been studied extensively [3]. Despite the substantial complexity observed in vessels within the body when compared to a Starling resistor, these resistor models have been shown to serve as a valuable approximation for physiological vessels [4].

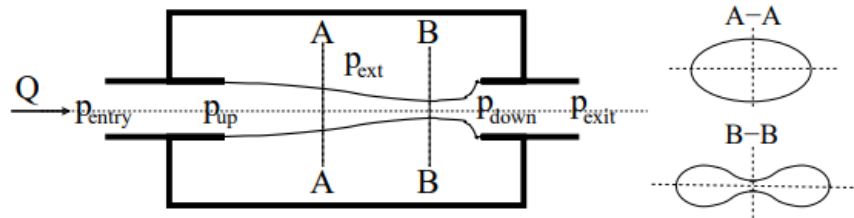


**Figure 2.** Starling Resistor: A collapsible tube placed in a pressurized chamber, which may deform under sufficient external pressure [3].

From a physiological perspective, conditions like pulmonary vein stenosis exemplify vein narrowing due to wall thickening, causing collapse under increased blood flow velocities [5]. Similarly, in upright postures, jugular veins may experience negative transmural pressure, leading to vessel collapse and reduced flow rates [6]. Flow-induced instabilities are present in the external jugular vein during upright postures exposed to negative transmural pressure [7]. In microgravity, jugular veins experience less negative transmural pressure and tend to distend due to an upward fluid shift and diminished hydrostatic pressure gradient [8]. Recent space studies

revealed that such changes in the gravitational field caused flow stagnation and reversal in astronaut's jugular vein, causing venous thrombosis in space crews [6], [9]. Additionally, understanding these fluid-structure interactions is also crucial in explaining respiratory diseases, such as obstructive sleep apnea [10].

## **1.2. Literature Review**

### **1.2.1. Theoretical Studies**

For the past few decades, plenty of research has been done to understand the dynamics of fluid flow in thin-wall collapsible tubes using theoretical approaches. Simple 1D models have been developed to explore the change in cross-sectional shape depending on the varied transmural pressure, flow limitations, potential downstream elastic jump in bronchial airways, and existence of self-excited oscillations [11], [12], [13]. Jensen et al. (1990) identified a critical flow rate where a stable cross-sectional area transitions to instability, resulting in eventual collapse and reversal of flow direction [14]. Kozlovsky et al. (2014) simulated a 2D collapsed vessel under negative transmural pressure, showcasing highly distensible regions with significant reductions in cross-sectional areas, even with slight pressure alterations, though the degree of collapse varied with wall thickness relative to inner diameter [15]. Figure 3 shows that the degree of reduction in the area of the collapsed region may vary depending on the  $\gamma$ , which is a measure of the thickness of the walls of a tube relative to its inner diameter. However, the overall trend of collapse is similar in all cases.

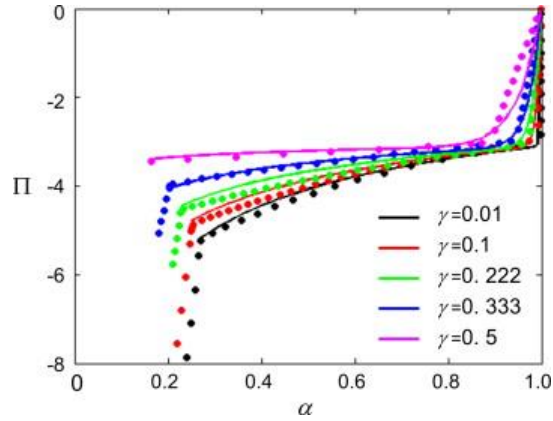


**Figure 3.** Simulation of collapsible vessel behavior for different wall thickness to diameter ratios [15].

Tang et al. (2015) modeled a collapsible tube by simulating it as a 2D beam with an elastic wall, as shown in Figure 4(a). External pressure on the elastic wall caused self-excited oscillations, with the most significant deformations consistently downstream. Higher negative transmural pressure amplified self-excited oscillation amplitude in the  $y$ -direction [16]. Figure 4(b) illustrates the trend in the change of self-excited oscillation amplitude as a function of external pressure applied to the tube. Increased external pressure indicates more negative transmural pressure.

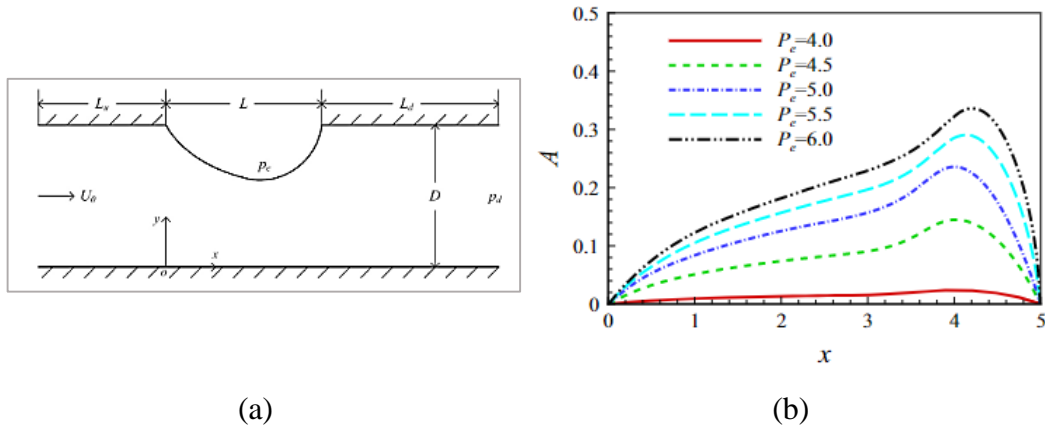


**Figure 4.** (a) Collapsible tube 1D model; (b) Area amplitude during self-excited oscillation [16].

Laudato et al. (2023) explored the tube law and degree of collapse by varying other tube properties including length of the tube, length to inner diameter ratio, etc. [17]. Recent studies

have gone beyond quasi 1D, or 2D models and steady flow through 3D collapsible tubes has been studied. Hazel and Heil (2003) found negative transmural pressure causes non-axisymmetric buckling, leading to fluid-solid interaction [18]. Some useful non-dimensional parameters have been introduced to explain fluid-structure interactions using 3D models. The non-dimensional parameter  $Q$  can show the relationship between the tube's stiffness and viscous forces in Equation 2.

$$Q = \frac{\mu \bar{U}}{RK} \quad (2)$$

where  $K$  is the tube's flexural rigidity,  $R$  is the tube's inner radius,  $\mu$  is viscosity and  $\rho$  is the density of the fluid mixture.  $Q \rightarrow 0$  indicates that the tube's stiffness is pretty high, and the tube deformation only depends on the external pressure with a mean velocity of  $\bar{U} = 0$ . Using  $Q$ , another non-dimensional parameter  $H$  can be defined as Equation 3, which remains constant during any experiment using the same fluid and tube. When fluid is highly viscous,  $H \rightarrow 0$ . On the other hand, higher inertia compared to fluid viscosity results in  $H > 0$ . This work also suggests reporting the Reynolds number for experimental cases based on the tube's undeformed diameter.

$$H = \frac{Re}{Q} = \frac{\rho KR^2}{\mu^2} \quad (3)$$

Although the Reynolds number reported in this study had a limited range, it still identified instability in the degree of collapse as the Reynolds number increased. In fact, three-dimensional unsteady flows in collapsible tubes have been analyzed with high-frequency oscillating walls and a critical Reynolds number was identified where the wall extracts energy from the flow, potentially triggering sustained self-excited oscillations [19]. This work

highlighted that the frequency of self-excited oscillation is dependent on the material properties of the system.

### 1.2.2. Experimental Studies

While theoretical analyses provide a robust foundation for understanding collapse and self-excited oscillation, the validation and extension of these theories necessitate experimental studies. The behavior of collapsible tubes under negative transmural pressure, examined via starling resistors, reveals the pronounced collapsibility at the throat downstream [20], [21]. This collapse pattern aligned with Shapiro's tube law and intensified with increased flow rates, leading to complete collapse. Additionally, altering transmural pressure shifts the collapse location. It has been reported to be a function of external pressure, as shown in Figure 5 [21].

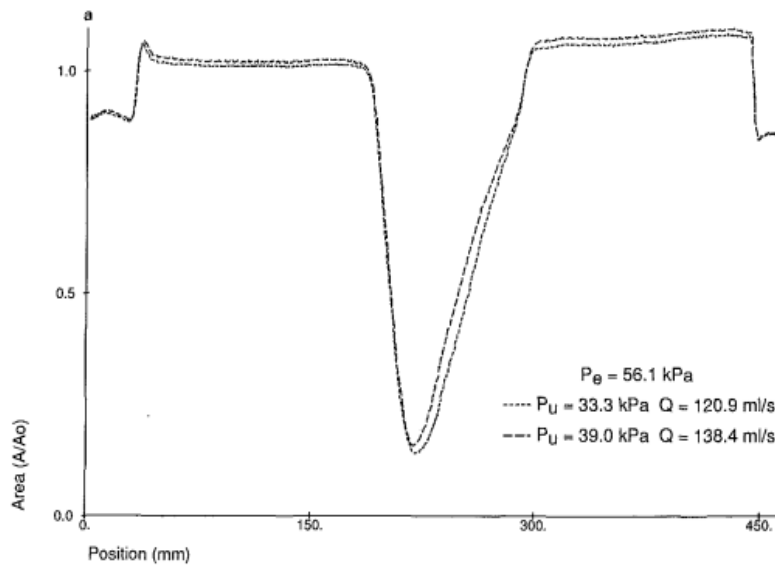


**Figure 5.** Collapse location moved left (toward downstream) for increased external pressure. Augmented degree of collapse was also spotted at  $P_e = 116.7$  kPa [21].

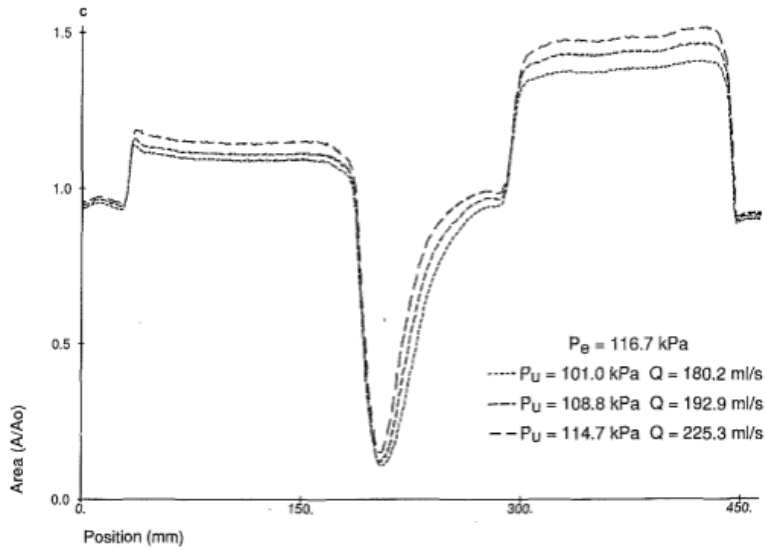


**Figure 5.** Collapse location moved left (toward downstream) for increased external pressure. Augmented degree of collapse was also spotted at  $P_e = 116.7$  kPa [21] (continued).

These findings provide important insights into the flow dynamics and wall reactions of collapsible tubes, particularly in conditions where biological tubes may experience negative transmural pressure.

Gavriely et al. (1989) found buckled tube and limited flow rates potentially initiate flow-induced (self-excited) oscillation during the study of generation of respiratory wheezing in a thick-walled tube [22]. Bertram et al. (2006) identified flow limitations when the transmural pressure went down by setting lower downstream pressure, indicating that the tube collapsed toward the downstream in that case [23]. Even with gel, mimicking surrounding tissues, the deformation of the collapsible tube does not differ from the classical tube law. Tube deformation, primarily area reduction, persists under negative transmural pressure, following the same pattern without surrounding [24]. Several studies observed self-excited oscillations after negative transmural pressure reaches a threshold, manifesting in downstream pressure and flow rate data [23], [25]. Moreover, different percentages in mixtures of working fluids did not cause any major differences in the laminar flow rates that triggered self-excited oscillations [26].

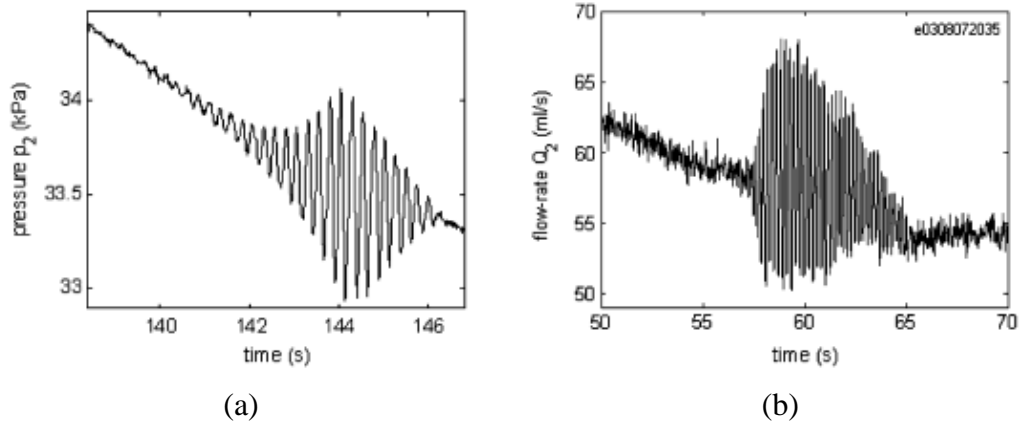


**Figure 6.** Self-excited oscillation burst under a certain range of Transmural pressure: (a) Self-excited oscillation decayed after  $p_2$  dropped to a certain range; (b) Flow rate got independent  $p_2$  and notably low during tube collapse [23].

Figure 6 illustrates the burst of self-excited oscillation under the negative zone of transmural pressure, followed by decay after a certain range of downstream pressure ( $p_2$ ).  $\gamma$  value was 0.17 in this experiment and the unsupported length of the silicon tube was 228 mm. At the same time, the flow rate became independent of  $p_2$ , when  $p_2$  went lower and the tube was in the process of collapse [23].

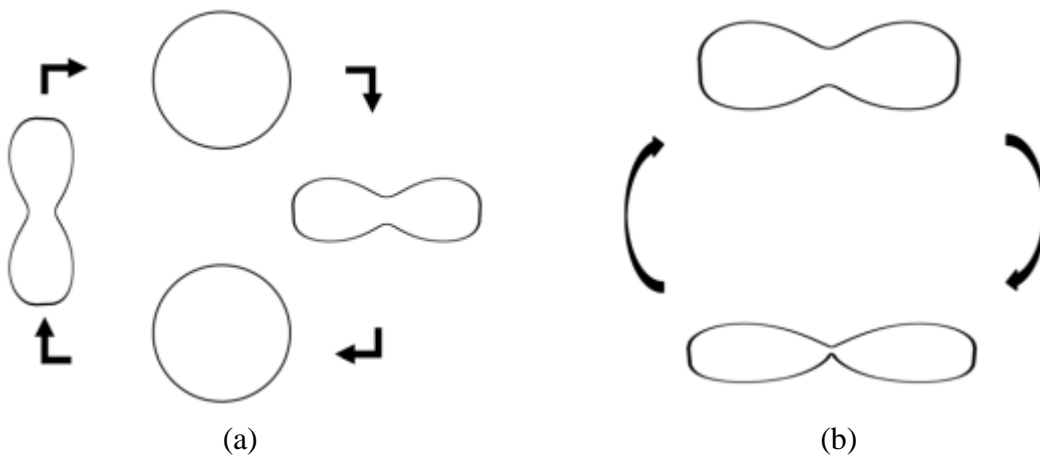


**Figure 7.** Overall scenario of two distinct types of self-excited oscillation: (a) Wall movement in between two extremes; (b) Low amplitude wall movement about either one of the extremes. Extremes are not necessarily axis-symmetric [27].



The type of oscillation is another aspect of observing the fluid-structure interaction, especially when self-excited oscillation is triggered. Wang et al. (2016) experimentally verified the types of self-excited oscillation mentioned in Figure 7, which was already reported by Heil and Water (2006). In general, self-excited oscillation starts from a fully open regime experiencing the wall motion in two different extremes simultaneously, where starting from a buckled, or collapsed condition faces the other type of self-excited oscillation [27], [28]. Experimental research has also identified two distinct types of waveforms during self-excited oscillations: LU-type and LD-type. L indicates lower frequency and U, or D indicates the downstream waveform staying either above a line of mean pressure, or below that mean pressure value for most of the time of the cycle. These waveforms were plotted by graphing downstream pressure against time and are depicted as mentioned shapes in Figure 8 [20].

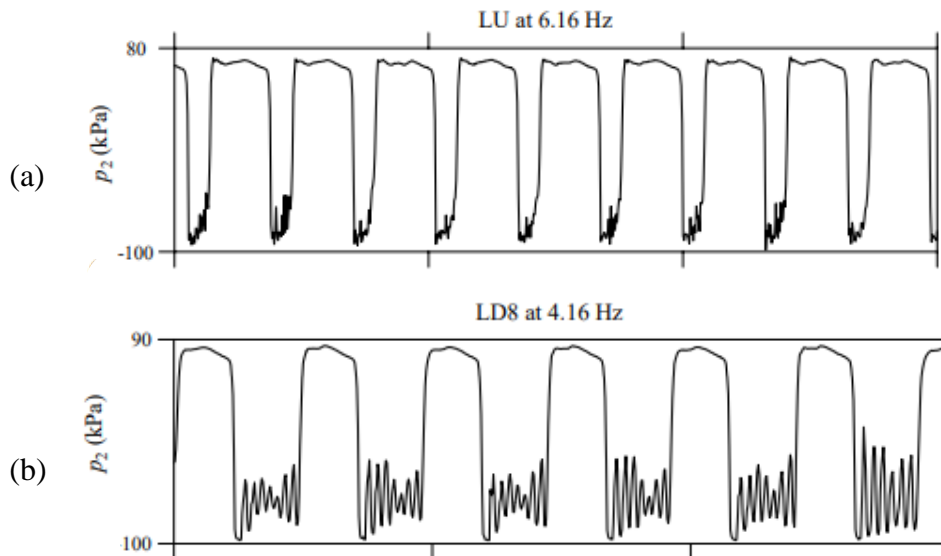


**Figure 8.** Different types of self-excited oscillation shapes: (a) LU-type; and (b) LD-type [20].

Different waveforms like LU (lower frequency – primarily maintaining above mean pressure), or LD (lower frequency – primarily maintaining below mean pressure) have been identified as well in other studies [15], [25], [29]. The frequency of self-excited oscillation can

vary depending on fluid velocity. Changes in pressure gradient act as a factor that accelerates the flow, likely leading to an increase in frequency [22].

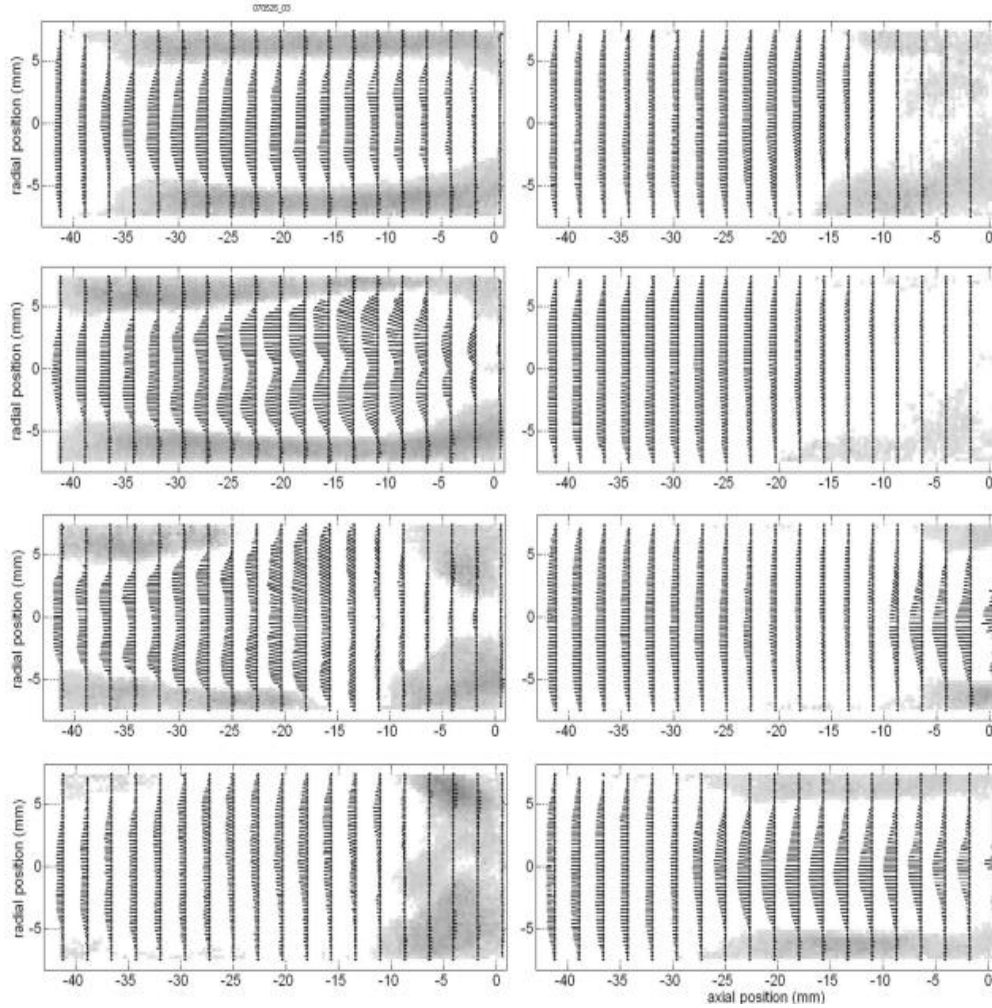


**Figure 9.** Downstream jet velocity during self-excited oscillation by utilizing PIV [30].

In recent years, Particle Image Velocimetry has been used to visualize downstream jet shapes of the tube’s self-excited oscillation during experiments and analyzed velocity vectors for predetermined cases to demonstrate the self-excited oscillatory movement of the wall of the tube [30]. Figure 9 displays the different moments of the downstream jet captured during this experiment, where in left column from top to down velocity profile was found in parabolic shape

at the axial position of -30 mm of flow field. By progressing to the next phase, the velocity profile flattened, which indicates the reduction both in peak and average velocity.

Despite extensive research on steady-flow Starling resistors, there still is a lack of experimental data quantifying the fluid-structural interaction in collapsible tubes, particularly for pulsatile flow and self-excited oscillations. Kobayashi et al. (2004) investigated the impact of pulsatile flow on a stenosis model and analyzed changes in flow rate in response to reduced downstream pressure. They observed that within a specific range of downstream pressure, pulsatile flow resulted in flow choking, particularly around an average downstream pressure of 15 mmHg, as shown in Figure 10. Interestingly, the stenosed model did not exhibit any flow limitation under steady flow conditions despite similar reductions in downstream pressure [31].

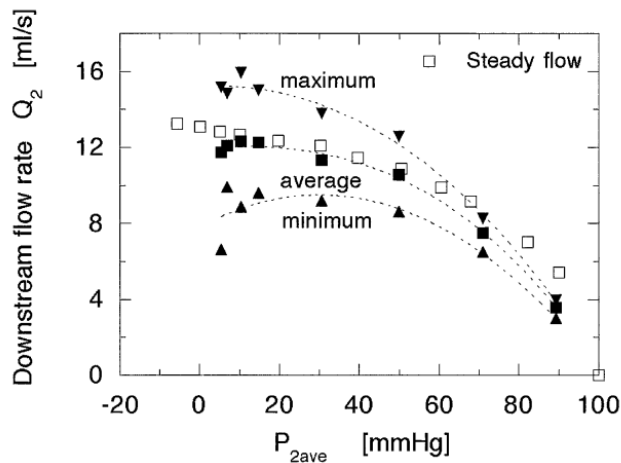


**Figure 10.** Flow limitation effect under pulsatile flow compared to a steady flow through a stenosis tube model [31].

During the study of disparities in obstructive sleep apnea between males and females, Zarandi et al. (2021) assumed a Starling resistor as the pharynx. Pulsating air flow was used through the collapsible tube when analyzing upper airway collapse. Through finite element analysis, they quantified the buckling of the tube to ascertain the influence of tube length on critical buckling pressure. Upon employing the proposed model and comparing the outcomes

with experimental data, it was concluded that shorter collapsible tubes exhibit higher resistance to transmural pressures before buckling compared to their longer equivalents [32].

### **1.3. Research Gaps**

There has been relatively little experimental research done on the optical analysis of collapsing tubes to observe the fluid-structure interaction under a wide range of Reynolds numbers and transmural pressure. To address this knowledge gap, researchers could conduct experiments that focus on optical analysis of tube collapse under a range of Reynolds numbers and transmural pressures. This would involve using high-speed cameras or other imaging techniques to capture the collapse of the tube and then analyzing the resulting images to identify key features of the flow. PIV could be used to study fluid flows under a wide range of conditions, including complete collapse and self-excited oscillations. In the case of tube collapse, PIV could be used to observe the flow field as the tube collapses and to identify changes in velocity and direction of flow. This could provide valuable insights into the mechanisms underlying tube collapse and help to improve the design of medical devices.

Another research gap in simple collapsible tube experiments is the need for more experimental data on the behavior of these systems under different flow conditions. While there have been many studies on the behavior of collapsible tubes under steady-state flow conditions, there is still much to learn about how these systems behave under unsteady or pulsatile flow conditions.

### **1.4. Objectives**

The objective of the research is to understand the physics behind static deformation and self-exciting oscillations for predicting and controlling the behavior of collapsible tubes in

physiological conditions. Our present work aimed to explore two distinct phases of motion for the collapsible tubes:

- First, static deformation and self-excited oscillations were studied under steady flow inputs.
- Second, we subjected the collapsible tube to a pulsatile flow to assess fluid-structure interaction under unsteady pulsatile flows, mimicking typical physiological transport phenomena.

In both steady and pulsatile flow scenarios, we observed bursts of self-excited oscillation beyond critical transmural pressures. Additionally, flow limitation phenomena have been discussed in both steady and pulsating conditions.

The thesis organization can be outlined as following chapters:

- Chapter 1: Introduction. In this chapter, the background, literature review of theoretical and experimental works, research gaps, and objectives have been introduced.
- Chapter 2: Research method. This chapter will explain the governing equations, experimental set-up, and data analysis approach.
- Chapter 3: Collapsible tube under steady flow. In this chapter, an experimental study on static deformation and self-excited oscillations in response to steady flow inputs will be presented.
- Chapter 4: Collapsible tube under pulsatile flow. This chapter explores the interaction between fluids and structures amidst dynamic pulsatile flows, mimicking common physiological boundary conditions.

- Chapter 5: Conclusions. In this chapter, the experiment results will be summarized and areas of improvement and limitations will be discussed.

## 2. RESEARCH METHOD

### 2.1. Governing Equations

A collapsible tube flow system, i.e., Starling resistor, can be approximated by a quasi-1D model described by the governing equations below: Equation 4, the momentum equation, describes the change of the axial velocity  $u$  as a function of distance and time, driven by the longitudinal pressure gradient:

$$\frac{\partial u}{\partial t} + u \frac{\partial u}{\partial x} = -\frac{1}{\rho} \frac{\partial p}{\partial x} \quad (4)$$

The continuity equation, Equation 5 describes the change of the cross-sectional area ( $A$ ) of the collapsible tube in the axial direction:

$$\frac{\partial A}{\partial t} + \frac{\partial(Au)}{\partial x} = 0 \quad (5)$$

To solve the above equations, the tube constitutive model is defined by Shapiro's tube law:  $A(x, t) = f[P_{tm}(x, t), x]$ , which relates the transmural pressure ( $P_{tm} = P_{internal} - P_{external}$ ) to the cross-sectional area ( $A$ ) of the tube. When  $P_{tm}$  is highly positive, the tube is axis-symmetrically distended and a large transmural pressure change is necessary to induce any change in the tube's cross-sectional area. When  $P_{tm}$  is close to zero, small changes to  $P_{tm}$  can lead to a significant change in the cross-sectional area [33]. By solving Equations 4 and 5 under steady state, the cross-section area along axial direction can be described by:

$$\frac{1}{A} \frac{dA}{dx} = -\frac{1}{u} \frac{du}{dx} = \frac{-Ru}{c^2 - u^2} \quad (6)$$

where  $R$  is the friction factor and  $c$  and  $u$  denote the wave speed and flow velocity, respectively. The wave speed  $c$  defines the speed of small-amplitude perturbations traveling along the tube wall as:

$$c = \sqrt{\frac{1}{\rho D}} \quad (7)$$

where  $D$  is the distensibility of the tube and  $\rho$  is the density of the fluid. Distensibility can be defined by Equation 8.

$$D = \frac{1}{A} \left( \frac{\partial A}{\partial P} \right) \quad (8)$$

Distensibility has a non-linear relationship with applied pressure, which is depicted in Figure 11 [34]. Therefore, under highly positive or highly negative transmural pressure it is quite difficult to deform the tube shape by applying external pressure.

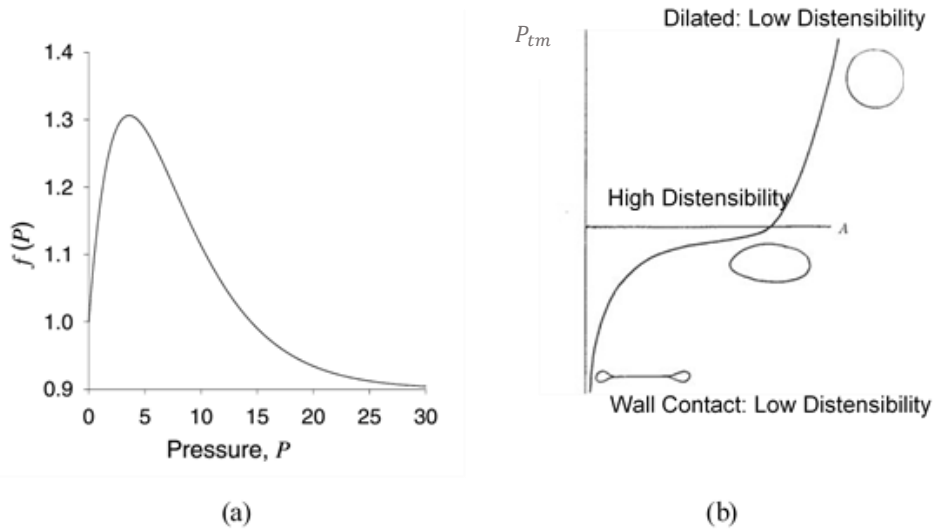


**Figure 11.** Relationship of distensibility with pressure: (a) Non-linear relation with externally applied pressure [34]; (b) Change in distensibility with transmural pressure.

The flow behavior indicated by Equation (6) is analogous to the compressible nozzle flow. For example, If the flow velocity  $u$  is less than the wave speed  $c$  in Equation 6,  $dA/dx$  is negative and the cross-section area  $A$  will decrease in the direction of the flow, while  $du/dx$  is positive and the flow will accelerate in the flow direction. This scenario is subcritical. In contrast, if  $u$  is greater than  $c$ ,  $A$  will increase and  $u$  will decrease in the direction of flow, which



represents a supercritical condition. In either case, the flow velocity  $u$  will approach to  $c$ , hence flow limitation, similar to choking in compressible nozzles, will occur in collapsible tube flows. As a subcritical flow goes into the collapsible tube, the flow acceleration will continue until the cross-section area decreases to a minimum (throat), where a further increase of flow velocity requires a local distensibility jump (similar to aerodynamic shock waves). Therefore, the critical velocity at the throat would be important for unsteady behaviors, such as self-excited oscillations in such tube flows. Heil et al. (2008) mentioned this critical velocity can be estimated by Equation 9.

$$u_{crit} = \sqrt{\frac{K_p}{\rho}} \quad (9)$$

where  $K_p$  denotes the flexural rigidity of the tube and keeps an inverse relation with distensibility [20], which can be defined by Equation 10 using other material properties ( $\nu$ ,  $\gamma$ ):

$$K_p = \frac{E}{12(1 - \nu^2)} (\ln(1 + \gamma))^3 \quad (10)$$

Here,  $\gamma$  represents the ratio of the tube wall thickness to the inner radius.  $E$  is elastic modulus and it is obtained using the well-known correlation between Elastic (Young's) modulus and hardness as Equation 11 [35], [36].

$$E = \frac{0.0981(56 + 7.62336S)}{0.137505(254 - 2.54S)} \quad (11)$$

$S$  denotes the Shore A hardness. In this study, the Shore A hardness is measured using Shore A durometer in the NDSU Materials Testing Lab to determine the Young's modulus of the sample of the hyper-elastic tube material.

## 2.2. Experimental Materials

A commercial hyper-elastic PDMS tube was obtained for this experimental study. This collapsible tube has a wall thickness of 0.7 mm, an unfixed length of 150 mm, and an inner diameter ( $D$ ) of 15 mm. This tube material is non-viscous with an elastic (Young's) modulus of 1.44 MPa, and a Poisson's ratio ( $\nu$ ) of 0.47. Different elasticity of the collapsible tube might affect the resistance to deformation under negative transmural pressure and shape retention when positive transmural pressure is applied. Based on the material properties and the thickness to radius ratio  $\gamma = 0.093$ , the flexural rigidity of the tube ( $K_p$ ) is calculated to be 0.83 mmHg using equation (4).

Optical analysis necessitates a fluid with a matching Refractive Index (RI) to the tube's optical properties. Therefore, a fluid mixture of 60% water and 40% glycerol was used to match the RI of 1.4 [37]. This mixture had a density of 1.080 kg/mL and viscosity ( $\mu$ ) of 3.5 cP, closely mimicking the properties of actual blood plasma. A commercial RI meter was used to measure the RI of the fluid mixture. Figure 12 illustrates the optical states before and after using the fluid mixture both inside and outside the tube, suggesting that the mixture efficiently eliminated optical distortion for this experiment.

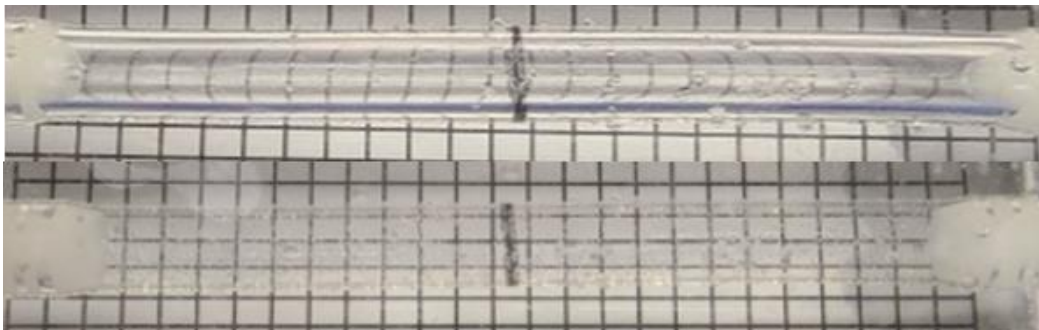


**Figure 12.** The tube model before (top) and after (bottom) RI matching.

### 2.3. Experimental Setup and Test Conditions

In this study, we conducted two series of experiments with 1) steady flow inputs and 2) pulsatile flow inputs. For both experiments, the collapsible tube model was installed into a pressure chamber. The pressure-controlled chamber was filled up with the same RI-matching fluid mixture and completely sealed. A syringe pump is connected to the pressure chamber to precisely control the external pressure to the tube. High-frequency pressure transducers were installed upstream, downstream, and within the pressure-controlled chamber to measure pressure data at a sampling frequency of 5 kHz. An ultrasonic flow meter was installed downstream right after the pressure transducer to record the flow rate data. The pressure transducers used have an equipment uncertainty of  $\pm 2\%$ ; the flow meter used has an equipment uncertainty of  $\pm 1\%$ . A schematic of the tube dimension, axial coordinate definition, and the pressure sensors' locations is illustrated in Figure 13.

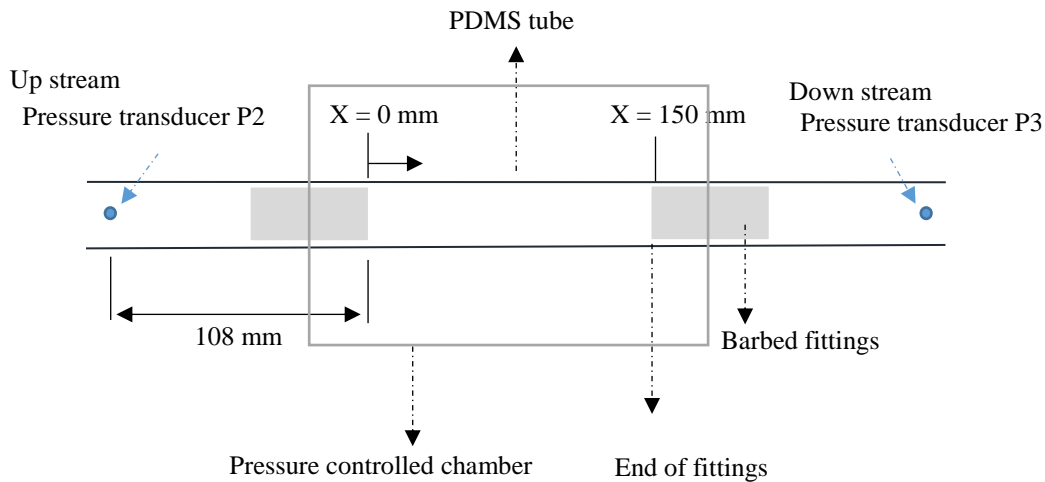


**Figure 13.** The collapsible tube model: Dimensions have been provided along with fittings' and pressure transducers' locations.

#### 2.3.1. Experimental Set-Up of Steady Flow

For steady flow experiments, the pressure chamber was integrated into a closed-loop flow system driven by a steady centrifugal fluid pump as shown in Figure 14. The downstream

reservoir maintained a constant fluid level, while the height of the upstream tank was changed at the beginning of each test run for a new flow rate condition. For each upstream tank height, the chamber pressure was precisely controlled by a syringe pump. The chamber pressure was changed from low to high, gradually collapsing the tube. Overall, the flow rates range from 0.20 L/min (the lower end of flow through veins) to 5 L/min (the normal cardiac output of adult humans) during the steady flow tests. The transmural pressures range from -80 mmHg to 40 mmHg with an internal pressure varying from 5 mmHg to 150 mmHg, representing typical values in physiological circulation systems [38], [39], [40], [41], [42].

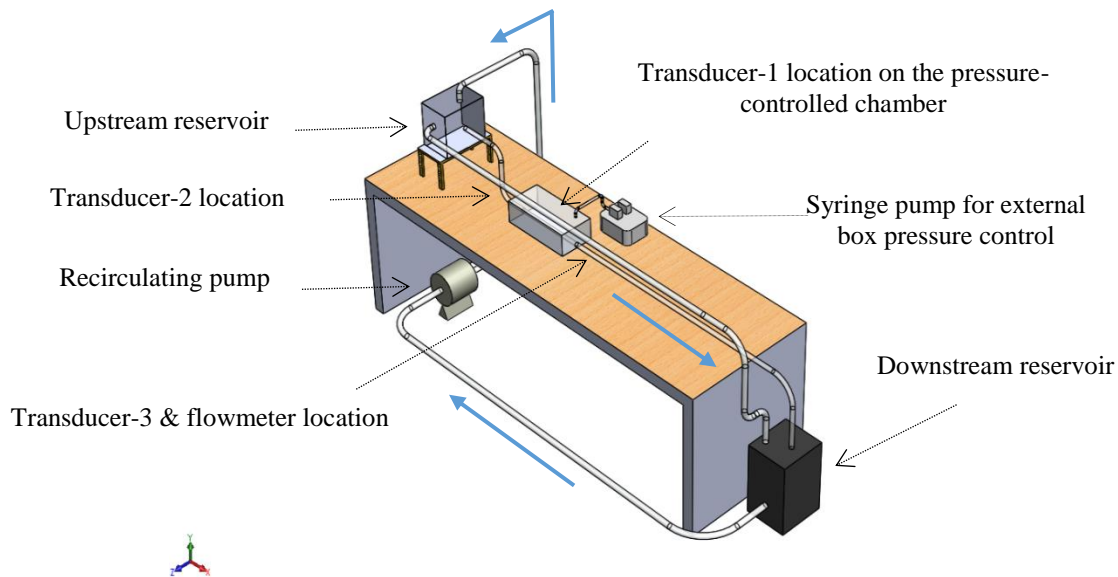


**Figure 14.** Schematic of the experimental setup during steady flow.

### 2.3.2. Experimental Set-Up of Pulsatile Flow

For pulsatile flow experiments, the centrifugal pump was replaced by a programmable pulsatile flow pump (BDC laboratory) as shown in Figure 15. This pump allowed user-defined flow rates, frequency, and waveforms for experimental needs. Ball valves on the pump head were used to maintain the forward pulsating flow. The test procedure was similar to the steady flow experiments: first, the pulsatile input was fixed for a new flow condition; then the chamber

pressure was changed gradually to measure the flow and tube dynamics from distended to collapsed scenarios. Overall, two different frequencies (1 Hz and 0.5 Hz) and flow rates (1.5 and 0.75 Liter per minute) were tested to represent the Womersley number and the Reynolds number ranges respectively of typical venous flow [43]. Test conditions will be discussed more in Chapter 4.

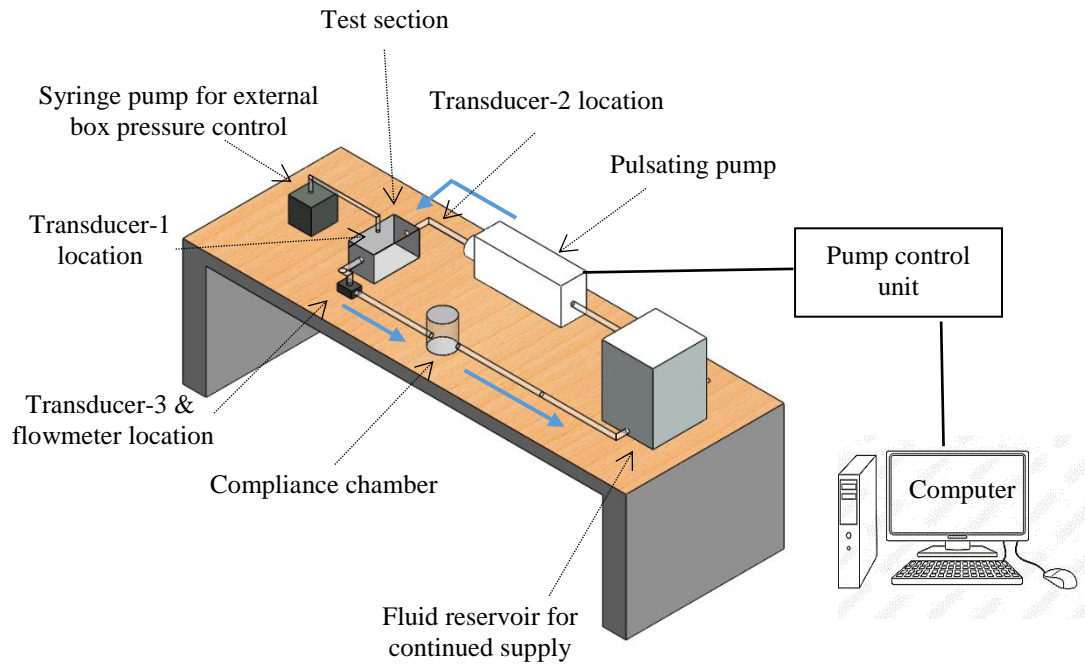


**Figure 15.** Schematic of the experimental setup during pulsatile flow test. The pulsating pump was controlled by a unit connected to the computer.

### 2.3.3. PIV Measurements

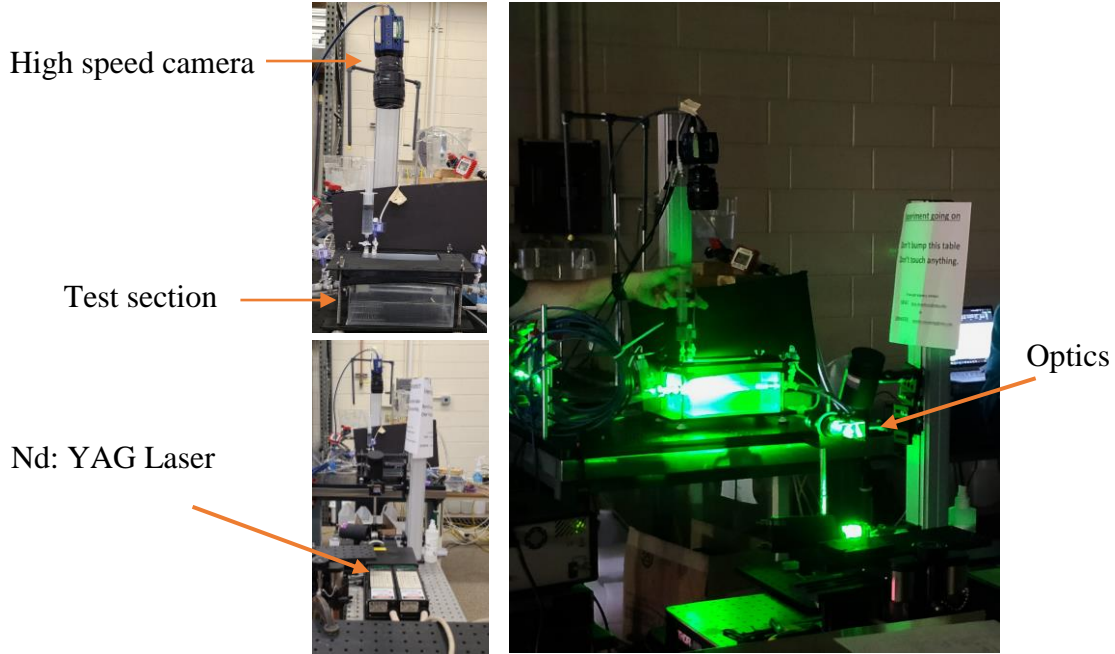


**Figure 16.** PIV set-up for steady flow experiment.

Particle image velocimetry (PIV) was used to measure the velocity field of fluid flow in our pre-determined region. Laser, optics, and camera set-up were as depicted in Figure 16. We used to seed the fluid with 10-micron silver-coated microsphere particles. The flow field was illuminated by a 532 nm Nd:YAG double-pulsed laser. Two laser beams were converted into sheets to illuminate the horizontal plane of the tube. The time interval between two lasers ranged from  $\Delta t=200 \mu s$  to  $\Delta t=500 \mu s$  depending on the flow velocity of each case. The raw images of the particles were captured with a high-resolution PIV camera from the top at 15 Hz. The camera was focused on  $x = 70 \text{ mm}$  to  $x = 150 \text{ mm}$  (mostly downstream of the tube, as shown in Figure 12). The camera and lasers were synchronously triggered by the pulsating pump in each case at the rising edge of the electric signal. During the steady flow experiment, 150 PIV image pairs were taken at a frame rate of 15 Hz for each case. After obtaining the raw images, a cross-correlation analysis was performed among  $16 \times 16$  pixel and then  $8 \times 8$  pixel interrogation windows

with a 50% overlap. For pulsating flow, 200 image pairs were taken with a frequency of 10 Hz, and phase-lock analysis was conducted to provide average flow fields within a cycle.

#### 2.4. Optical Measurements for Tube Deformations

For tube deformations, images were taken by a high-resolution CMOS camera (FLIR Blackfly) at a frame rate of 65 Hz as shown in Figure 17. A black line was drawn at the desired measurement location of the tube. The images were analyzed using a MATLAB algorithm by applying a ‘Lazy Snapping’ method to calculate the deformation area as a function of transmural pressure changes [44].

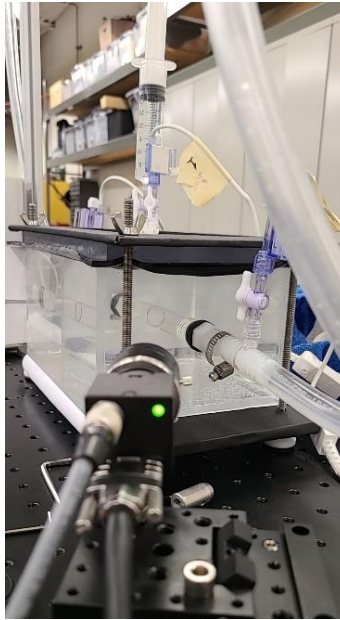


**Figure 17.** High-speed camera captures images during steady flow experiment.

This approach involves two primary steps: Masking and Segmentation. Prior to segmenting the images, the method requires the foreground and background of the desired image to be pre-selected. The segmentation process relies on the Gibbs energy solution outlined in Equation 12:

$$E(X) = \sum_{i \in V} E_1(x_i) + \lambda \sum_{(i,j) \in \mathcal{E}} E_2(x_i, x_j) \quad (12)$$

where  $E_1(x_i)$  is likelihood energy,  $E_2(x_i, x_j)$  is prior energy.  $v$  is the set of all nodes and  $\varepsilon$  is the set of all arcs connecting adjacent nodes.

This method enables users to segment images by simply indicating the foreground and background regions of the image using a few strokes or scribbles. The method then automatically generates a segmentation mask based on these user inputs. ‘Lazy Snapping’ works by computing a graph that represents the image, where each pixel in the image is a node in the graph. The weights of the edges in the graph are determined by the similarity between the pixels they connect. Figure 18 illustrates the way used by this method to segment a region depending on the energy value of particular points.

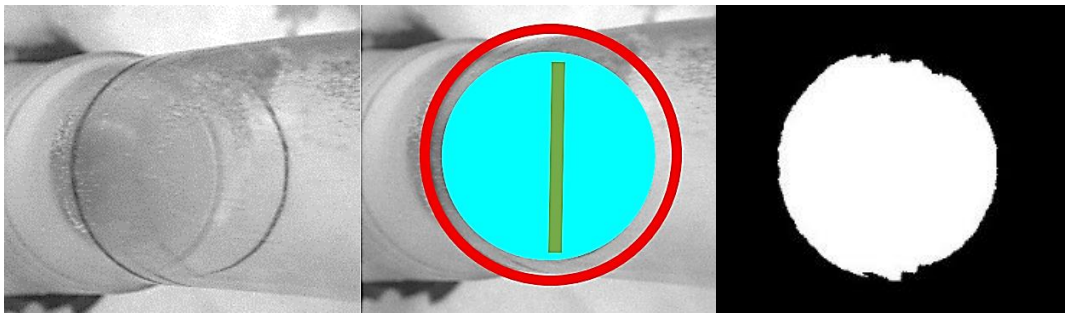


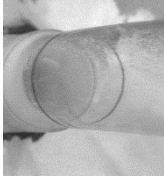
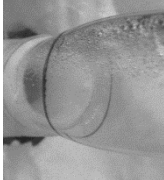
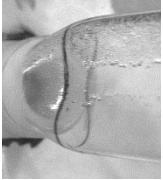
**Figure 18.** Segmentation process using lazy-snapping method. From left to right (a) raw gray-scale image. (b) marking the foreground with a green line and the background with a red circle. (c) segmented black & white image is ready for further analysis.

Before we started the result analysis, a statistical uncertainty analysis was done to identify how closely this method can segment the images in different conditions. The area uncertainty obtained by this method was estimated using repeated measurements of 100 images at the three different collapsed conditions as listed in Table 1. The uncertainty was calculated based on Equation 13 where the z-value was based on a 95% confidence level. From Table 1, it is clear that the automatic segmentation algorithm provides a reliable area measurement from the images with a maximum uncertainty of less than 2% even for extremely deformed scenarios.



$$\mu_{area} = \bar{x}_{area} \pm z \frac{\sigma}{\sqrt{n}} \quad (13)$$

**Table 1.** Area uncertainty statistics

Shape	Circle	Ellipse	Buckled
Conditions			
Area uncertainty (%)	0.66	1.01	1.51

Upon completion of processing the steady flow data, we proceeded to calculate the axial cross-sectional area using the 'Lazy Snapping' tool during the pulsating flow test. Figure 19 illustrates a sample case showcasing various times of a cycle with a flow rate of 1.5 Lpm and a frequency of 60 bpm at  $\Pi = -24.8$ . Due to the pulsation, accurately measuring the area amplitude becomes crucial. However, noise cancellation during data processing can potentially affect peak values. Therefore, selecting the optimal filtration method was imperative to present the data more effectively.

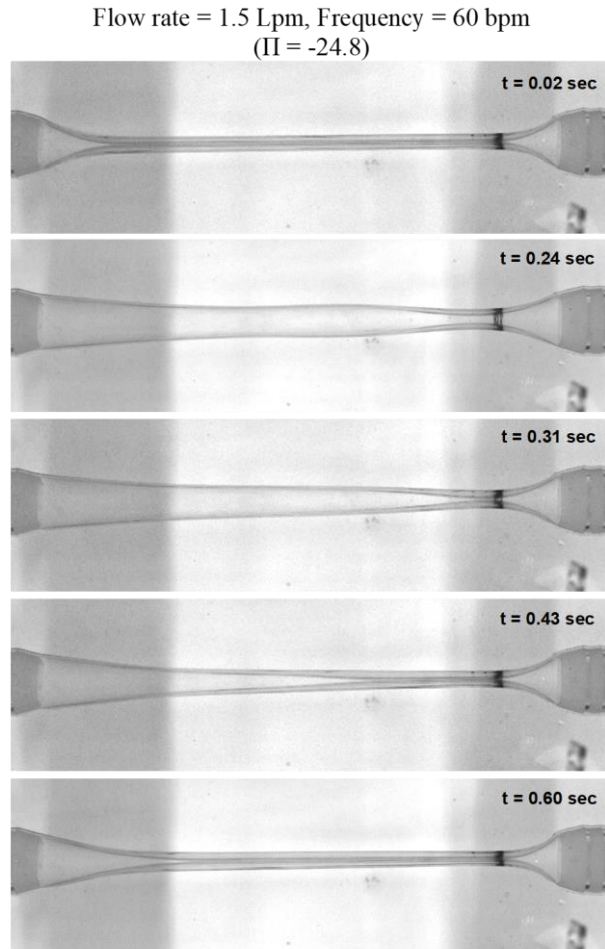


**Figure 19.** A sample case from the pulsating flow test used for filter comparison. The flow rate was 1.5 Lpm with a frequency of 60 bpm at  $\Pi = -24.8$ .

Though moving mean is one of the common ways to filter out the noise in the data set, it might potentially remove the true peak in area amplitude. Therefore, we chose the Savitzky-Golay (S-G) filter to remove the noise, which utilizes the least square smoothing process within a moving window [45]. Least-squares polynomial smoothing involves fitting polynomials to small segments of a data set to approximate it, minimizing the mean-squared error, and iterating this process for each sample position to generate a smoothed output sequence. Savitzky-Golay filters extend this concept by employing least-squares fitting to derive an  $n^{\text{th}}$ -order polynomial that best represents the data set values within the window. The resulting central point of this fitted polynomial curve is then adopted as the updated smoothed data point [46]. In our case, the

window size of 15 was employed to represent the original data as best. A comparison of axial cross-sectional area calculation for 2 complete cycles using a moving mean filter and S-G filter along with original data has been produced in Figure 20. The subsequent filtration process closely matched the original data and maintained a peak nearly identical to the primary data.

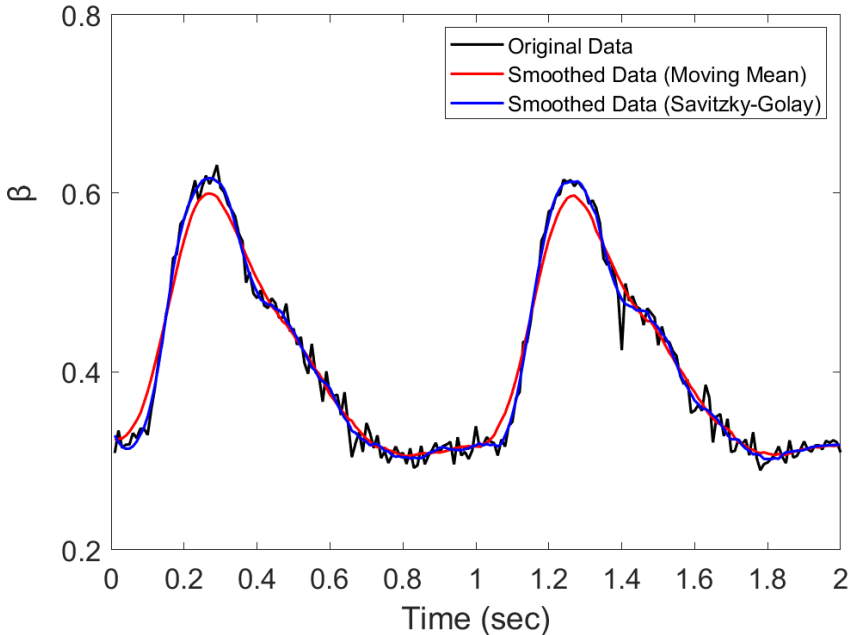


**Figure 20.** Comparison of noise filtration using moving mean filter and S-G filter.  $\beta$  is dimensionless axial cross-sectional area.

### 3. COLLAPSIBLE TUBE UNDER STEADY FLOW

#### 3.1. Introduction

The Starling resistor serves as a standard configuration for studying the deformation of collapsible tubes under varying transmural pressures and pressure gradients. When the transmural pressure goes down significantly negative, the interaction between tube wall deformation and internal pressure of fluid initiates self-excited oscillation. In this experiment, a Starling resistor was integrated into a steady flow loop, as detailed in Chapter 2. Throughout the experiment, pressure, flow rate, and changes in cross-sectional area were monitored. This chapter will delve into the fluid-structure interaction of collapsible tubes under steady flow conditions, focusing on the relationship between pressure and area, critical transmural pressure ranges for initiating self-excited oscillations, self-exciting oscillation frequencies, and downstream pressure waveforms.

Two dimensionless parameters are introduced to quantify the pressure-area relationship in Equations 14 and 15. The normalized transmural pressure,  $\Pi$  is defined as

$$\Pi = \frac{P_{tm}}{K_p} \quad (14)$$

where,  $P_{tm}$  is the measured transmural pressure in mmHg and  $K_p$  is the flexural rigidity defined by Equation 10 in the previous chapter. The normalized cross-section area,

$$\alpha = \frac{A}{A_0} \quad (15)$$

where  $A$  is the measured area and  $A_0$  is the undeformed area at zero transmural condition.

#### 3.2. Test Procedure and Conditions

The experimental setup for steady flow, detailed in Chapter 2, is illustrated in Figure 14. Before testing various steady flow scenarios under varying pressure differences and  $\Pi$

conditions, the tube law was validated using this experimental setup and tube model. Initially, both upstream and downstream flows were inactive, with the inlet and outlet filled with the same fluid mixture and maintained in a stationary state. Pressure was then applied to the pressurized chamber across a range of values. Following data collection and validating tube law, the chamber was integrated into the steady flow loop.

During the steady flow experiment, an adjustable height inlet tank was connected upstream to explore the different pressure heads and achieve the desired Reynolds numbers. Downstream, a long plastic tube submerged beneath the water surface of the reservoir facilitated the generation of sufficient negative pressure to attain higher flow rates. The pressure difference ( $\Delta P$ ) was computed by comparing the fluid mixture head in the inlet tank to the head of the downstream reservoir, with the experiment table surface serving as the baseline. Figure 21 gives an illustration of this setup.

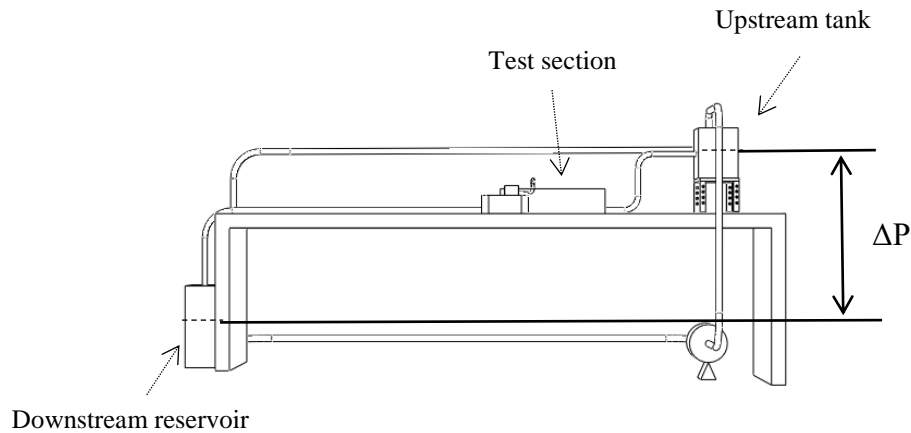


**Figure 21.** Schematic of the difference in pressure head of inlet supply and outlet reservoir during steady flow test.

A programmable syringe pump was used to regulate the chamber pressure, which eventually helped to get the desired transmural pressure. Concurrently, a high-speed camera was continuously capturing images of the collapsible tube from the predetermined angle of  $17^\circ$

between the pressurized chamber's side wall and camera axis. At the same time, pressure data were recorded for 15 seconds for each test case at three different locations (upstream, downstream, and pressure chamber) simultaneously with three individual transducers. The flow meter was positioned immediately after the inlet tank before the inlet tube connected to the pressurized chamber. For these tests, it should be noted that:

- A black line as shown in Figure 22 for cross-section area measurements was drawn at  $x = 137$  mm near the downstream exit of the tube due to the shift of the collapsible location under steady flows. Where for tube law validation, that black line was at  $x = 75$  mm around the center of the tube length.
- For each flow condition, the  $Re$  changed as tube deformed with a decreased  $\Pi$ . Hence, any  $Re$  number used here is the initial  $Re$  number, when the tube was undeformed. Flow was unobstructed when  $\Pi > 0$ .

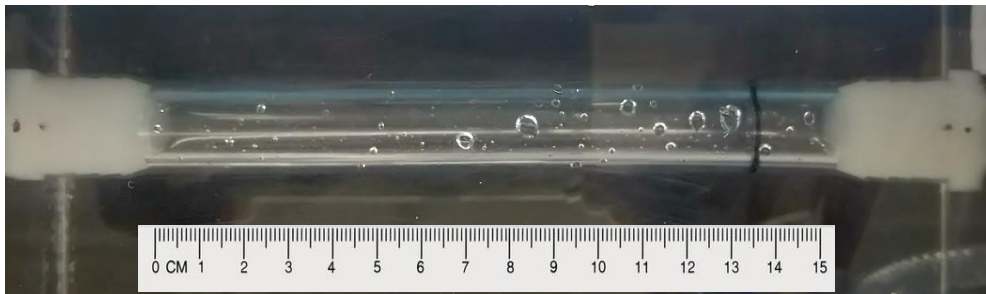


**Figure 22.** A black circle was drawn near the downstream to facilitate the optical analysis.

Using this set-up for steady flow, test conditions were as described below in Table 2. The range of  $\Pi$  is reported from positive extreme to negative extreme. Because the experiment was focused to observe the deformation of the collapsible tube from distended to collapsed condition. For each flow condition, the initial  $Re$  changed as the tube deformed with a decreased transmural pressure and flow was unobstructed when transmural pressure was positive.  $Re$  was defined by  $Re = (\rho Du)/\mu$ , where  $u$  is the average velocity for the corresponding case and was determined

from the average flow rate for that case.  $D$  is inner diameter of the tube. Here, case 1 to case 5 didn't show any self-excited oscillatory movement of the tube wall, but cases 6 and 7 had chaotic self-excited oscillation followed by regular patterned self-excited oscillations in the rest of the cases.

**Table 2.** Steady flow cases

Case	$\Delta P$	Range of $\Pi$	Associated range of Re
1	12.6 mmHg	+35 to -27	200 to 35
2	16.8 mmHg	+39 to -30	400 to 44
3	24.3 mmHg	+37 to -32	600 to 153
4	34.0 mmHg	+43 to -26	800 to 264
5	43.0 mmHg	+37 to -36	1000 to 356
6	60.7 mmHg	+5 to -51	1150 to 595
7	68.6 mmHg	+6 to -56	1300 to 656
8	71.0 mmHg	+14 to -63	1500 to 695
9	87.7 mmHg	+12 to -81	1600 to 651
10	94.3 mmHg	+13 to -84	1700 to 690
11	98.0 mmHg	+14 to -88	1800 to 701

Note: For validating tube law,  $\Delta P$  was 0 mmHg and  $\Pi$  applied from +10 to -31.

### 3.3. Static Deformation of the Tube: A Validation against Tube Laws

The first result we obtained was the static deformation of the tube to validate our thin-walled tube deformation against the classic tube law. The experiments were done by controlling the chamber pressure only under no flow conditions, changing the transmural pressure from highly positive to highly negative. For this test, a black circle was drawn at the middle of the tube length.

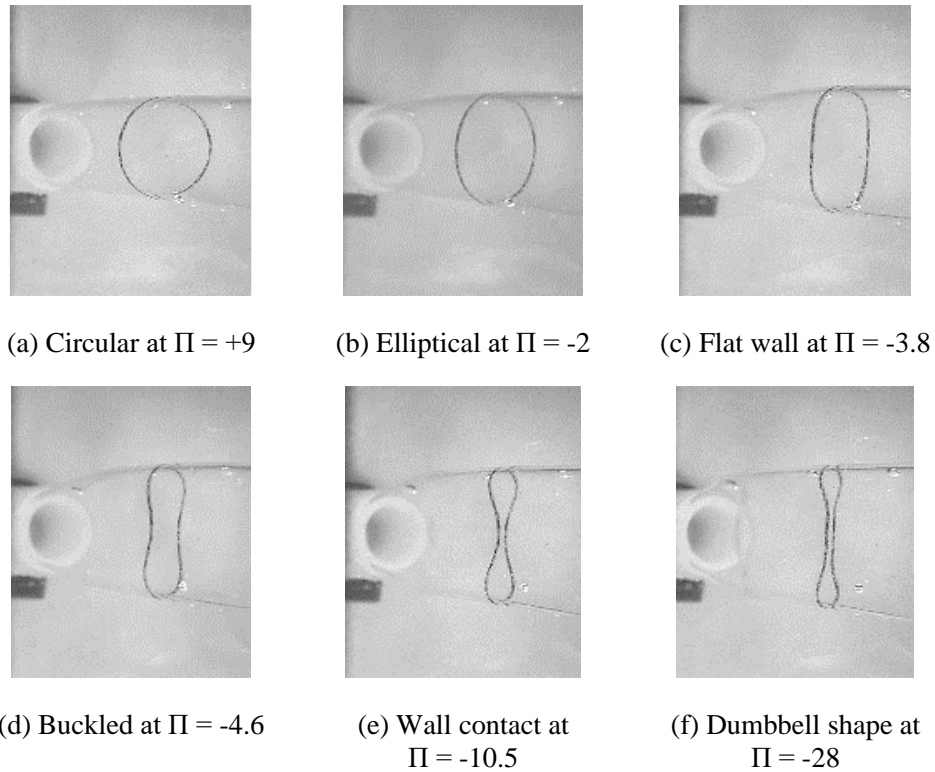


**Figure 23.** Images of the cross-sectional shape at the middle of the tube ( $x = 75$  mm) under ‘no-flow’ condition with varied transmural pressures.

Figure 23 shows that as  $\Pi$  decreases from +9 to -28, the middle cross-section of the tube gradually deforms and eventually collapses because the material's bending stiffness is unable to withstand the external forces. The evolution of deformation due to the transmural pressure change can be described as (a) circle to (b) ellipse and (c) flat-wall oval, followed by (d) buckled tube, (e) critical wall contact, and then eventually (f) collapsed dumbbell shapes. In addition, the deformation always occurs in a preferred direction (oriented in the vertical plane in the setup), because the collapsible tube cross-section isn't a perfect circle under positive transmural pressure. Though most of the research on collapsible tubes assumes the cross-sectional area of the tube is very circle at positive transmural pressure, perfect circle doesn't exist in physiological contexts. Most of the biological vessels including veins are not circular in cross-section. Rather, these vessels possess a shape close to the ellipse, where external pressure on the tube compels it



to deform through the minor axis [47]. In Figure 20, the results are quantitatively compared with the tube laws for collapsible tubes with a finite thickness. The theoretical equation was provided by Kozlovsky et al. [15] as the following:

$$\Pi_{(\alpha,\gamma)} = 3.1 \left( \alpha^{\left( \frac{60}{\gamma^{0.5}} - 65 \right)} - \alpha^{(0.7\gamma-0.4)} \right) \quad (16)$$

where  $\gamma$  (ratio of wall thickness to radius of the tube) equals 0.093 in our experiments. This resulted in a theoretical prediction curve (red line) in Figure 24. The strong correlation between our experimental data and the theoretical model confirmed that the tube deformation followed the classical tube law under the quasi-1D assumptions.

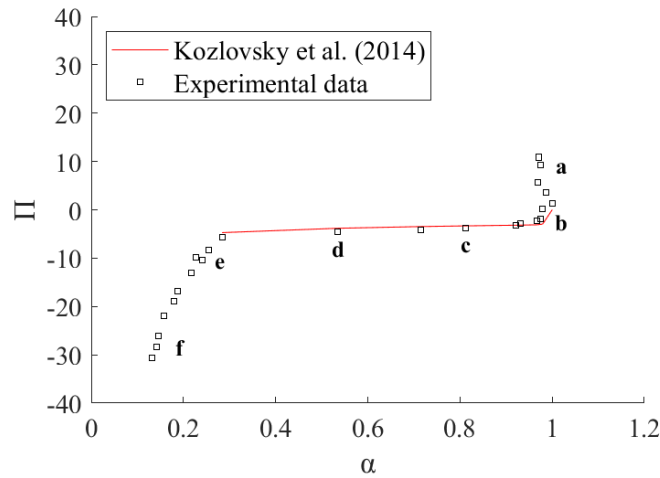


**Figure 24.** Nondimensional cross-sectional area of collapsible tube vs.  $\Pi$  compared with a theoretical model. Letters a through f correspond to the states of deformation illustrated in Figure 23.

### 3.4. Fluid-Structure Interactions under Steady Flows

#### 3.4.1. Tube Deformation

The steady flow-induced tube deformation ( $\alpha$ ) under varied transmural pressures ( $\Pi$ ) was studied within a range of  $\Delta P$  from 12.6 mmHg to 98.0 mmHg (corresponding initial Re from 200 to 1800). Figure 25 shows the  $\Pi$ - $\alpha$  curves for the  $\Delta P = 12.6\text{mmHg} - 43.0\text{ mmHg}$  range,

compared with the no-flow condition  $\Delta P = 0$  mmHg ( $Re = 0$ ). From the results, we can see that the curves closely follow the theoretical tube law prediction when  $\Delta P$  was hanging around or below 43.0 mmHg. The  $\Pi$ - $\alpha$  relation suggests that the deformation induced by transmural pressure remained relatively independent of  $\Delta P$  when the pressure difference was relatively low. It has been also noticed that when transmural pressure approached below zero, even small changes in  $\Pi$  made a larger reduction in cross-sectional area. But after a certain range of  $\Pi$ , mostly around -10, the distensibility of the tube material ( $D$ ) became very low. Therefore, additional external pressure on the tube could not expedite the reduction in the area.

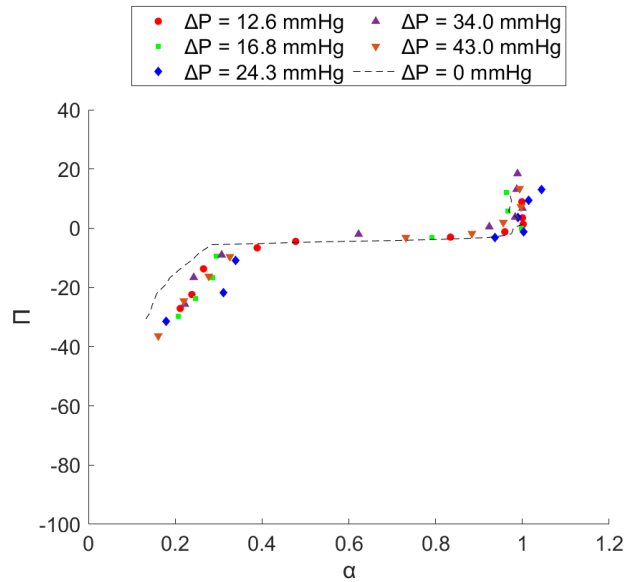


**Figure 25.** Nondimensional transmural pressure vs area curves under steady flows:  $\Delta P = 12.6$  mmHg to 43.0 mmHg, no self-excited oscillation.

In Figure 26, the deformation of the tube cross-section is depicted for case 5, where  $\Delta P$  was 43 mmHg with an initial Reynolds number of 1000. It is evident that for  $\Pi$  ranging from -1.8 to -9.6, the tube deformed rapidly. However, upon reaching  $\Pi = -16.3$ , further increases in negative pressure did not significantly reduce the area. Although this range of  $\Pi$  varied slightly

for other non-oscillating cases, the trend of deformation remained similar. No discernible self-excited oscillation was observed within these  $\Delta P$  cases.

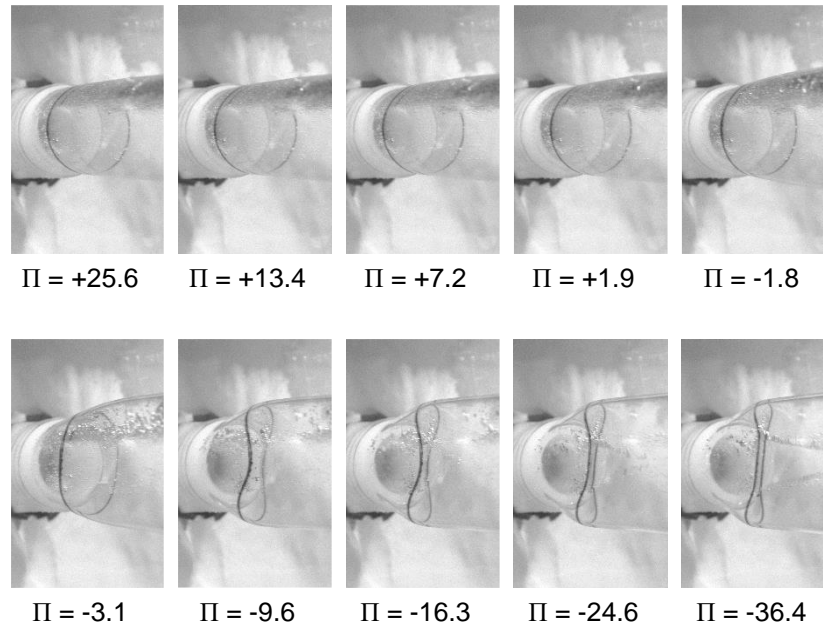


**Figure 26.** Cross-sectional area was reduced when  $\Pi$  went negative with a shape deformation from circle to dumbbell shape at case 5 ( $\Delta P = 43$  mmHg).

### 3.4.2. Self-Excited Oscillation

As we increased  $\Delta P$  to above 60.7 mmHg, noticeable deviations emerged from previous conditions, as shown in Figure 27. Within specific ranges of negative  $\Pi$ , unstable fluid-structure interaction ensued during cases 6 to 11, leading to self-excited oscillations (marked by the large gap suggested by the dashed line box in Figure 23). Raw images have been provided in Figure 28 for the first cycle of self-excited oscillation of  $\Delta P = 94.3$  mmHg case under  $\Pi = -30$  and Figure A1 in Appendix demonstrates the self-excited oscillatory movement of the tube wall during  $\Delta P = 98.0$  mmHg case. The results suggest that as  $\Delta P$  increased, the ranges of  $\Pi$  within which self-excited oscillation might occur also increased significantly. The higher the pressure difference was, the more negative  $\Pi$  was required to completely collapse the tube to end the self-excited

oscillation. All the reported  $\Pi$  during self-excited oscillation are the mean downstream transmural pressure.

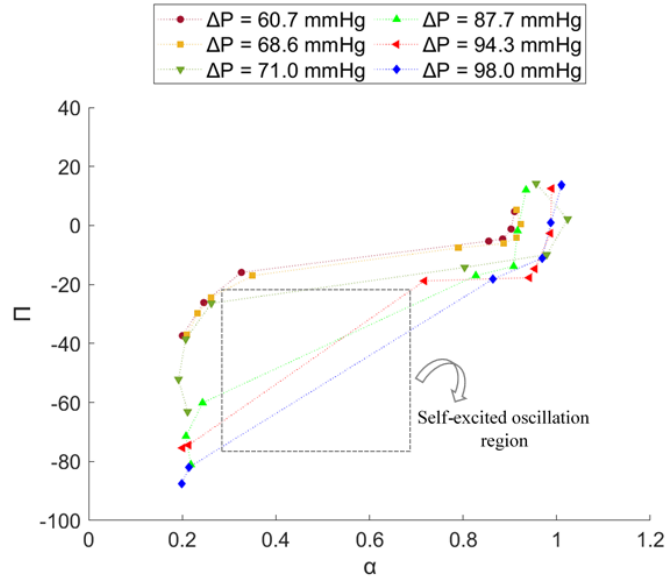


**Figure 27.** Nondimensional transmural pressure vs area curves under steady flows:  $\Delta P = 60.7$  mmHg to 98.0 mmHg, self-excited oscillation observed.

The self-excited oscillations stem from the coupling of the tube's elastic characteristics with the fluid dynamics. Upon surpassing a critical pressure difference across the tube, the walls deformed and the tube became constricted, triggering flow instability. The flow instability, in turn, impacted the tube's wall, leading to the initiation of self-excited oscillations. Such behavior is typical in collapsible tubes with low stiffness, particularly under negative transmural pressures that increase the likelihood of tube wall collapse. In most cases, the critical velocity for self-excited oscillation remained around 0.3 m/s, aligning closely with the aforementioned predicted value using  $U_{crit} = \sqrt{\frac{K_p}{\rho}}$ . Figure 24 illustrates a self-excited oscillation case at  $\Delta P = 94.3$  mmHg and  $\Pi = -30$ . Under this condition, a complete cycle of self-excited oscillation took approximately 0.73 seconds (frequency = 1.37) and the cross-section deformed back and forth between “buckled” and “dumbbell” shapes

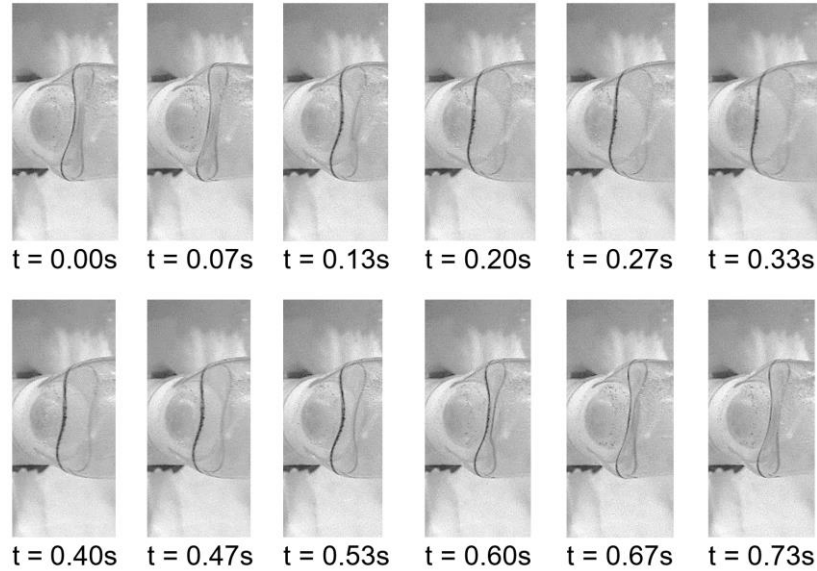


**Figure 28.** Images of the cross-section of the collapsible tube during the first cycle of self-excited oscillation at case 10 ( $\Delta P = 94.3$  mmHg) when  $\Pi = -30$ .

#### ***3.4.2.1. Downstream transmural pressure amplitude and waveform***

Another interesting phenomenon we observed is that neither the frequency nor the magnitude of the self-excited oscillation is constant as we keep decreasing the negative transmural pressure. These effects are demonstrated in Figure 29, which shows the transmural pressure fluctuations downstream of the tube. Under three  $\Delta P$  cases, it can be seen that as the magnitude of mean negative  $\Pi$  increased, the self-excited oscillation introduced an increased amplitude of pressure fluctuations. In addition, the frequency of the self-exciting oscillation also increased which will be discussed in detail later. Self-excited oscillation patterns were also distinct in each case, suggested by the pressure curves. In the lower range of negative  $\Pi$ , the oscillation was LU-type (Lower frequency – spent most time above mean pressure) and it gradually changed to LS-type (Large Sine) until the end of the self-excited oscillation. Truong and Bertram (2009) also mentioned this LS-type during self-excited oscillation, is considered one of the most common self-excited oscillation patterns downstream of collapsible tubes [48]. No LD-type self-excited oscillation pattern was observed in this study.

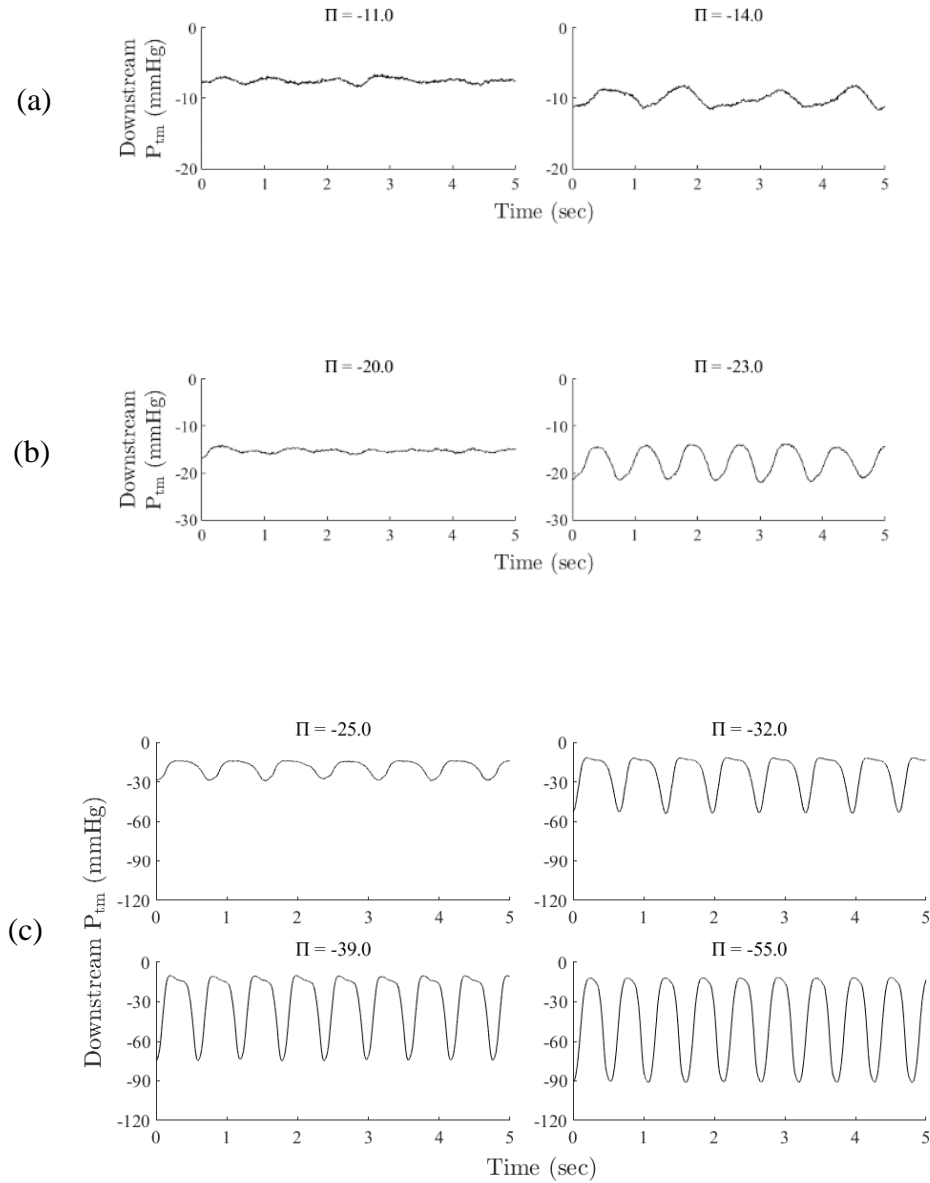


**Figure 29.** Transmural pressure waveforms downstream of the tube showing self-excited oscillations: (a)  $\Delta P = 68.6$  mmHg (Irregular waveform); (b)  $\Delta P = 71.0$  mmHg; (c)  $\Delta P = 87.7$  mmHg.

Though the pressure gradient went even higher than 90 mmHg, the response in downstream transmural pressure under varied  $\Pi$  followed the same pattern. In Figure 30, self-excited oscillation started around  $\Pi = -25$  to  $-30$  and sustained until the tube got collapsed by touching walls leading to a dumbbell shape. Also the waveform during self-excited oscillation transformed from LU to LS-type under more negative transmural pressure.

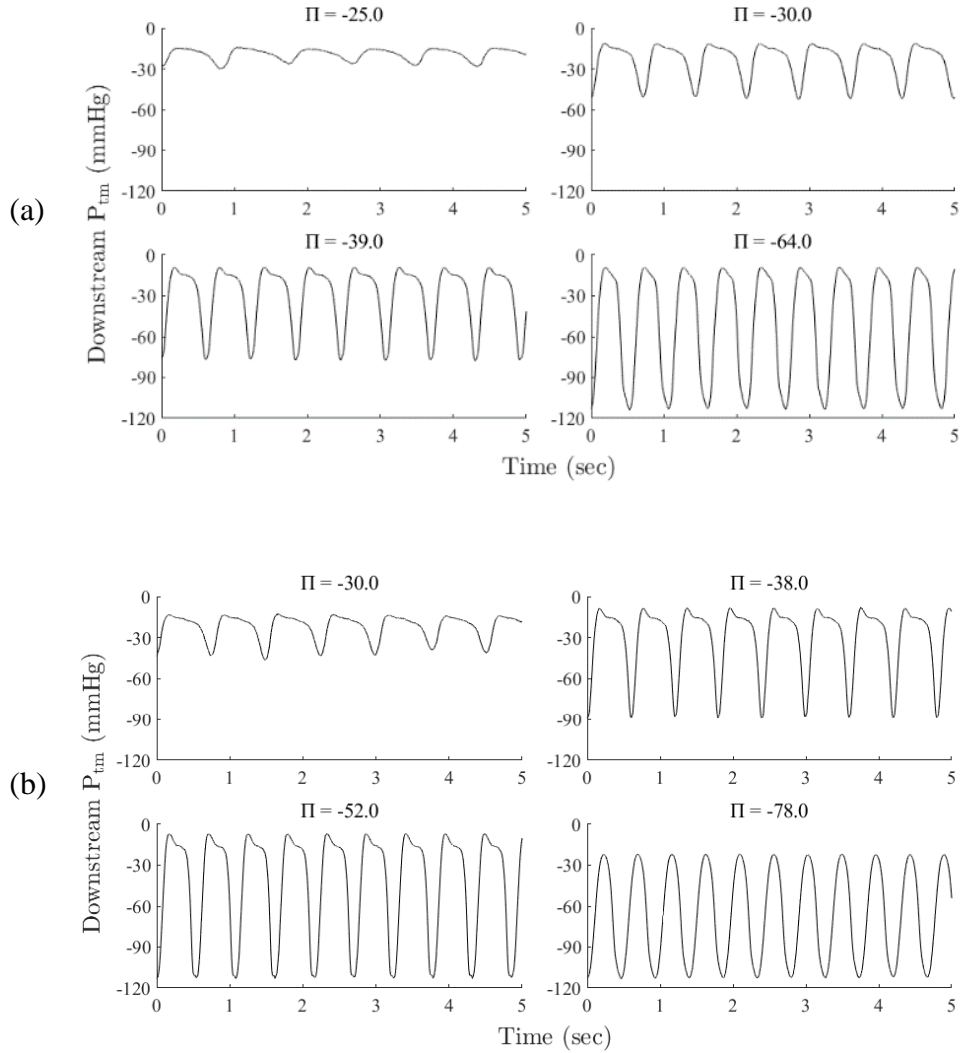


**Figure 30.** Transmural pressure waveforms downstream of the tube during self-excited oscillations continued for even higher-pressure gradients: (a)  $\Delta P = 94.3$  mmHg; (b)  $\Delta P = 98.0$  mmHg.

### 3.4.2.2. Frequency of self-excited oscillation

It is also interesting to note that when  $\Delta P$  is relatively low as in Figures 29(a) and 29(b), the self-excited oscillation shows a relatively chaotic pattern. As  $\Delta P$  increased and initial  $Re$  became higher, the self-excited oscillation pattern became more regular. This was further demonstrated by the fast-Fourier transformation results. In Figure 31, it can be seen that as  $\Delta P$  increased, the peak frequency became increasingly distinguishable with high-frequency components diminishing. Furthermore, the dominant frequency was  $1.8 \text{ Hz}$ ,  $2.2 \text{ Hz}$ , and  $2.5 \text{ Hz}$  for

case 9 in Figure 31(d), case 10 in Figure 31(e), and case 11 in Figure 31(f), respectively, showing an increasing trend as  $\Delta P$  increases. In addition, under the same  $\Delta P$ , the self-excited oscillation frequency increased when  $\Pi$  developed more negative. For example, in case 10 with  $\Delta P = 94.3$  mmHg, a self-excited oscillatory movement started in the tube with a frequency of 1.3 Hz around  $\Pi = -30$ . In that case, with more negative  $\Pi$ , the frequency jumped up to a maximum of 2.2 Hz as discussed earlier.

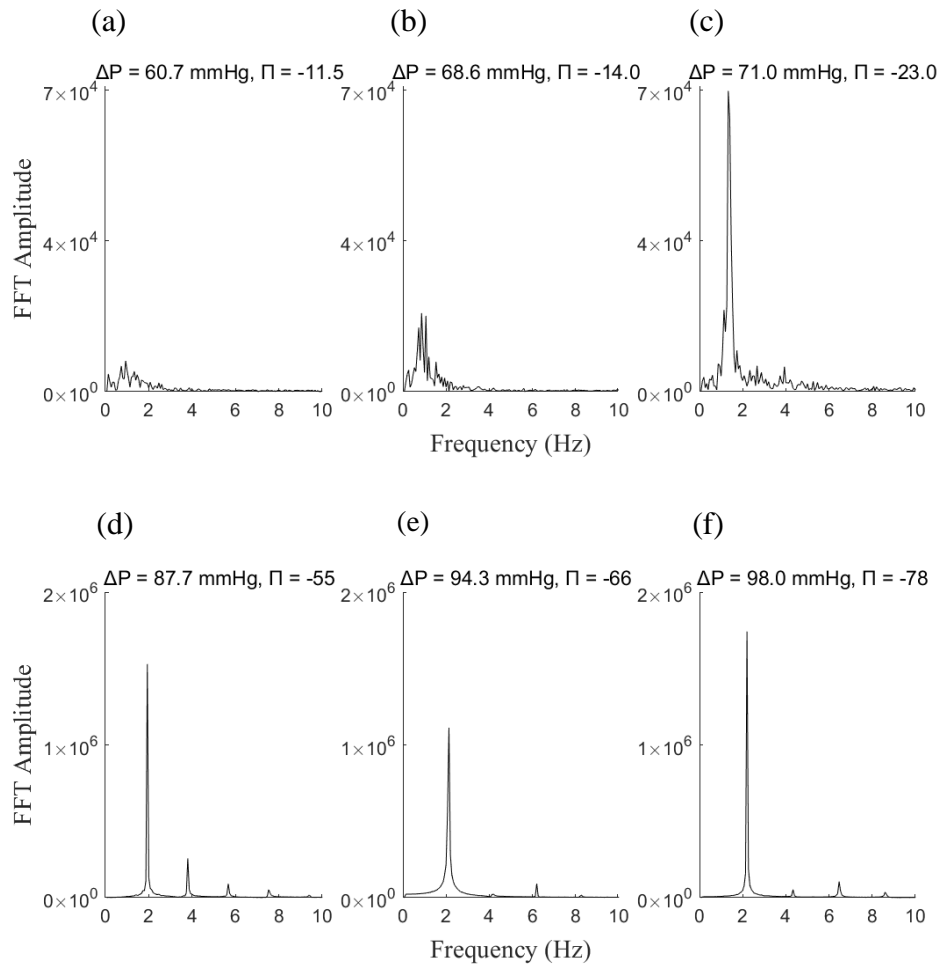


**Figure 31.** The dominant frequency of self-excited oscillations under different pressure gradients.



### 3.4.2.3. *Self-exciting cross-sectional area oscillation amplitude*

Figure 32 shows the amplitude of the self-excited oscillation in terms of the radial cross-sectional area for steady flow cases 9, 10, and 11, where regular patterned self-excited oscillations were triggered. In these  $\Pi$ - $\alpha$  curves, data with error bars show the fluctuation of the nondimensional area,  $\alpha$  due to self-excited oscillations. It is evident that the amplitude of the area during self-excited oscillation peaked around the middle of the  $\Pi$  range for each  $\Delta P$  case, rather than monotonically increasing with the magnitude of negative  $\Pi$ . In strongly negative  $\Pi$  conditions, the tube was significantly buckled, leaving less room for the wall's self-excited oscillatory motions. Overall, this result indicates that there exists a critical  $\Pi$  under each flow condition, where the maximum amplitude of wall motion during self-excited oscillation is expected (typically near the middle of the self-excited oscillation  $\Pi$  range). Additionally, as  $\Delta P$  increased, the range of the maximum amplitude became larger. In Figure 32(a), the range of maximum amplitude was  $\alpha = 0.15$  to  $0.6$ , whereas in Figure 32(c), this range went for a wider range of  $\alpha = 0.15$  to  $0.7$ .

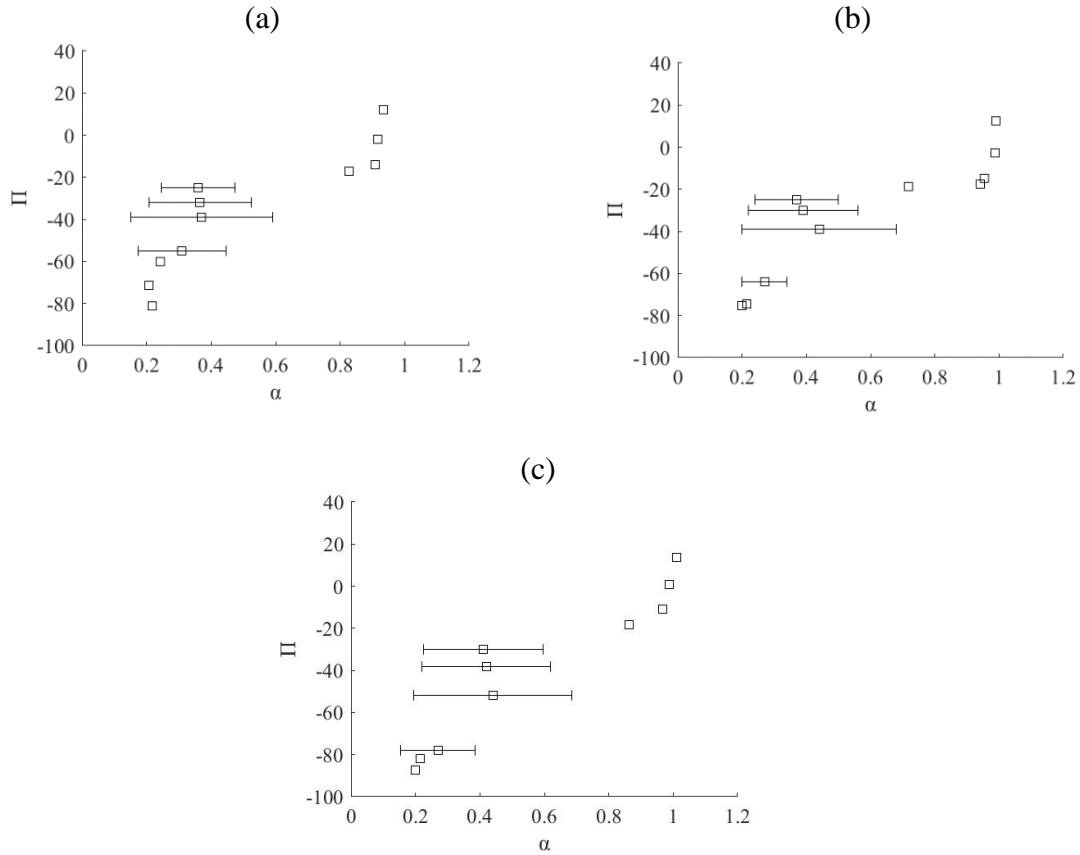


**Figure 32.** Cross-section area amplitudes during self-excited oscillations: (a)  $\Delta P = 87.7$  mmHg; (b)  $\Delta P = 94.3$  mmHg; (c)  $\Delta P = 98.0$  mmHg.

### 3.4.3. Flow Limitation Effect in Steady Flow

By employing a flow meter upstream of the flow loop, we recorded cumulative volume over time in each instance. Using this data, we determined the average flow rate ( $Q$ ) in liters per minute. This determination was further confirmed by the instantaneous average flow rate data directly recorded from the flow meter.

#### 3.4.3.1. Flow rate alteration under negative transmural pressure

When downstream transmural pressure dropped below zero, there was a significant change in the flow rate across all test conditions due to the tube deformations. From Figure 33(a), it is evident that in all the non-oscillating scenarios (cases 1 – 5), the flow rate was independent of downstream transmural pressure until  $\Pi$  reached zero. When  $\Pi$  became negative,

the flow rate decreased in all the  $\Delta P$  cases. Though the flow rate dropped to approximately 0 liters per minute for two lower  $\Delta P$  cases at 12.6 mmHg and 16.8 mmHg,  $\Delta P = 24.3 - 43.0$  mmHg cases maintained a little flow even under highly negative  $\Pi$ .

On the contrary, Figure 33(b) illustrates the flow rate vs. transmural pressure in cases where self-excited oscillations occurred. In these cases, the  $\Delta P$  was sufficiently large to maintain flow above 1.0 liters per minute even when  $\Pi$  went significantly negative. It was also noticed that until the onset of self-excited oscillation around  $\Pi = -20$ , there was no remarkable reduction in flow rate. However, once self-excited oscillation commenced, the average flow rate dropped down. But the tube kept a descent average flow rate even under highly negative transmural pressure. The periodic opening of the tube during self-excited oscillation attained a peak flow rate, which eventually helped to maintain the average flow rate at specific  $\Pi$  values under any  $\Delta P$  condition.

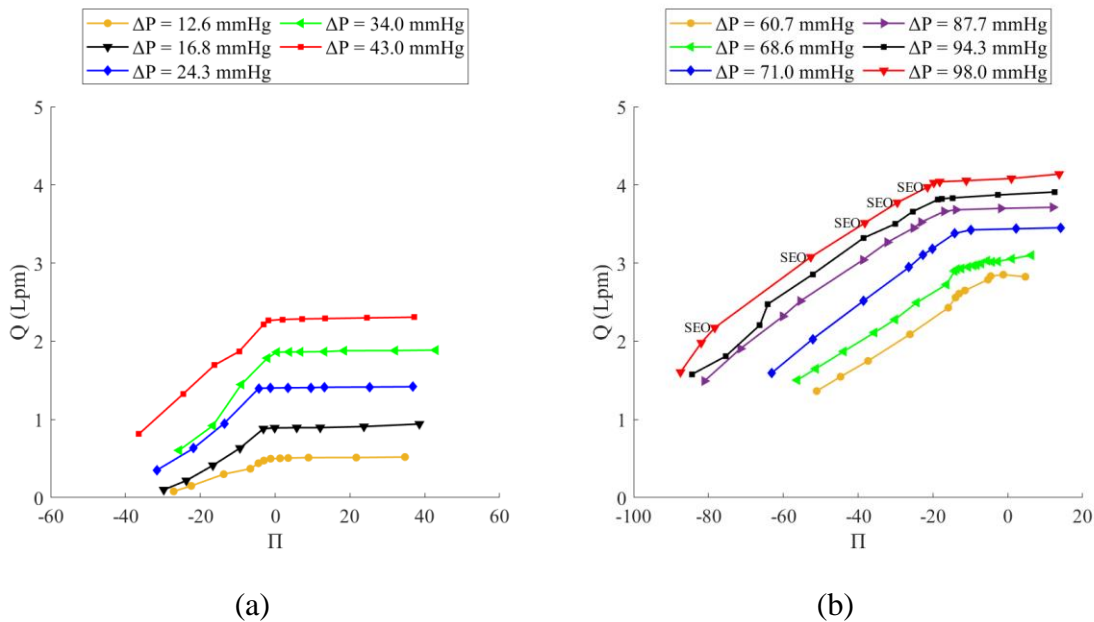


**Figure 33.** Change in the flow rate under reduced downstream transmural pressure: (a) Non-oscillating cases; (b) Self-excited oscillatory cases.

Note: SEO means self-excited oscillation on the plot of  $\Delta P = 98.0$  mmHg curve from self-excited oscillatory cases.

### 3.4.3.2. Flow resistance in steady flow

Flow resistance during the steady flow was measured under varied  $\Delta P$  to compare the changes in resistance to flow when  $\Delta P$  changes. Firstly, the Darcy friction factor,  $f$  was calculated by Equation 17, as this experiment utilized laminar flows.

$$f = \frac{64}{Re} \quad (17)$$

Using this  $f$ , Darcy-Weisbach equation gave major losses through the collapsible tube. Minor losses through the tubing were negligible. Considering the major losses, resistance ( $R$ ) was found for each case by Equation 18.

$$R = \frac{\Delta P'}{Q} \quad (18)$$

where  $\Delta P'$  measures the exact pressure difference of upstream and downstream on the unsupported portion of the collapsible tube.  $Q$  was the flow rate during that specific case. From Figure 34, it can be observed that within a certain range of  $\Pi$ , resistance remained consistently low despite the decreasing transmural pressure. For non-oscillating cases in Figure 34(a), resistance surged immediately after exposure to negative transmural pressure. The highest resistance was observed in the case with the lowest  $\Delta P$  (12.6 mmHg). As Reynolds number elevated with increased  $\Delta P$ , the peak resistance of  $5 \times 10^{-3}$  mmHg.s/mm<sup>3</sup> was dropped down to  $2.2 \times 10^{-3}$  mmHg.s/mm<sup>3</sup>.

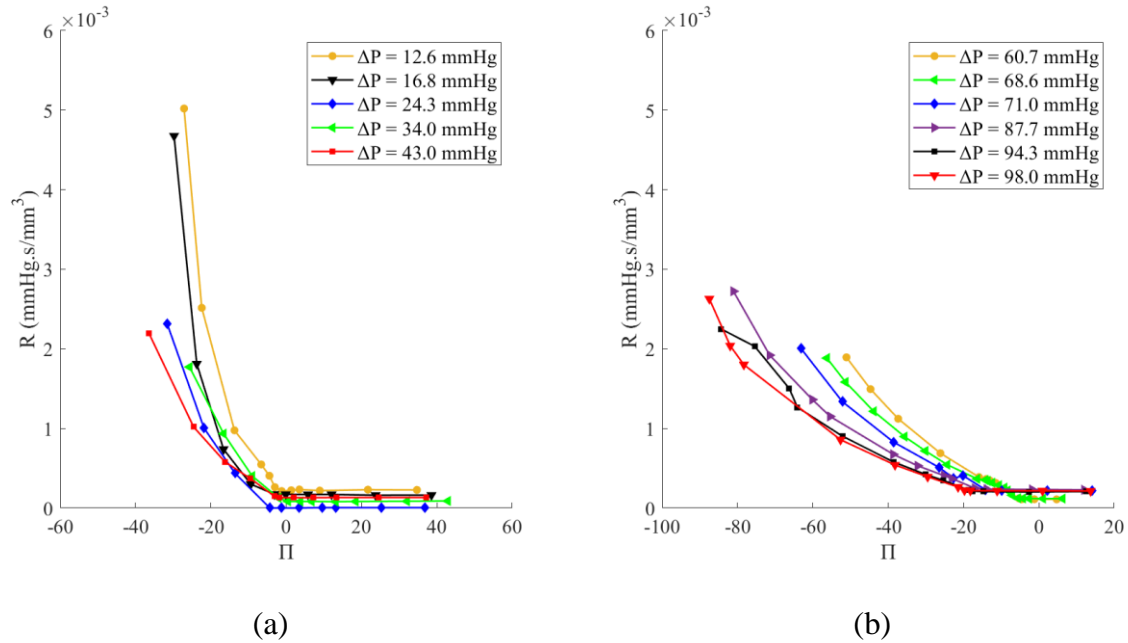


**Figure 34.** Change in the flow resistance: (a) Non-oscillating cases; (b) Self-excited oscillatory cases.

In instances of self-excited oscillations, as  $\Delta P$  increased further, the change in resistance was significantly different from cases without self-excited oscillations. Notably, resistance remained relatively stable until  $\Pi$  reached -10 to -20, where the self-excited oscillation was typically initiated. As plotted in Figure 34(b), when transmural pressure became sufficiently negative, resistance rose to a maximum of  $2.8 \times 10^{-3}$   $\text{mmHg}\cdot\text{s}/\text{mm}^3$  which was halfway of the maximum resistance we observed in  $\Delta P = 12.6$  mmHg case. However, this elevation in resistance during self-excited oscillatory cases occurred over a broader range of negative  $\Pi$  compared to non-oscillating  $\Delta P$  cases. Overall, it can be concluded that the self-excited oscillation leads to a decreased average flow resistance for fluid transport in collapsible tubes.

### 3.5. Flow Field Analysis Based on PIV Data

In the earlier section of this chapter, we observed the onset of self-excited oscillations characterized by a regular patterned waveform in steady flow cases 9 to 11. Consequently, to

analyze the flow field under a  $\Delta P$  of 94.3 mmHg, we employed particle image velocimetry (PIV). Several instances of  $\Pi$ , including critical ones linked with self-excited oscillations, were investigated. Table 3 provides an overview of the selected cases of tube deformation, self-excited oscillation, etc.

**Table 3.** Range of  $\Pi$  at  $\Delta P = 94.3$  mmHg for PIV analysis

PIV Case	$\Pi$	Tube deformation	Self-excited oscillation Condition
A	-0.6	Not collapsed	No Oscillation
B	-19	Partially collapsed	Irregular vibration
C	-27	Collapsed	Onset of oscillation
D	-29	Collapsed	Oscillating
E	-30	Collapsed	Oscillating
F	-39	Collapsed	Oscillating
G	-50	Collapsed (Walls touched)	Oscillation stopped

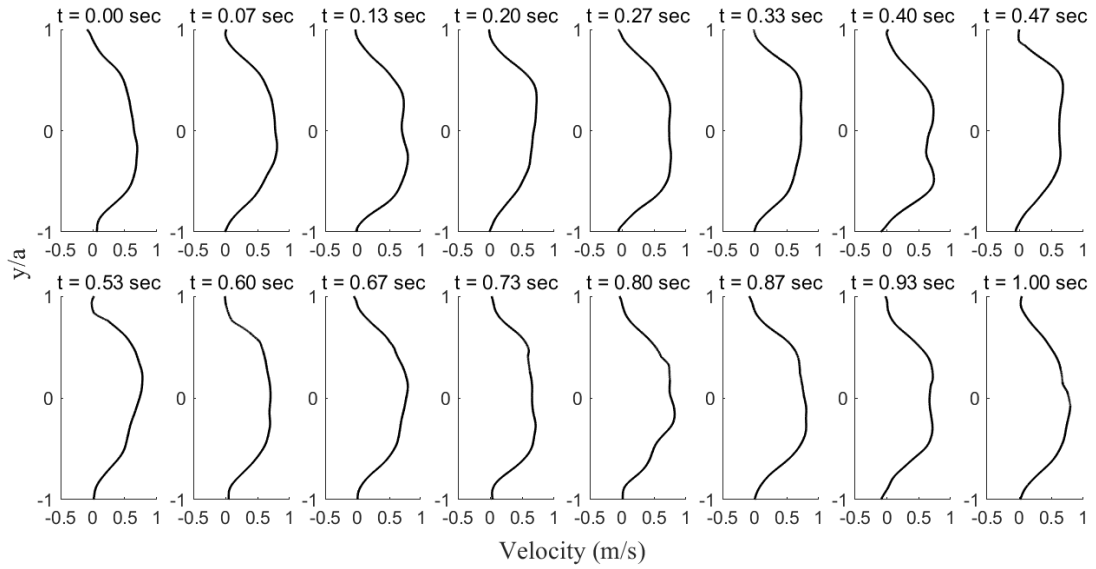
The PIV results of three critical conditions (case B, E, and F from Table 3) are shown in Figures 35-40. The latter two  $\Pi$  cases showed self-excited oscillations with increasing magnitude and frequency.

### 3.5.1. Velocity Fluctuation during Self-Excited Oscillation

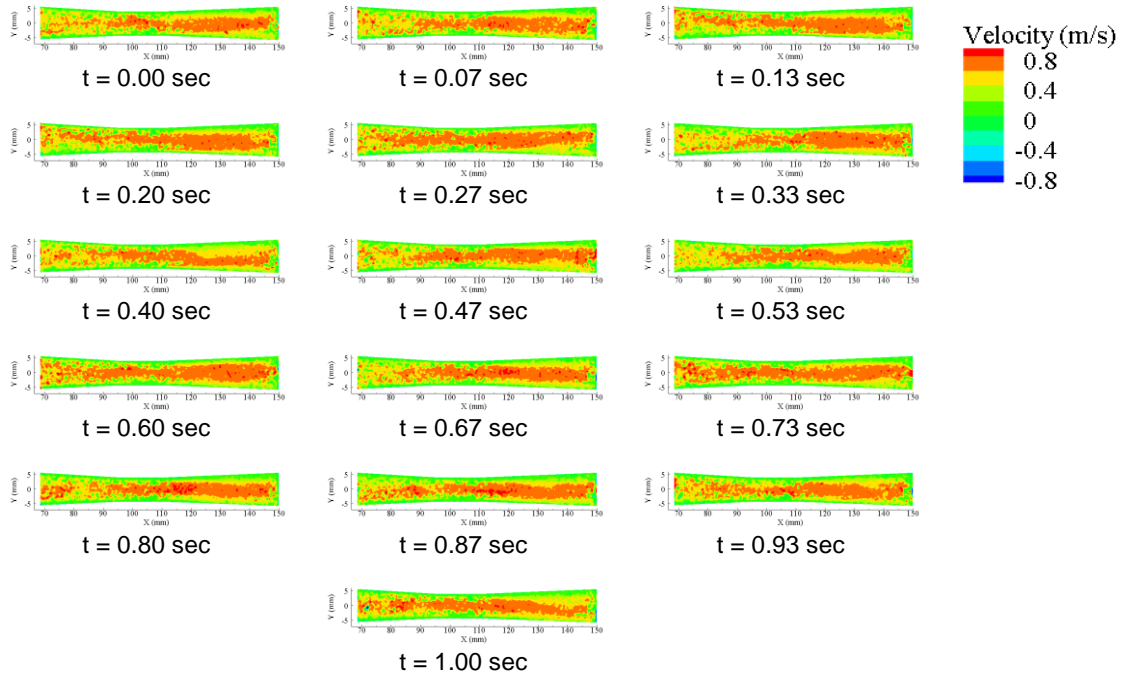
For plotting the velocity profile around the downstream, the velocity data have been extracted at  $x = 120$  mm (Figure 13 in Chapter 2), just before the collapse location. The y-axis was nondimensionalized ( $y/a$ ) through the division of  $y$  values by  $a$ , where  $a$  is the width of the flow channel on the measured plane. The value of  $a$  was different depending on whether the tube was fully open, partially collapsed, or fully collapsed.

At  $\Delta P = 94.3$  mmHg and  $\Pi = -19$  (Figure 35), the flow remains almost constant with only slight variations in velocity profiles, suggesting no self-excited oscillations but only small perturbations existing in the tube flow. The velocity profiles were almost flat at the center around  $y/a = 0$  and the average velocity was found 0.3 m/s, which was nearly critical to initiate the

self-excited oscillation. Figure 36 with the velocity color map also supports this result, where we see a continuous jet through the horizontal axis of the tube. The results suggest at a low magnitude of negative  $\Pi$ , the system can remain relatively stable. The initial onset of the tube's self-exciting oscillation was found at  $\Pi = -25$  for  $\Delta P = 94.3$  mmHg.



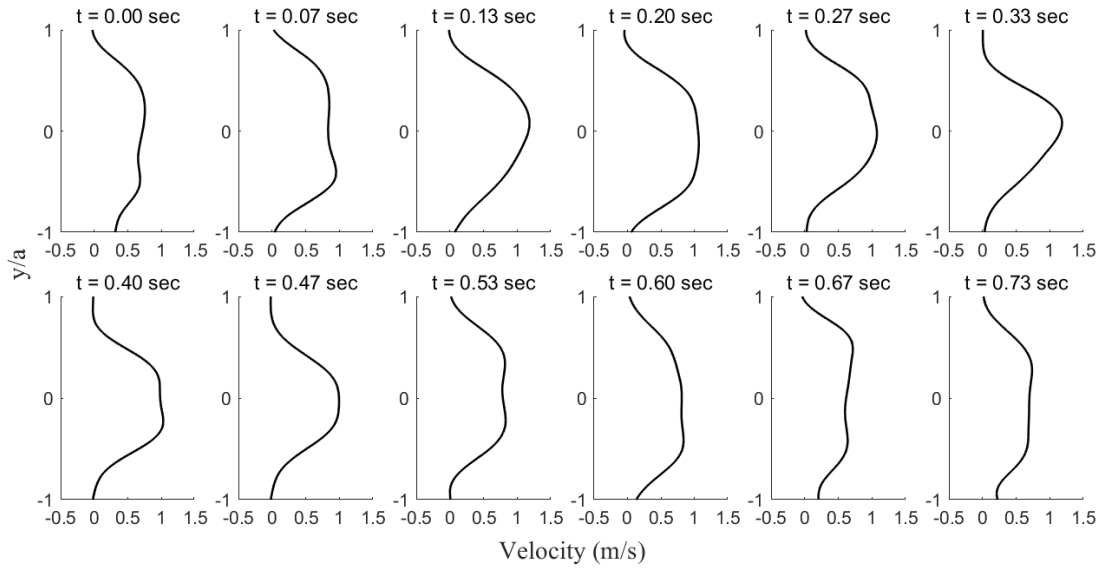
**Figure 35.** Velocity profiles at different time steps for 1 sec at  $\Delta P = 94.3$  mmHg and  $\Pi = -19$  case.



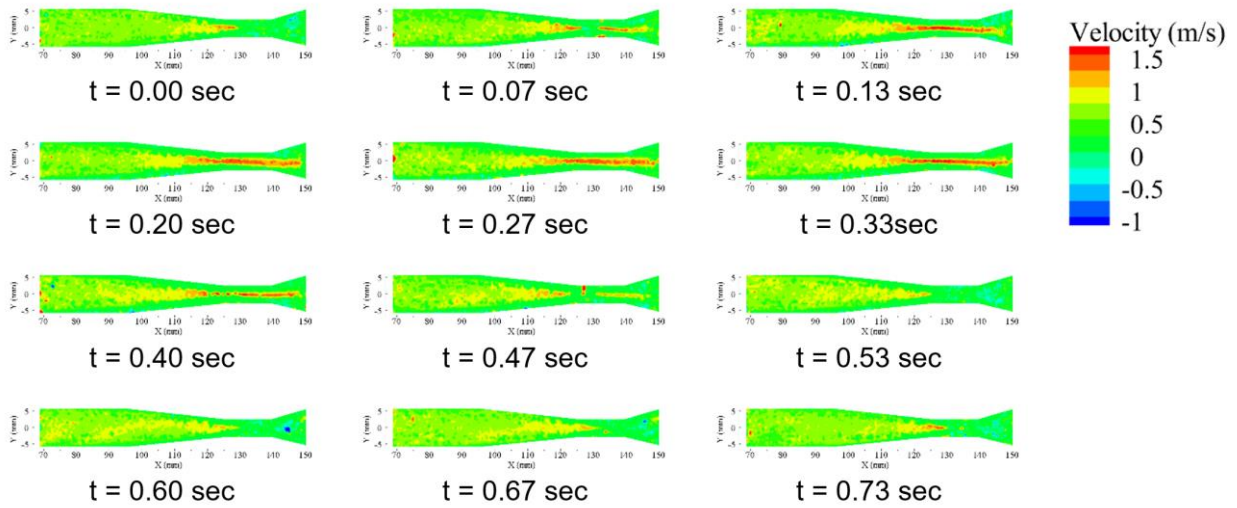
**Figure 36.** Continuous jet through the partially collapsed tube for 1.00 sec at  $\Delta P = 94.3$  mmHg and  $\Pi = -19$  case. No self-excited oscillation was observed.

Figures 37 and 38 show the velocity profiles and the flow fields during the first cycle ( $t = 0.00$  to  $0.73$  sec) of self-excited oscillation for  $\Pi = -30$  at  $\Delta P = 94.3$  mmHg. It can be seen that the rises and falls of the jet flow are induced by the self-excited oscillation during a cycle, with the highest velocity of  $1.2$  m/s measured at  $t = 0.33$  sec, which is at approximately the middle of the self-excited oscillation cycle. The average velocity during this cycle was  $0.33$  m/s. At the peak of the jet flow, it is also noticeable that the jet was asymmetrical about the tube center. This phenomenon was constantly observed during multiple cycles (which will be discussed in the next section), which is likely similar to the asymmetrical vortex shedding.





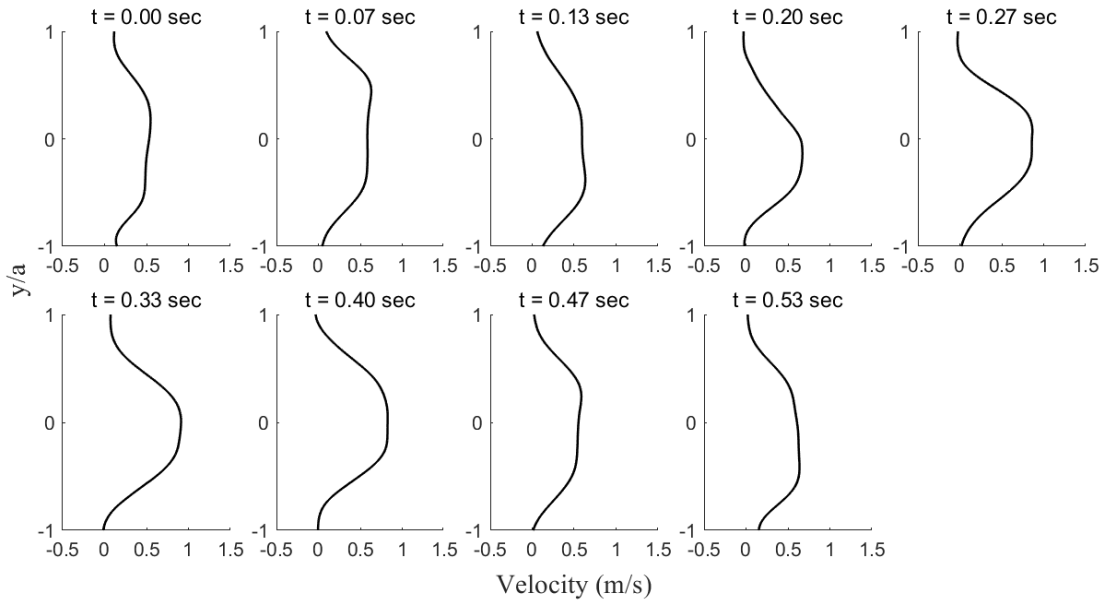
**Figure 37.** Velocity profiles during one cycle of self-excited oscillation at  $\Delta P = 94.3$  mmHg and  $\Pi = -30$  case.



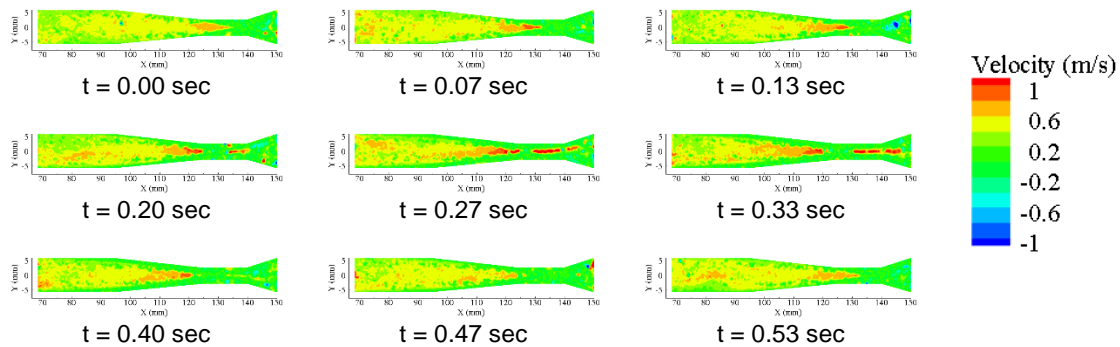
**Figure 38.** Periodic jet through the collapsed tube during one cycle of self-excited oscillation  $\Delta P = 94.3$  mmHg and  $\Pi = -30$  case.

Figure 39 presents another scenario in the same  $\Delta P$  case, but  $\Pi$  is more negative at  $\Pi = -39$ . It was evident that as  $\Pi$  became more negative, the frequency of the jet flow became higher as the first cycle of self-excited oscillation ended at  $t = 0.53$  sec. Both the peak flow velocity and average velocity dropped to  $0.93$  m/s and  $0.3$  m/s, respectively, due to more flow restrictions.

Moreover, Figure 40 provides a more visual representation of this  $\Pi$ , where the continuity of the periodic jet was disturbed by the extreme collapse around the throat.



**Figure 39.** Velocity profiles during one cycle of self-excited oscillation at  $\Delta P = 94.3$  mmHg and  $\Pi = -39$  case.



**Figure 40.** Periodic but discontinued jet through the collapsed tube during one cycle of self-excited oscillation at  $\Delta P = 94.3$  mmHg and  $\Pi = -39$  case.

### 3.5.2. Asymmetrical Downstream Jet

Thus far, it was thought that the periodic downstream jet might exhibit symmetry around the central horizontal axis of the tube. However, it has been discovered that the jets emerging downstream from the tube throat are not symmetrical. For examining this phenomenon during

self-excited oscillation, the velocity data have been extracted one more time at  $x = 145$  mm right after the throat area, and the y-axis is normalized by  $a'$ , where  $a'$  is the width of flow channel on the measured plane.

From Figure 41 to Figure 44, it is clearly evident that instantaneous peak velocity was fluctuating from the positive half to the negative half of the  $y/a'$ . A dashed line around  $y/a' = 0$  was introduced on velocity profiles to distinguish the movement.

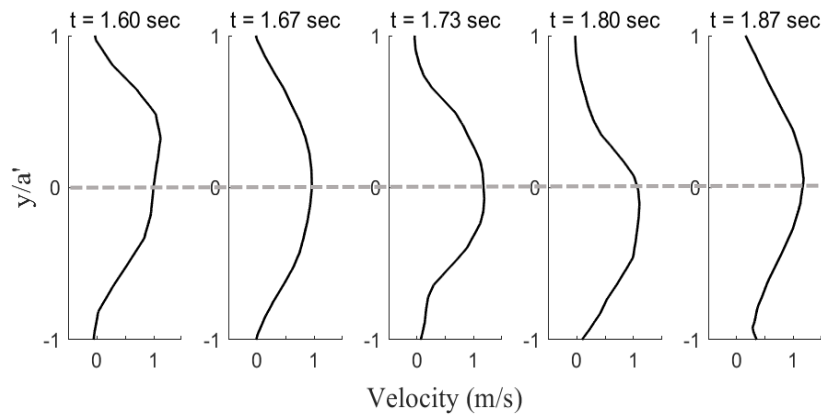


**Figure 41.** Velocity profile from  $t = 1.60$  sec to  $1.87$  sec at  $\Delta P = 94.3$  mmHg and  $\Pi = -30$  during the third cycle of self-excited oscillation.

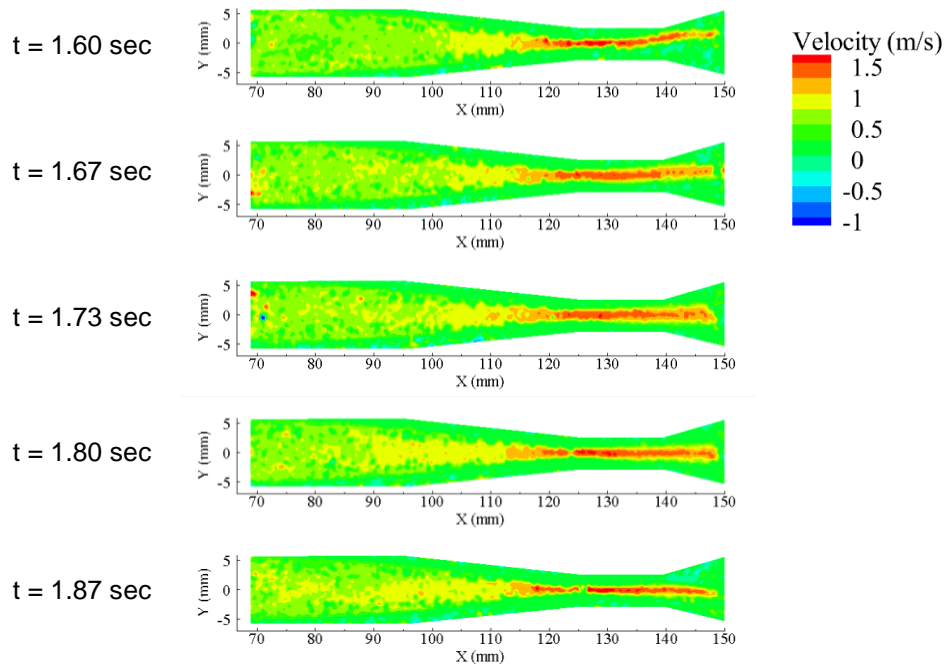


**Figure 42.** An asymmetrical downstream jet (upward) was observed at  $t = 1.60$  sec at  $\Delta P = 94.3$  mmHg and  $\Pi = -30$  during the third cycle of self-excited oscillation.

In the velocity profile illustrated in Figure 41, it is evident that the peak velocity during the third cycle at 1.60 seconds exceeded the level indicated by the dashed line, returning to center around the dashed line at 1.87 seconds. This observation is further supported by Figure 42, which portrays an asymmetrical downstream jet at  $t = 1.60$  seconds. Notably, this pattern varied across the self-exciting oscillation cycles. Upon nearing the next cycle, specifically the fourth one depicted in Figure 43, the peak velocity was observed below the dashed line at 2.33 seconds. The downstream jet scenario is apparent in subsequent demonstrations shown in Figure 44.

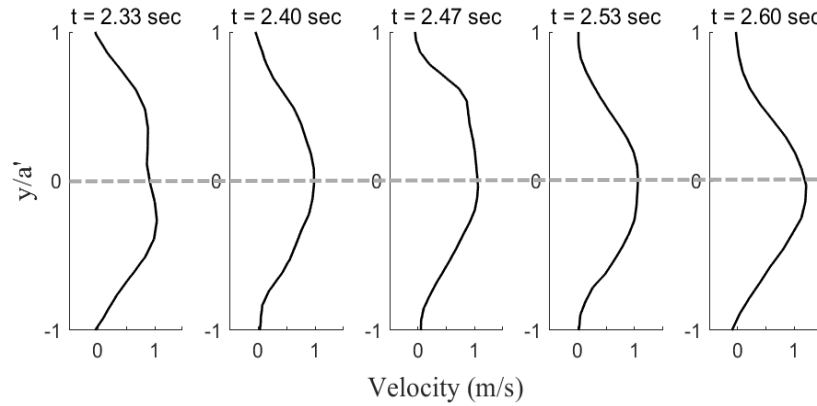


**Figure 43.** Velocity profile from  $t = 2.33$  sec to 2.60 sec at  $\Delta P = 94.3$  mmHg,  $\Pi = -30$  during the fourth cycle of self-excited oscillation.

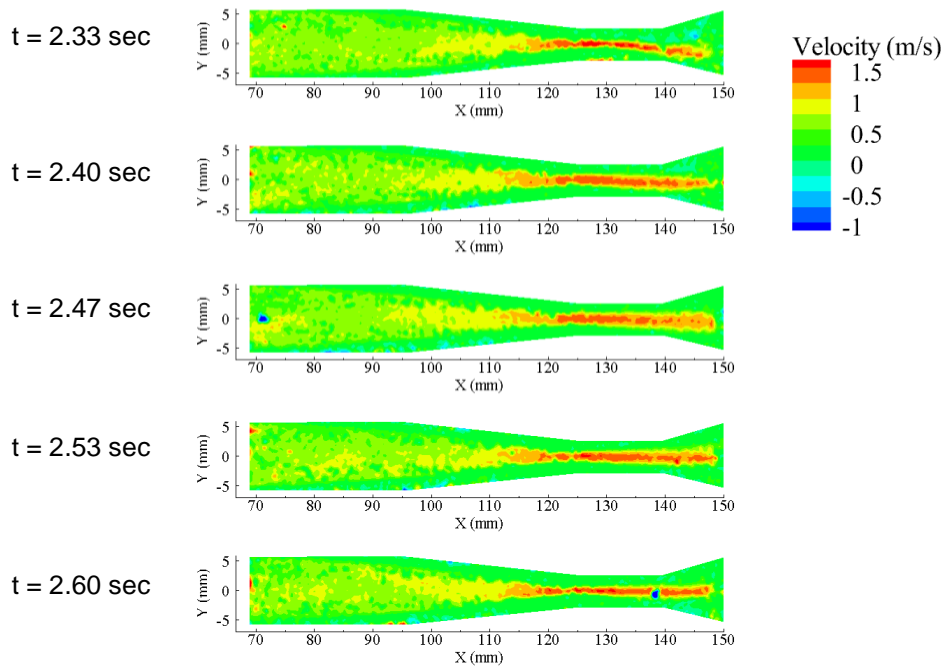


**Figure 44.** An asymmetrical downstream jet (downward) was observed at  $t = 2.33$  sec at  $\Delta P = 94.3$  mmHg and  $\Pi = -30$  during the fourth cycle of self-excited oscillation.

### 3.6. Summary

This study examined the behavior of a collapsible tube under varying steady flow inputs. Results showed that decreasing transmural pressure led to tube deformation from a circle to an ellipse, then to a dumbbell shape, ultimately collapsing and touching walls. Under steady flow,

negative transmural pressure caused the collapse, with the collapse degree depending on pressure ( $\Pi$ ) for each  $\Delta P$ . Self-excited oscillations began at  $\Delta P = 60.7$  mmHg, stemming from the interplay between tube elasticity and fluid dynamics, with the frequency escalating as both the pressure differential and negative  $\Pi$  increased. Self-excited oscillations' onset occurred at  $\Pi = -20$  to  $-25$  for most of the cases and stopped at more negative  $\Pi$  as the pressure differential increased. Flow velocity fluctuated during self-excited oscillations, spiking to  $1.2$  m/s before dropping to critical velocity ( $0.3$  m/s), then to  $0.13$  m/s before collapse. Frequencies ranged from  $1.3$  Hz to  $2.5$  Hz as  $\Delta P$  increased from  $87.7$  mmHg to  $98.0$  mmHg. At every  $\Delta P$  case, the frequency increased with more negative  $\Pi$  and peaked before the tube collapsed. Flow rate decreased in all lower  $\Delta P$  cases with increases in negative transmural pressure. But self-excited oscillatory cases maintained a relatively larger average flow rate, even under most negative  $\Pi$  conditions. Moreover, asymmetrical downstream jets were spotted during self-excited oscillations, indicating asymmetrical vortex shedding is related to self-excited oscillations.

## 4. COLLAPSIBLE TUBE UNDER PULSATILE FLOW

### 4.1. Introduction

To explore the interaction between fluid and structure amidst physiologically pulsatile conditions, we performed experiments using the identical collapsible tube configuration to steady flow experiment. In this test, the constant flow pump was substituted with a programmable pulsatile pump, as shown in Figure 15 in Chapter 2. Figure 45 depicts the normalized pressure waveform of two characteristic cycles produced by the pump. Within each cycle, the forward piston motion accounted for 35% of the time, while the backward piston motion comprised 65%, mimicking a typical systolic duration of 35% in the human cardiac cycle [49]. A very brief dip into negative pressure can be observed during 35%-45% of the cycle in Figure 45, which is caused by the closure event of the ball valve, representing typical heart valve functions.

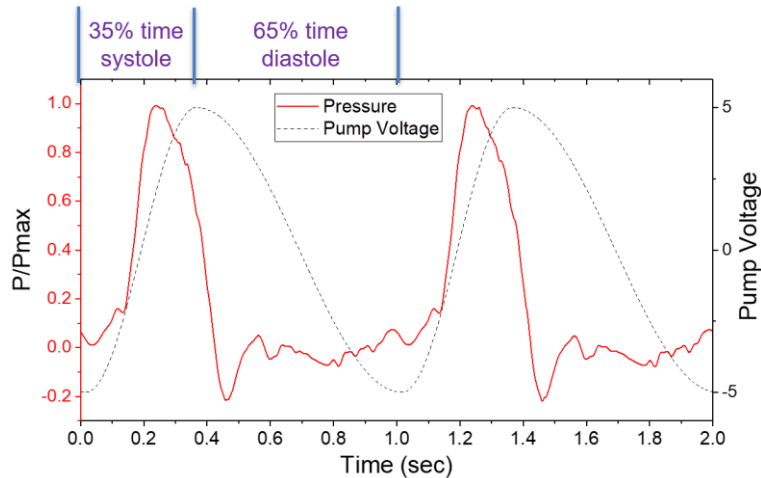


**Figure 45.** Pressure and pump activation waveforms.

To examine the impact of both pulsation amplitude and frequency of flow two dimensionless parameters were considered: Reynolds number ( $Re$ ) and Womersley number ( $Wo$ ). To investigate the dynamics of biological fluid flow under a variety of physiological conditions,  $Re$  and  $Wo$  numbers prove to be highly effective [50]. Here, the  $Re$  number is defined as:

$$Re = \frac{4Q_m}{\pi D \nu} \quad (19)$$

where  $Q_m$  is the mean flow rate during each cycle;  $D$  is the diameter of the tube;  $\nu$  is the kinematic viscosity of the fluid mixture. The Womersley,  $Wo$ , quantifying the normalized frequency of the pulsatile flow [51], is defined as:

$$Wo = \frac{D}{2} \sqrt{\frac{\omega}{\nu}} \quad (20)$$

where  $\omega = 2\pi f$  is the angular frequency of the pulsation. Lei et al. (1997) mentioned some typical range of  $Re$  during input of resting flow in venous grafting as in Figure 46, frequency was considered 60 bpm [52]. In our study, the range of these nondimensional parameters was inspired primarily by flow characteristics in larger veins and other comparable physiological transportation conditions in collapsible vessels [49], [53], [54], [55], [56]. The range of  $Re$  and  $Wo$  will be provided in the next section of this chapter.

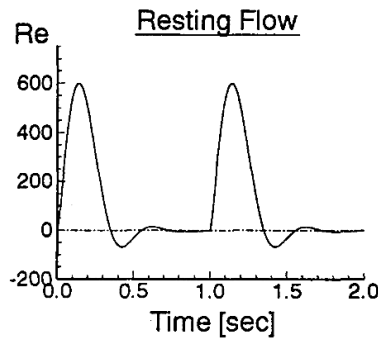


**Figure 46.** Reynolds number of venous flow input mimicking rest condition [52].

#### 4.2. Test Procedure and Conditions

To compare the effect of pulsation in the same collapsible tube model, a different flow loop was introduced comprising a programmable pulsating pump. This pump delivered the desired inlet flow to the collapsible tube model inside the pressurized chamber with a preset flow



rate and frequency. An ultrasonic flow meter was installed downstream of the tube to monitor both of peak and average flow rates.

The amplitude of fluctuations in the axial cross-section area was also determined from the captured images for each case. To facilitate this area measurement and perform comparison, another nondimensional parameter ( $\beta$ ) was defined. This dimensionless axial cross-sectional area can be defined by Equation 21.

$$\beta = \frac{\Omega}{\Omega_0} \quad (21)$$

where  $\Omega$  is the axial cross-sectional area of collapsible tube at any condition.  $\Omega_0$  is the axial cross-section area without external pressure on the pressurized chamber and at no flow condition. Pressure data were taken in a similar way to the steady flow experiment and pressure inside the chamber was controlled by a syringe pump in the same way as the steady flow test. It's to be noted that the reported  $\Pi$  in this section as well as in the following sections will be the mean value of downstream transmural pressure of any corresponding cycle of a case during the test. This mean value of  $\Pi$  was recorded directly from a computer display connected to the pressure transducers.

Based on the available works of literature as discussed in the previous section of this chapter, the average flow rate was decided to be set to 0.75 & 1.5 liters per minute (Lpm) and frequency was set to 30 and 60 beats per minute (bpm). We conducted three cases from the combination of the mentioned ranges of mean flow rate and frequency as tabulated in Table 4. The baseline case was representing the base flow rate of 1.5 Lpm with a frequency of 60 bpm.  $Re$  and  $Wo$  numbers represent the mean flow rate and frequency of the cases correspondingly. The three test cases, all fall in the range of large venous flows and other similar physiological transport phenomena in collapsible tubes as discussed in the previous section.

**Table 4.** Pulsatile flow cases

Case	Re	Wo	Range of mean $\Pi$
1 (Baseline)	655	10.4	+52.2 to -48.9
2 (Half amplitude)	327	10.4	+48.7 to -48.9
3 (Half frequency)	655	7.4	+50.8 to -48.9

### 4.3. Fluid-Structure Interactions under Pulsatile Flow Condition

#### 4.3.1. Effect of Transmural Pressure on Pulsatile Flow

##### 4.3.1.1. *Highly positive transmural pressure*

Beginning with the baseline scenario at Reynolds number (Re) of 655 and Womersley number (Wo) of 10.4, under conditions where the downstream transmural pressure was highly positive ( $\Pi = 52.2$ ), the collapsible tube exhibited forward flow towards the downstream during systolic elevation. Analysis of Figure 47 confirms a positive pressure gradient during this period. As depicted in Figure 48, which illustrates an almost flat line with small amplitude fluctuations of area across two cycles. No significant deformation was observed in the collapsible tube. Some raw images of this condition at different times of a cycle have been provided in Figure A2 in Appendix. Figure 49 shows the phase-averaged velocity fields in this condition. It is clear that the pulsatile flow passes the undeformed tube with the highest peak systolic velocity at  $t=0.2$  seconds, and a brief reverse flow phase was observed from 0.4 to 0.6 seconds which corresponded well to the pressure measurements.

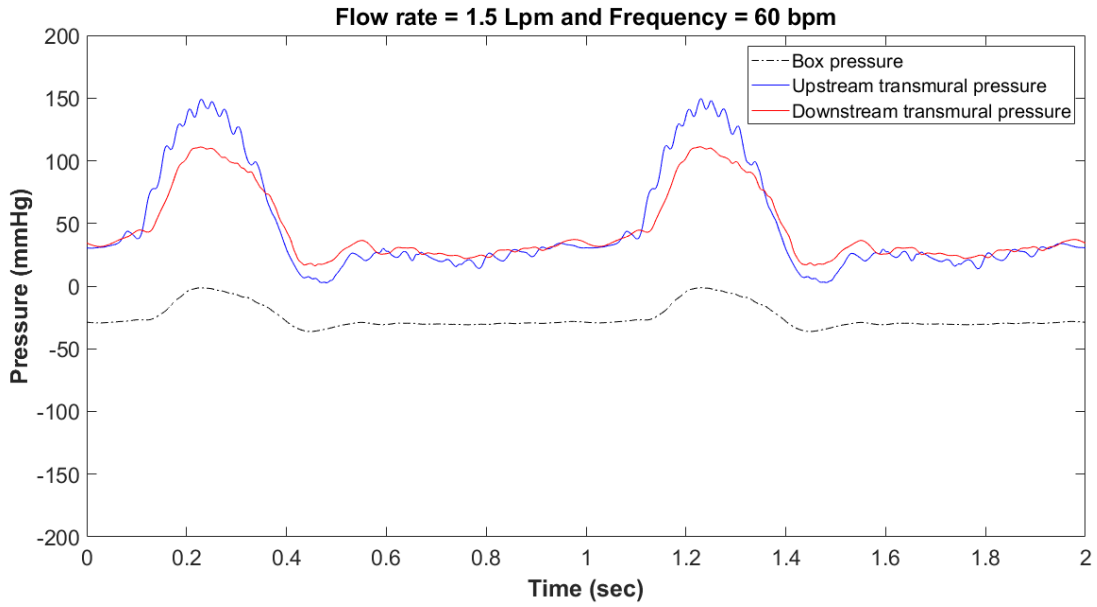


**Figure 47.** Pressure vs. time for baseline case ( $Re = 655$ ,  $Wo = 10.4$ ) at mean downstream  $\Pi = +52.2$ . The dotted line represents the chamber pressure at those cycles.

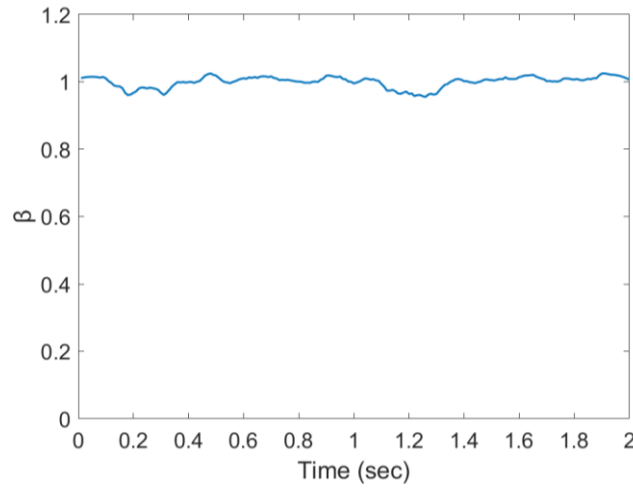


**Figure 48.** Area vs. time for baseline case ( $Re = 655$ ,  $Wo = 10.4$ ) at mean downstream  $\Pi = +52.2$ .

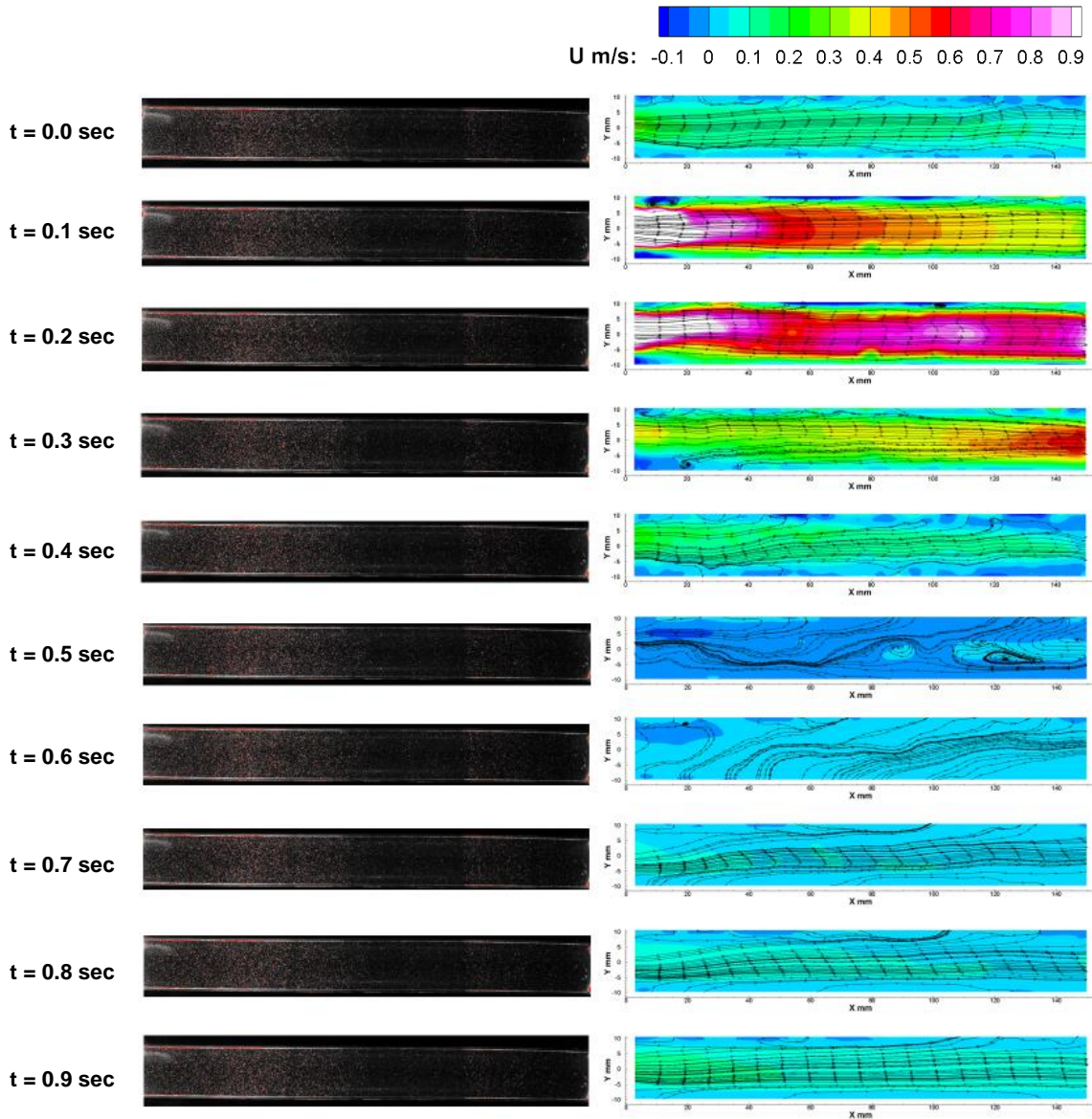


**Figure 49.** PIV results for baseline case ( $Re = 655$ ,  $Wo = 10.4$ ) at highly positive mean downstream  $\Pi = +52.2$ . Left column shows the raw images and right column shows the flow field with streamlines.

Instantaneous velocity fields at  $t=0.1$  and  $0.2$  seconds were compared in multiple pulsating cycles in Figure 50. It is clear that while the accelerating flow exhibited uniformity and a laminar pattern across the cycles, an unstable and wavy flow pattern was observed at peak and post-peak systolic flow from cycle to cycle. Such flow characteristics suggest the presence of 3D vortex structures during the deceleration phases of pulsatile flow.

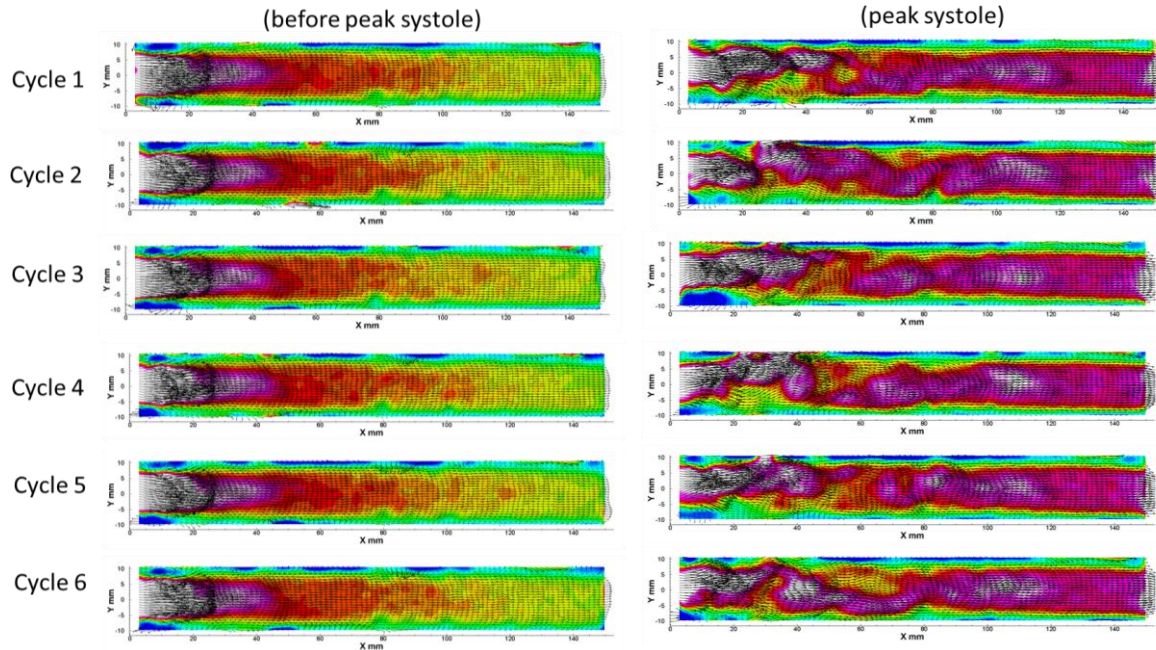


**Figure 50.** Instantaneous velocity before the peak systole at  $t = 0.1$  sec (left column) and peak systole  $t = 0.2$  sec (right column) for baseline case at  $\Pi = +52.2$  (highly positive).

#### 4.3.1.2. Near neutral (slightly positive) transmural pressure

In Figure 51, it is illustrated that when the downstream transmural pressure ( $\Pi$ ) was decreased to 6.9 (slightly positive) at the beginning of systole, the pressure gradient nearly approached zero. At this point, the tube exhibited partial collapse at its midpoint and buckled symmetrically. The amplitude of fluctuation in the area throughout the cycles for these structural changes in the collapsible tube has been demonstrated in Figure 52. Once a positive pressure gradient was established, flow pushed through the deformed tube during the accelerating phases. This flow also pushed the throat area towards the downstream at  $t = 0.1$  sec as depicted in Figure 53. Importantly, no significant reverse flow was observed in this scenario, even when a mild negative pressure gradient was present during the diastolic piston movement.

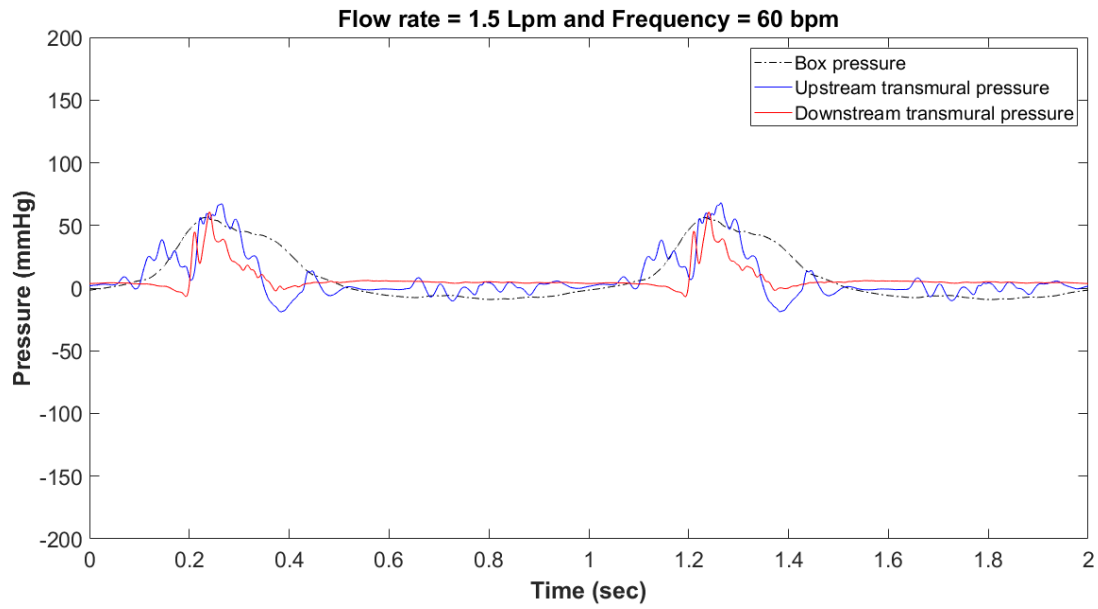


**Figure 51.** Pressure vs. time for baseline case ( $Re = 655$ ,  $Wo = 10.4$ ) at mean downstream  $\Pi = +6.9$ . The dotted line represents the chamber pressure at those cycles.

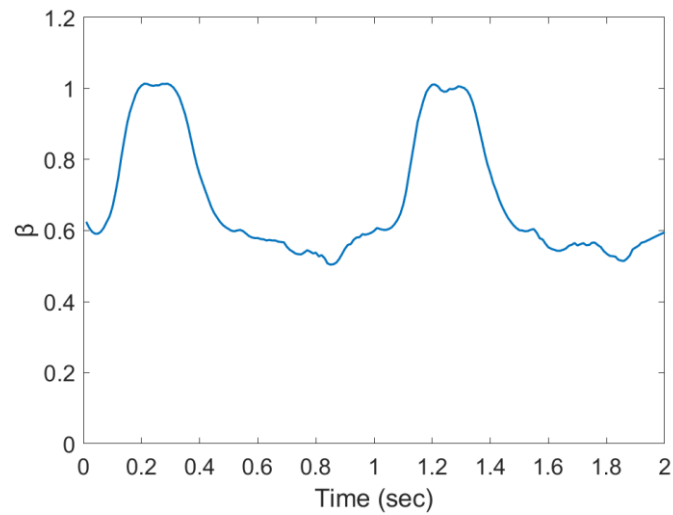


**Figure 52.** Area vs. time for baseline case ( $Re = 655$ ,  $Wo = 10.4$ ) at mean downstream  $\Pi = +6.9$ . Fluctuation in the area amplitude has been observed.



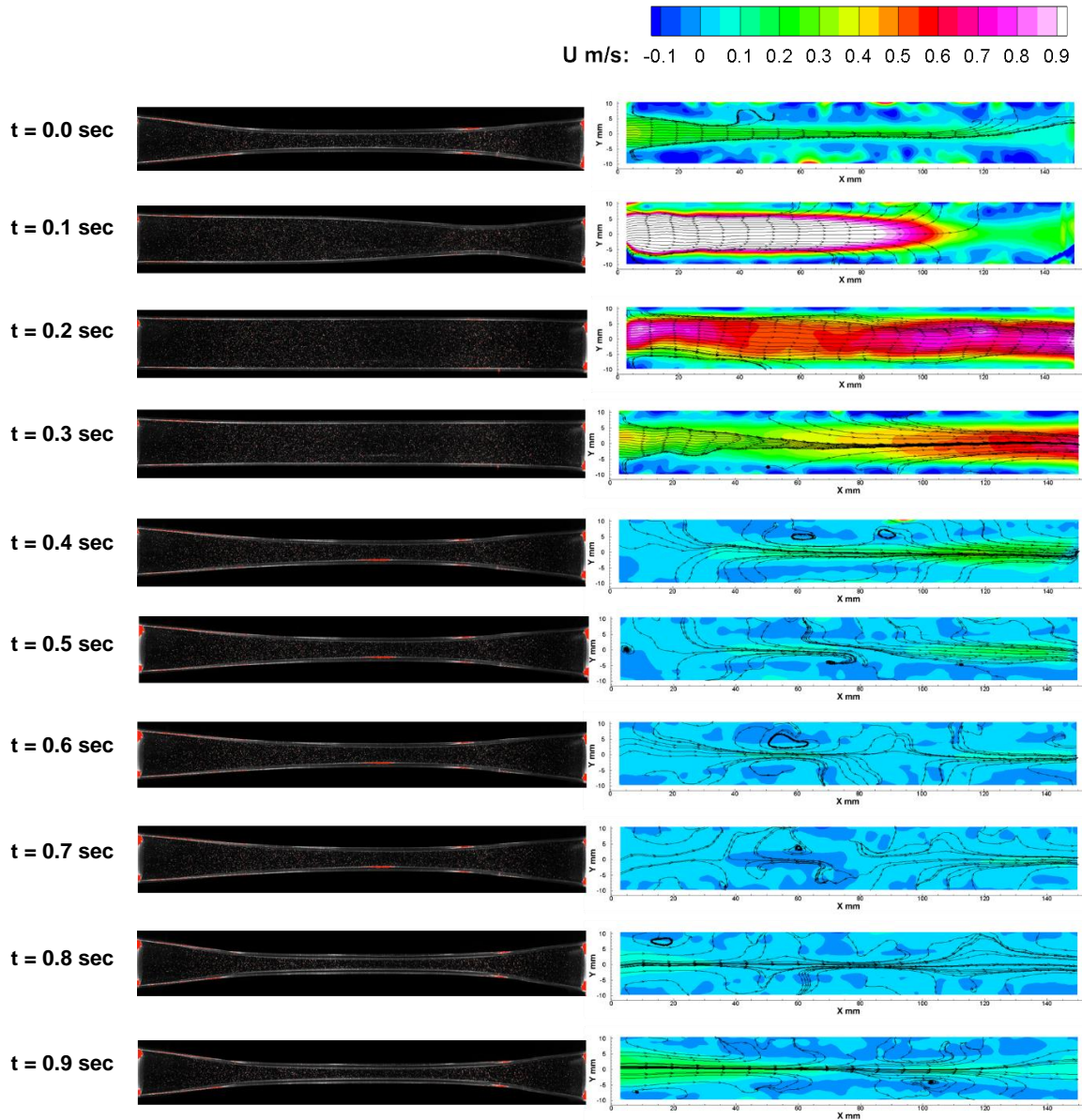


**Figure 53.** PIV results for baseline case ( $Re = 655$ ,  $Wo = 10.4$ ) at slightly positive mean downstream  $\Pi = +6.9$ . Left column shows the raw images and right column shows the flow field with streamlines.

#### 4.3.1.3. *Highly negative transmural pressure*

When the mean downstream transmural pressure reached highly negative values ( $\Pi = -36.4$ ), the tube collapsed completely, touching the opposite walls, and remained collapsed throughout the diastole. However, as soon as systolic flow commenced, it exerted pressure, causing the collapsed tube to reopen just before reaching peak systolic flow. Particularly

intriguing was the observation of a unique deformation of the tube at peak systolic flow, occurring at  $t = 0.2$  sec, as depicted in Figure 54. This "Double Throat" deformation led to flow acceleration followed by deceleration before reaching the maximum collapse region downstream.

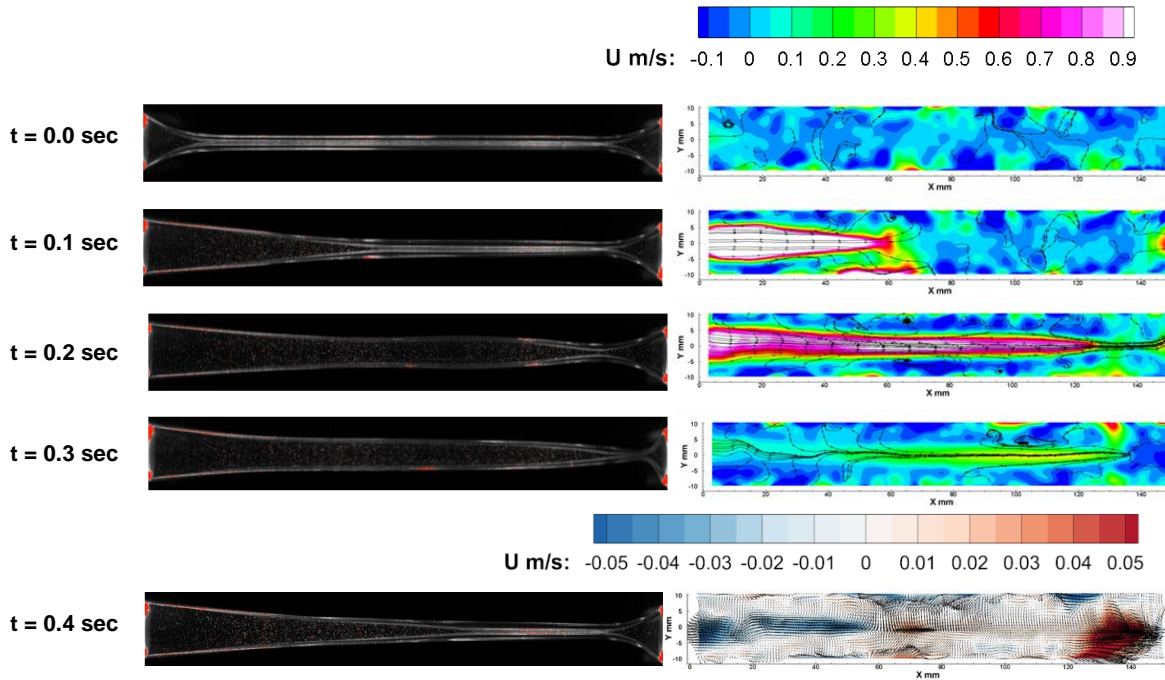


**Figure 54.** PIV results for baseline case ( $Re = 655$ ,  $Wo = 10.4$ ) at highly negative mean downstream  $\Pi = -36.4$ . Left column shows the raw images and right column shows the flow field with streamlines. At  $t = 0.4$  sec, flow reversal was observed with a different color bar.

Once the flow returns to the diastolic phase, the tube collapses again, predominantly expelling the fluid. Consequently, we continue to witness fluctuations in the axial cross-sectional area, as depicted in Figure 55. The magnitude of the area change was diminished (ranging between  $\beta = 0.3$  to  $0.6$ ) compared to the slightly negative  $\Pi$  condition (ranging between  $\beta = 0.6$  to  $1.0$ ).

Another interesting phenomenon was noted shortly after the peak systole, at approximately  $t = 0.4$  sec. A self-excited oscillation occurred near the exit, as illustrated in Figure 56 of the downstream transmural pressure plot. This spontaneous self-excited oscillation



burst triggered local reverse flow upstream of the collapsible tube. PIV results from the previously mentioned Figure 54 validate this flow reversal at  $t = 0.4$  sec, but the magnitude of this reverse flow was smaller compared to the systole flow.

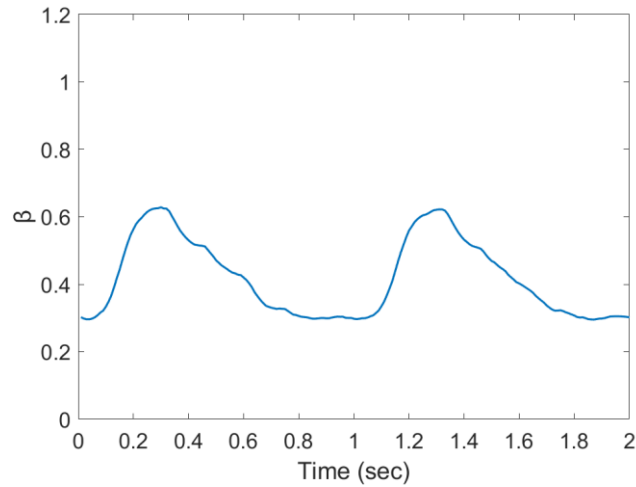


**Figure 55.** Area vs. time for baseline case ( $Re = 655$ ,  $Wo = 10.4$ ) at highly negative mean downstream  $\Pi = -36.4$ . Fluctuation in area amplitude has been observed, amplitude went down.

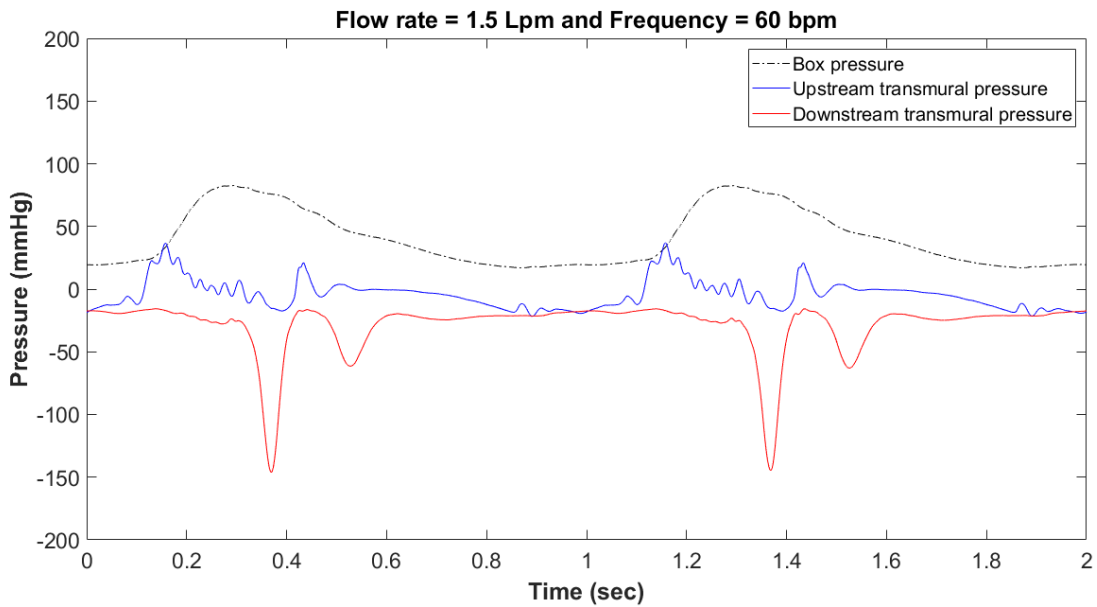


**Figure 56.** Pressure vs. time for baseline case ( $Re = 655$ ,  $Wo = 10.4$ ) at mean downstream  $\Pi = -36.4$ . Self-excited oscillation triggered in the collapsible tube downstream.

We explored deeper into negative downstream transmural pressure and discovered that a more negative  $\Pi$  triggers earlier and more prolonged self-excited oscillations in the collapsed tube downstream. Figure 57 clearly illustrates that as  $\Pi$  approached -48.9, each cycle of the pulsatile flow exhibited the onset of triple peaks and prolonged self-excited oscillations. However, the amplitude of these self-excited oscillations was lower compared to other  $\Pi$  cases.

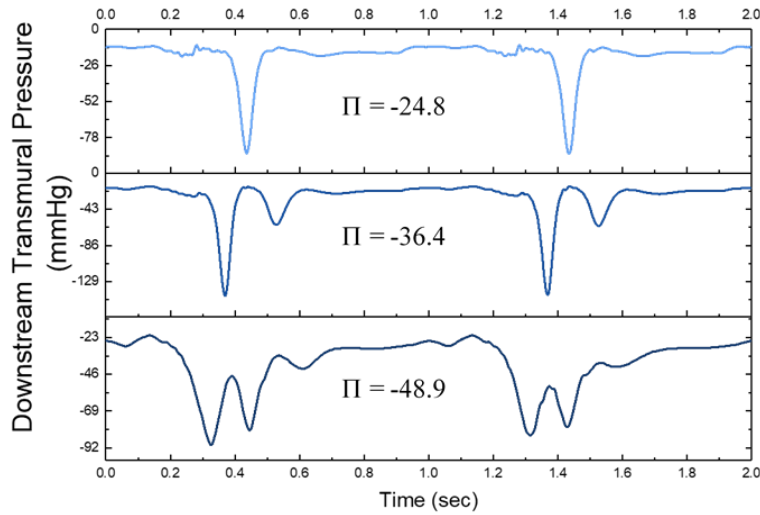


**Figure 57.** Earlier and prolonged self-excited oscillation triggered at baseline case ( $Re = 655$ ,  $Wo = 10.4$ ) under  $\Pi = -48.9$ .

#### 4.3.2. Effect of Reduced Reynolds and Womersley Numbers on Pulsatile Flow

To understand the effect of altered Reynolds and Womersley numbers in pulsatile flow, we have done a half Reynolds number and a half frequency case in contrast to the baseline case.

##### 4.3.2.1. Reduced Reynolds number

When the flow rate was reduced to half from the baseline (1.5 Lpm), the average  $Re$  number dropped to 327. At this condition under similar slightly positive mean downstream transmural pressure, the tube still went through deformation by buckling symmetrically. However, this reduced  $Re$  case showed less deformation compared to the baseline case. From

Figure 58 it can be described that during the fluctuation of the axial cross-sectional area, the amplitude of this change was smaller in half Re number case.

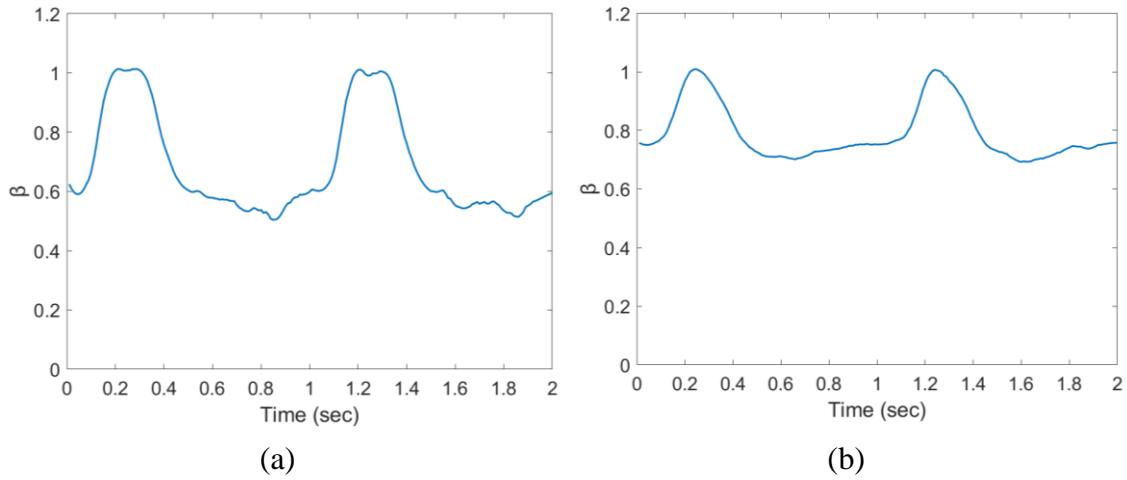


**Figure 58.** Area vs. time: (a) Baseline case ( $Re = 655$ ,  $Wo = 10.4$ ) at  $\Pi = +6.9$ ; (b) Half Re case ( $Re = 327$ ,  $Wo = 10.4$ ) at  $\Pi = +6.3$ .

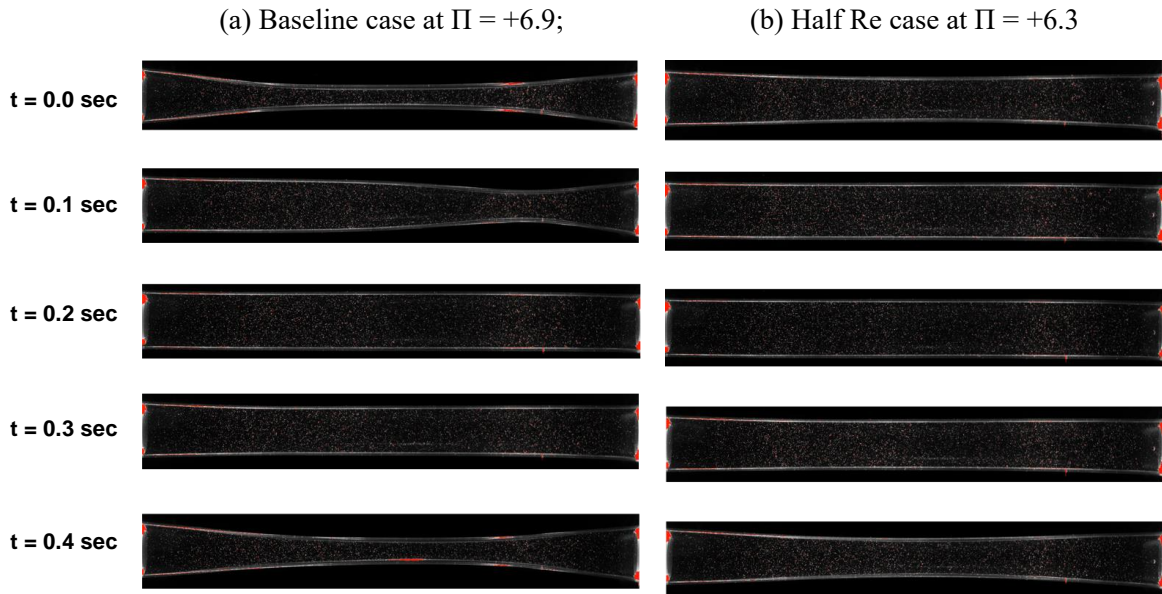


**Figure 59.** PIV raw images of the axial cross-sectional area under baseline and altered Re case at similar slightly positive  $\Pi$ .

From raw PIV images in Figure 59, a notable difference was observed at  $t = 0.1$  sec, when systolic flow passed through the buckled tube. The collapsible tube bounced back to undeformed shape more rapidly at reduced Re. Figure 60 illustrates the velocity map obtained

from PIV, corresponding well with the already described results from raw images and area calculation. Other than that, despite the lower velocity magnitude, a wavy upstream jet was observed at reduced Re case at  $t = 0.2$  sec.

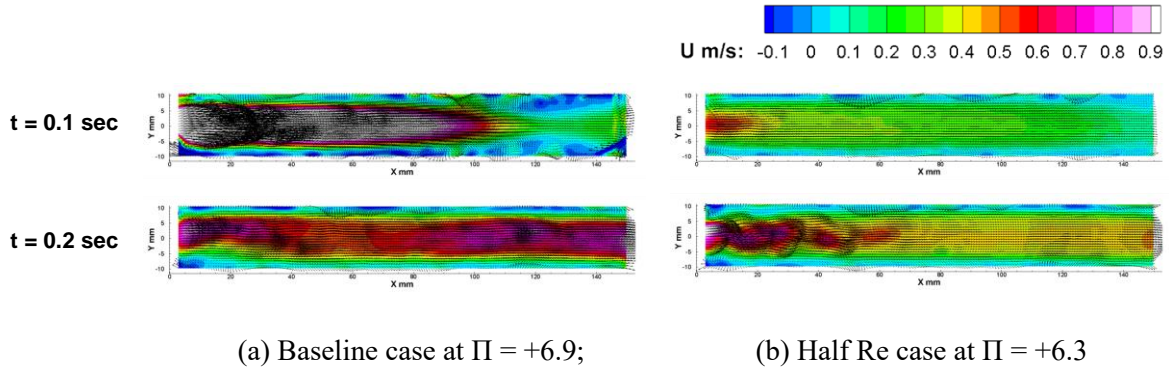


**Figure 60.** Velocity map utilizing PIV results under baseline and altered Re case at similar slightly positive  $\Pi$ .

#### 4.3.2.2. *Reduced Womersley number*

In a second comparison, the frequency of pulsatile flow was reduced to half (reduced  $Wo$  number), doubling the cycle periods and overall flow volume each cycle. To achieve a phase-to-phase comparison with the baseline case, phase-dependent dimensionless time ( $t/T$ ) was introduced here, where  $t/T$  is defined as the ratio of the actual flow time to the cycle period. At this condition, under similar mean downstream transmural pressure, no significant change in the tube deformation condition was observed. Figure 61 describes this unchanged amplitude of varying axial cross-sectional area. However, to recover the undeformed shape, the reduced frequency case took a different approach at the same phase. In this scenario, the tube's wall deformation wave was comparatively faster than the flow speed. Therefore, as shown in Figure 62(b), at  $t/T = 0.1$ , the tube wall started to bounce back quickly to the undeformed shape, while flow was still accelerating towards the downstream at peak systole.

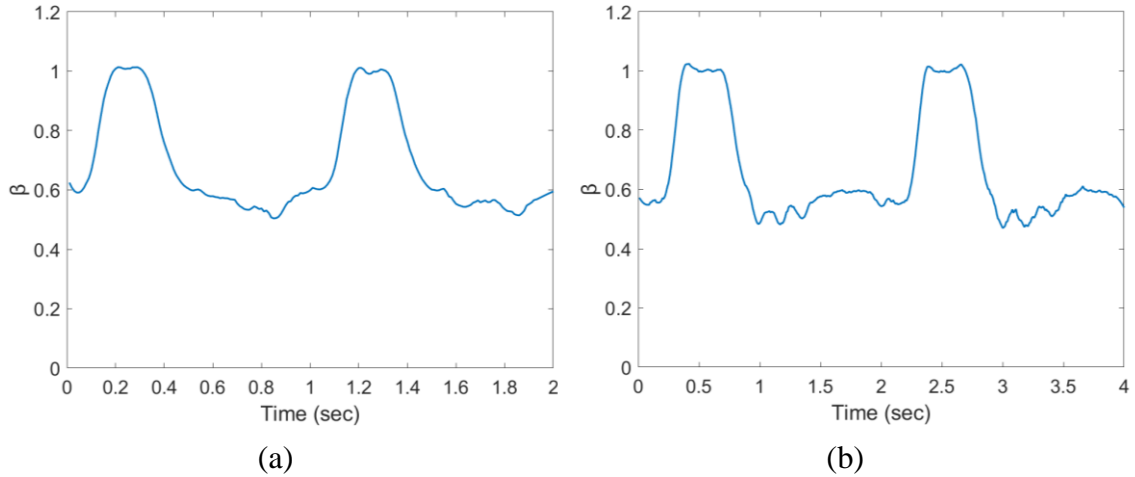


**Figure 61.** Area vs. time: (a) Baseline case ( $Re = 655$ ,  $Wo = 10.4$ ) at  $\Pi = +6.9$ ; (b) Half frequency case ( $Re = 655$ ,  $Wo = 7.4$ ) at  $\Pi = +6.3$ .

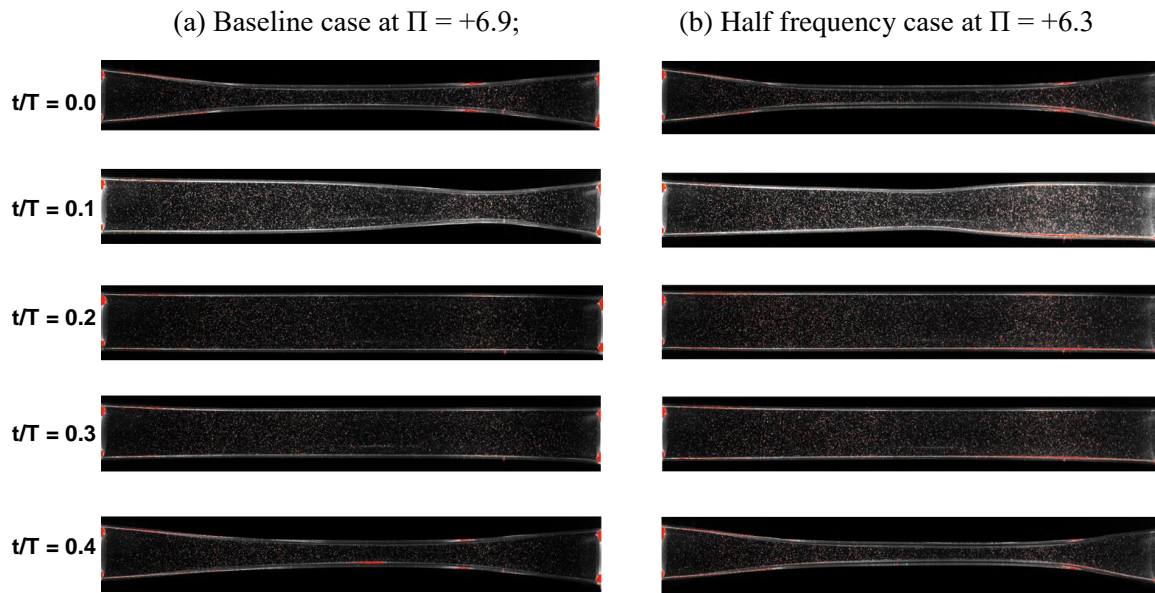


**Figure 62.** PIV raw images of the axial cross-sectional area under baseline and altered  $Wo$  case at similar slightly positive  $\Pi$ .

The velocity map in Figure 63, obtained from the PIV results under baseline and altered frequency conditions didn't produce any significant distinction in the flow fields. However, the velocity magnitudes over the regions in the reduced frequency case were not the same as in the baseline case.

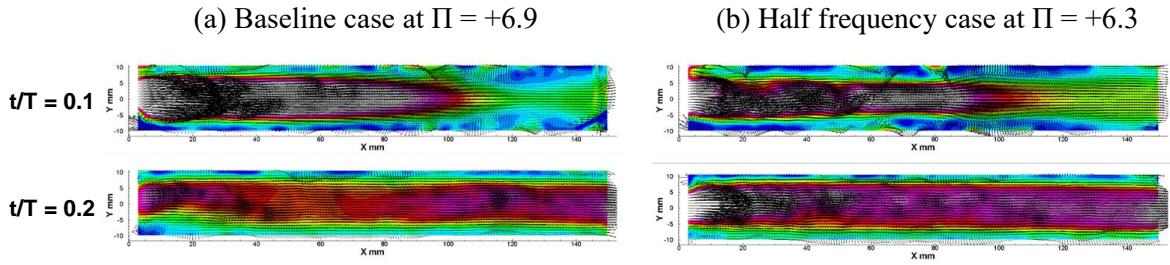


**Figure 63.** Velocity map utilizing PIV results under baseline and altered  $Wo$  case at similar slightly positive  $\Pi$ .

#### 4.3.2.3. Existence of self-excited oscillation under reduced $Re$ and $Wo$ numbers

Highly negative transmural pressure is always susceptible to triggering the self-excited oscillation, even during pulsatile flow conditions. Under reduced  $Re$  and  $Wo$  numbers, highly negative  $\Pi$  was applied to the collapsible tube similar to the baseline case ( $\Pi = -48.9$ ). Figure 64 shows that under reduced frequency, the onset of self-excited oscillation became even more evident and strong during the pulsating cycle due to the prolonged pulsating period. With pulsatile flow frequency getting smaller, we can expect the flow to become increasingly quasi-steady and the self-excited oscillation approaches what we observed in the steady flow input cases. In the reduced  $Re$  case, however, the tube didn't exhibit any significant self-excited oscillation in the downstream pressure due to the reduced flow velocity.

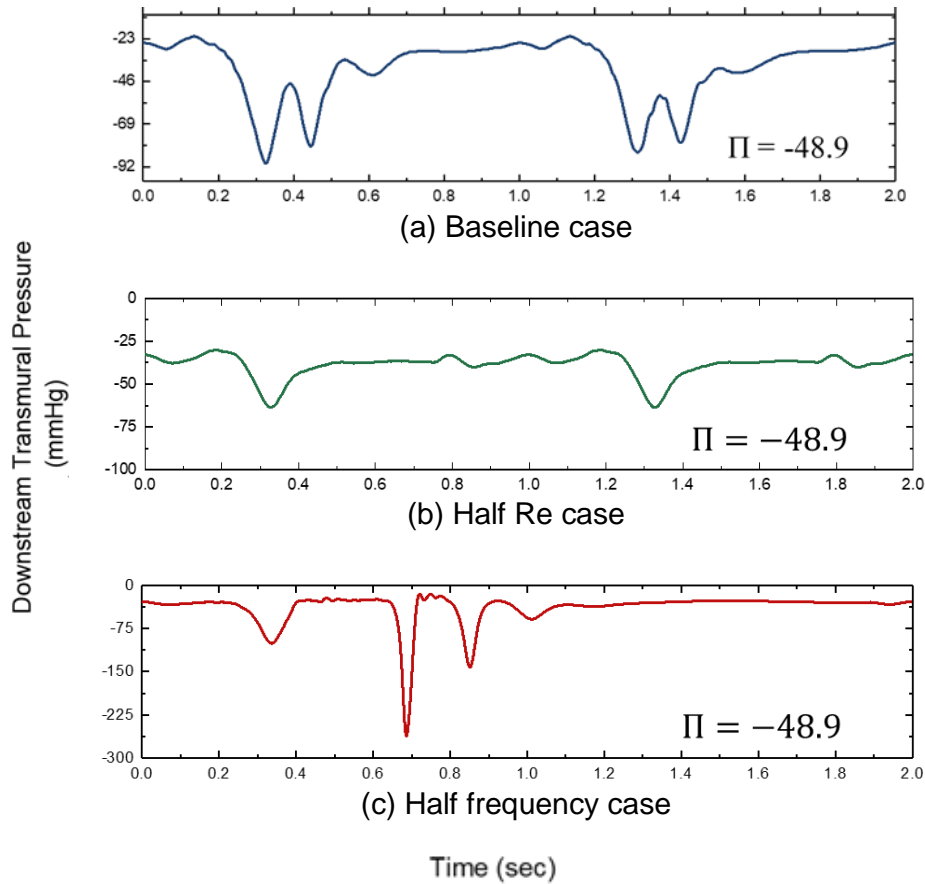
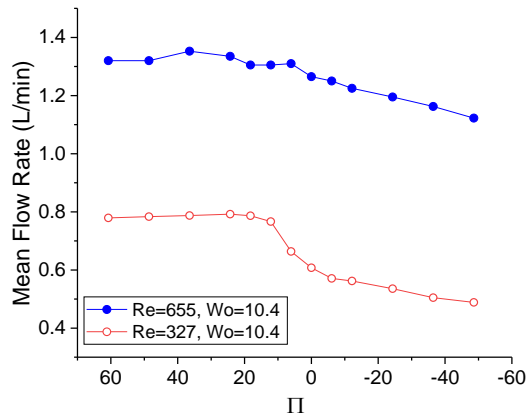


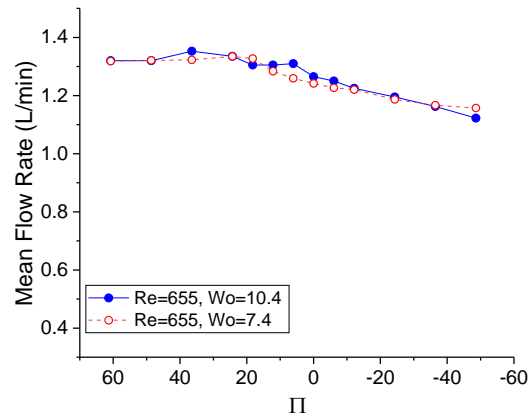
**Figure 64.** Comparison of self-excited oscillation burst under highly negative mean downstream transmural pressure. Half Re case didn't trigger self-excited oscillation.

#### 4.3.3. Flow Limitation Effect in Pulsatile Flow

In Figure 65, a comparison is presented illustrating mean flow rates of the pulsatile flow relative to  $\Pi$ , considering reduced Re and  $Wo$ . Across all instances in Figure 65(a), a pronounced constraint on flow was evident when the average  $\Pi$  dropped below +10. Though the mean flow rate was independent of change in downstream transmural pressure until that range of  $\Pi$ , the flow limitation phenomenon became more prominent at a reduced Re of 327. Notably, the observed pattern of limiting mean flow rate remained consistent across different  $Wo$  values as illustrated in Figure 65(b), indicating that the frequency of pulsatile flow has minimal influence on the overall mean output flow in collapsible tubes.



(a) Reduced Re



(b) Reduced Wo

**Figure 65.** Mean flow rates under pulsatile flow with different Re and Wo numbers: (a) Reducing Re by half; (b) Reducing frequency by half.

Figure 66 demonstrates how the peak flow rate changes with  $\Pi$  for reduced Re and Wo numbers. Though the limitation in mean flow rates occurred with a very small slope, peak flow rates decreased more significantly because of flow limitations. It's to be noted that when  $\Pi$  was below -20, the brief self-excited oscillations actually led to a higher peak flow rate as  $\Pi$  decreased. This effect from self-excited oscillations was more noticeable when Wo was reduced, as the longer pulsatile flow period gave more time for the self-excited oscillation to happen during flow deceleration.



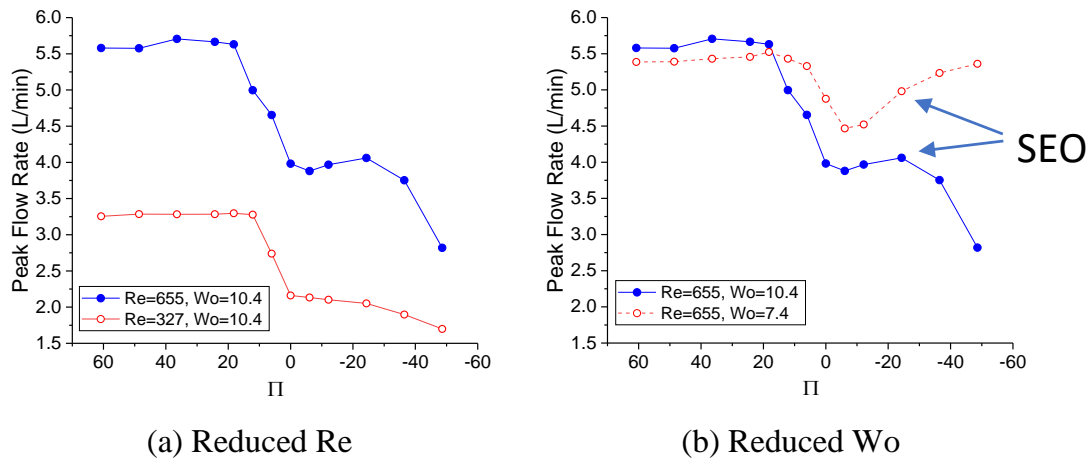


**Figure 66.** Peak flow rates under pulsatile flow with different Re and Wo numbers: (a) Reducing Re by half; (b) Reducing Wo by half.

Note: SEO means self-excited oscillation instances on the plot of peak flow rate curves for reduced Wo number case.

#### 4.4. Summary

In this chapter, the effects of altered transmural pressure, Reynolds number, and Womersley number on pulsatile flow through a collapsible tube have been discussed. Firstly, the transition from highly positive transmural pressure to highly negative significantly impacts the dynamics of cyclic tube deformation. During testing, the baseline case at  $\Pi = -36.4$  resulted in a unique "double throat" condition where the tube deformed, leading to accelerated flow followed by rapid deceleration and eventual collapse downstream. Self-excited oscillation was triggered under highly negative  $\Pi$  conditions during each cycle of the pulsatile flow.

In addition to the altered  $\Pi$ , Reynolds number and pulsatile flow frequency were reduced to half. Results suggest that, during half Reynolds number condition under the same  $\Pi$  (near neutral), the collapsible tube deformed less than the baseline condition. Though half-frequency case under the same  $\Pi$  (near neutral) showed similar tube deformation, they exhibited different responses in the context of traveling waves. In this particular scenario, the collapsible tube's wall

deformation wave traveled faster than the flow, which resulted in a more rapid bounce back of the wall to the undeformed shape.

The flow rate was independent of  $\Pi$  until it dropped to +10, but mean flow rate limitation has been observed under negative transmural pressure with a gradual decrease. In contrast, the peak flow rate dropped very sharply in the range of  $0 < \Pi < +10$ , which was elevated again during self-excited oscillation under highly negative  $\Pi$ .

## 5. CONCLUSIONS

### 5.1. Concluding Remarks

In this thesis, an experimental investigation has been done to observe the fluid-structure interaction of a collapsible tube under both steady and pulsatile flow conditions. Quantitative analysis of structural deformation through optical measurement and flow field analysis using Particle Image Velocimetry (PIV) has been performed. This study also covers a broader range of Reynolds numbers and transmural pressure to examine how the collapsible tube deforms and triggers the self-excited oscillation under altered conditions of steady flow. The experiment validated the static deformation of the tube against the classic tube law. Deformation and self-excited oscillation under steady flow were carried out across a range of pressure differentials ( $\Delta P$ ) through the collapsible tube and transmural pressures ( $\Pi$ ). In addition to the steady flow condition, the collapsible tube was introduced to the pulsatile flow input during the next phase of this experimental study. Considering the scarcity of available experimental data to explain collapsible tube behavior under varying pulsatile flow conditions, this segment of the experiment can address the gaps in understanding. Reynolds number and flow frequency were two major factors during the pulsatile flow experiment to compare the fluid-structure interaction under different conditions. Moreover, PIV enabled us to examine the variations in the flow field under both steady and pulsatile flow conditions including changes in velocity, symmetry of the jet, direction of flow, etc.

In the first part of the results, the static deformation of a collapsible tube to validate its behavior against the classic Shapiro's tube law under varied transmural pressures. During no-flow conditions, the deformation of the tube was examined by changing the transmural pressure from positive to negative values. After the validation of the collapsible tube's behavior, we

examined the tube deformation trend across a range of pressure differences ( $\Delta P$ ) and transmural pressures ( $\Pi$ ). Furthermore, a critical range of negative transmural pressure has been identified, which triggers the self-excited oscillation upon reaching a minimum  $\Delta P$ . The key findings of the collapsible tube under steady flow can be summarized as follows:

- The tube's cross-sectional shape under static conditions went through gradual deformation from a perfect circle to a collapsed dumbbell shape with changes in transmural pressures. This result closely followed Shapiro's tube law.
- Under steady flow conditions, at lower  $\Delta P$ , the deformation trend induced by transmural pressure remained relatively independent of change in pressure difference, with no evidence of self-excited oscillations.
- As  $\Delta P$  increased beyond 43.0 mmHg, noticeable self-excited oscillations were triggered within a critical range of negative  $\Pi$  and a transition from chaotic to regular pattern has been observed.
- Both the frequency and amplitude of self-excited oscillations increased with the increment of negative  $\Pi$  and  $\Delta P$ . The amplitude of self-excited oscillation peaked around the middle of the critical  $\Pi$  range for each  $\Delta P$  case, indicating an optimal  $\Pi$  for maximum wall motion during self-excited oscillation.
- Critical velocity for the self-excited oscillation onset was  $0.3 \text{ ms}^{-1}$  in most of the cases. Additionally, using PIV results, peak velocity during self-excited oscillation was found up to  $1.2 \text{ ms}^{-1}$ .
- PIV analysis also revealed the periodic downstream jet during self-excited oscillation and this jet was not symmetrical.

During the pulsatile flow experiment, fluid-structure interaction phenomena were more complex due to the pressure waves traveling through the tube. In this segment, a wider range of transmural pressure ( $\Pi$ ) was applied to see how the collapsible tube responds to the change in transmural pressure.  $\Pi$  in this phase of the experiment is defined based on its mean value during a cycle. We also explored if there is any impact of reducing either the Reynolds number or flow frequency to half. Besides the quantitative analysis of collapsible tube deformation (axial plane) through optical measurement, PIV outcomes helped to observe the flow field including the traveling wave pattern, magnitude of the flow, local flow reversal, etc. Peak and mean flow rates throughout the experiment were recorded to examine if any limitation occurred under different conditions. Therefore, the key findings from pulsatile flow experiments are summarized below:

- Under significantly positive  $\Pi$ , the tube wall does not deform significantly but only shows slight vibrations due to flow pulsation. A brief negative pressure gradient was observed, indicating a local flow reversal at the beginning of the diastole phase.
- PIV results suggest that although early systolic flow was comparatively steady and laminar, peak and post-peak (decelerating) flow showed some unsteady wave-like flow patterns that vary from cycle to cycle.
- Near neutral (slightly positive)  $\Pi$  leads to symmetrical buckling of the tube during the diastolic phase. But before peak systole, flow pushes this collapse downstream and opens the tube fully at peak systolic flow.
- Under highly negative  $\Pi$ , the tube collapsed completely at the diastolic phase.

Though before the peak of systolic flow accelerated to push the collapse to open up, at peak systolic flow a “double throat” was observed. This unique deformation made

the flow accelerate followed by a rapid deceleration before reaching the maximum collapsed region downstream.

- Self-excited oscillation is triggered right after the peak systole during highly negative  $\Pi$ . This was evident from pulsation in downstream pressure and locally reversed flow.
- When Reynolds number was reduced to half under the same  $\Pi$  (near neutral), less deformation on the tube wall has been observed. The transition back to undeformed shape was more rapid.
- With the reduction in flow frequency and keeping  $\Pi$  same (near neutral), tube deformation was likely to remain similar, but the tube wall's deformation wave was faster than the flow.
- Both mean and peak flow rates during pulsatile flow cycles were independent of  $\Pi$  until  $\Pi > +10$ . Self-excited oscillation under negative  $\Pi$  ( $< -10$ ) increases the peak flow rates in collapsed tube conditions.

These results can explain the possible physiological significance of transmural pressure in veins and similar blood vessels. Changes in transmural pressure, such as bodily fluid shifts and muscle weight changes in microgravity, might be a factor impacting normal function in collapsible vessel fluid transport. The results and discussion have important implications for many other physiological fluid transportation phenomena, such as flow reversal in veins, self-excited oscillation in snoring and sleep apnea, etc. Furthermore, beyond these physiological explanations, this study can serve as a benchmark for future computational simulations in the fluid-structure interaction of collapsible tubes under both steady and pulsatile flow conditions.

## 5.2. Future Works

Future research can be designed to address some limitations encountered in the present research. First, a PDMS (Polydimethylsiloxane) tube has been employed as a simplified representation of human blood vessels. While the length and perimeter of the tube closely mimic those of large biological vessels, the material thickness and collapsibility were fixed in our experiment. The use of a variety of tube materials can help us understand more physiological conditions within specific blood vessels and contribute to a broader understanding of the physics underlying biological conditions.

During pulsatile flow experiments, flow reversal was observed within a critical range of transmural pressure, as evidenced by PIV results. Confirmation from downstream flowmeter readings would provide further substantiation in these scenarios. Although we were able to measure peak and averaged flow rates during pulsatile flow cycles, detecting backward flow and measuring reverse flow rates in the future will offer a more detailed understanding of flow reversal.

Improvement could also be made in terms of the PIV sampling rates. In the present study, the data was obtained at 15 frames per second. With higher repetition rate lasers and cameras, a time-resolved PIV measurement would help us understand more detailed fluid-structure interactions during each pulsatile cycle.

## REFERENCES

- [1] A. H. Shapiro, “Steady Flow in Collapsible Tubes,” *J. Biomech. Eng.*, vol. 99, no. 3, pp. 126–147, Aug. 1977, doi: 10.1115/1.3426281.
- [2] Y. Matsuzaki, “Self-excited Oscillation of a Collapsible Tube Conveying Fluid,” in *Frontiers in Biomechanics*, G. W. Schmid-Schönbein, S. L.-Y. Woo, and B. W. Zweifach, Eds., New York, NY: Springer New York, 1986, pp. 342–350. doi: 10.1007/978-1-4612-4866-8\_24.
- [3] F. P. Knowlton and E. H. Starling, “The influence of variations in temperature and blood-pressure on the performance of the isolated mammalian heart,” *J. Physiol.*, vol. 44, no. 3, pp. 206–219, May 1912, doi: 10.1113/jphysiol.1912.sp001511.
- [4] M. Heil and A. L. Hazel, “Fluid-Structure Interaction in Internal Physiological Flows,” *Annu. Rev. Fluid Mech.*, vol. 43, no. 1, pp. 141–162, 2011, doi: 10.1146/annurev-fluid-122109-160703.
- [5] “Congenital pulmonary veins atresia or stenosis - About the Disease - Genetic and Rare Diseases Information Center.” Accessed: Jan. 16, 2024. [Online]. Available: <https://rarediseases.info.nih.gov/diseases/4598/pulmonary-vein-stenosis>
- [6] M. Lan *et al.*, “Proposed mechanism for reduced jugular vein flow in microgravity,” *Physiol. Rep.*, vol. 9, no. 8, Apr. 2021, doi: 10.14814/phy2.14782.
- [7] J. B. Grotberg and O. E. Jensen, “Biofluid mechanics in flexible tubes.,” *Annu. Rev. Fluid Mech.*, vol. 36, no. 1, pp. 121–147, Jan. 2004, doi: 10.1146/annurev.fluid.36.050802.121918.
- [8] B. Gerber, J.-L. Singh, Y. Zhang, and W. Liou, “A computer simulation of short-term adaptations of cardiovascular hemodynamics in microgravity,” *Comput. Biol. Med.*, vol. 102, pp. 86–94, Nov. 2018, doi: 10.1016/j.combiomed.2018.09.014.
- [9] “Assessment of Jugular Venous Blood Flow Stasis and Thrombosis During Spaceflight | Cardiology | JAMA Network Open | JAMA Network.” Accessed: Feb. 13, 2024. [Online]. Available: <https://jamanetwork.com/journals/jamanetworkopen/fullarticle/2755307>
- [10] T. Nakada, I. Kwee, H. Igarashi, and Y. Suzuki, “Aquaporin-4 Functionality and Virchow-Robin Space Water Dynamics: Physiological Model for Neurovascular Coupling and Glymphatic Flow,” *Int. J. Mol. Sci.*, vol. 18, no. 8, p. 1798, Aug. 2017, doi: 10.3390/ijms18081798.
- [11] J. E. Flaherty, J. B. Keller, and S. I. Rubinow, “Post Buckling Behavior of Elastic Tubes and Rings with Opposite Sides in Contact,” *SIAM J. Appl. Math.*, vol. 23, no. 4, pp. 446–455, Dec. 1972, doi: 10.1137/0123047.



- [12] D. Elad, R. D. Kamm, and A. H. Shapiro, “Choking Phenomena in a Lung-Like Model,” *J. Biomech. Eng.*, vol. 109, no. 1, pp. 1–9, Feb. 1987, doi: 10.1115/1.3138636.
- [13] O. E. Jensen and T. J. Pedley, “The existence of steady flow in a collapsed tube,” *J. Fluid Mech.*, vol. 206, pp. 339–374, Sep. 1989, doi: 10.1017/S0022112089002326.
- [14] O. E. Jensen, “Instabilities of flow in a collapsed tube,” *J. Fluid Mech.*, vol. 220, pp. 623–659, Nov. 1990, doi: 10.1017/S0022112090003408.
- [15] P. Kozlovsky, U. Zaretsky, A. J. Jaffa, and D. Elad, “General tube law for collapsible thin and thick-wall tubes,” *J. Biomech.*, vol. 47, no. 10, pp. 2378–2384, Jul. 2014, doi: 10.1016/j.jbiomech.2014.04.033.
- [16] C. Tang, L. Zhu, G. Akingba, and X.-Y. Lu, “Viscous flow past a collapsible channel as a model for self-excited oscillation of blood vessels,” *J. Biomech.*, vol. 48, no. 10, pp. 1922–1929, Jul. 2015, doi: 10.1016/j.jbiomech.2015.04.011.
- [17] M. Laudato and M. Mihaescu, “Analysis of the contact critical pressure of collapsible tubes for biomedical applications,” *Contin. Mech. Thermodyn.*, Nov. 2023, doi: 10.1007/s00161-023-01271-3.
- [18] A. L. Hazel and M. Heil, “Steady finite-Reynolds-number flows in three-dimensional collapsible tubes,” *J. Fluid Mech.*, vol. 486, pp. 79–103, Jun. 2003, doi: 10.1017/S0022112003004671.
- [19] M. Heil and S. L. Waters, “How rapidly oscillating collapsible tubes extract energy from a viscous mean flow,” *J. Fluid Mech.*, vol. 601, pp. 199–227, Apr. 2008, doi: 10.1017/S0022112008000463.
- [20] C. D. Bertram and N. S. J. Elliott, “Flow-rate limitation in a uniform thin-walled collapsible tube, with comparison to a uniform thick-walled tube and a tube of tapering thickness,” *J. Fluids Struct.*, vol. 17, no. 4, pp. 541–559, Mar. 2003, doi: 10.1016/S0889-9746(02)00160-3.
- [21] C. D. Bertram and K. S. A. Butcher, “Possible Sources of Discrepancy Between Sphygmomanometer Cuff Pressure and Blood Pressure Quantified in a Collapsible-Tube Analogue,” *J. Biomech. Eng.*, vol. 114, no. 1, pp. 68–77, Feb. 1992, doi: 10.1115/1.2895452.
- [22] N. Gavriely, T. R. Shee, D. W. Cugell, and J. B. Grotberg, “Flutter in flow-limited collapsible tubes: a mechanism for generation of wheezes,” *J. Appl. Physiol. Bethesda Md* 1985, vol. 66, no. 5, pp. 2251–2261, May 1989, doi: 10.1152/jap.1989.66.5.2251.
- [23] C. D. Bertram and J. Tscherry, “The onset of flow-rate limitation and flow-induced oscillations in collapsible tubes,” *J. Fluids Struct.*, vol. 22, no. 8, pp. 1029–1045, Nov. 2006, doi: 10.1016/j.jfluidstructs.2006.07.005.

- [24] S. Bassez, P. Flaud, and M. Chauveau, “Modeling of the Deformation of Flexible Tubes Using a Single Law: Application to Veins of the Lower Limb in Man,” *J. Biomech. Eng.*, vol. 123, no. 1, pp. 58–65, Feb. 2001, doi: 10.1115/1.1336143.
- [25] H.-J. Wu, L.-B. Jia, and X.-Z. Yin, “Experiments on self-excited oscillation in a thin-walled collapsible tube,” *Acta Mech. Sin.*, vol. 31, no. 6, pp. 817–826, Dec. 2015, doi: 10.1007/s10409-015-0465-y.
- [26] A. Podoprosvetova, J. Zayko, V. Yushutin, and V. Vedeneev, “Experimental study of the flow regime effect on the stability of collapsible tubes conveying fluid,” *Phys. Fluids*, vol. 33, no. 6, p. 064104, Jun. 2021, doi: 10.1063/5.0050745.
- [27] R.-Q. Wang, T. Lin, P. Shamsheery, and A. G. Winter V., “Control of Flow Limitation in Flexible Tubes,” *J. Mech. Des.*, vol. 139, no. 013401, Oct. 2016, doi: 10.1115/1.4034672.
- [28] M. Heil and S. L. Waters, “Transverse flows in rapidly oscillating elastic cylindrical shells,” *J. Fluid Mech.*, vol. 547, pp. 185–214, Jan. 2006, doi: 10.1017/S0022112005007214.
- [29] C. D. Bertram, C. J. Raymond, and T. J. Pedley, “Mapping of instabilities for flow through collapsed tubes of differing length,” *J. Fluids Struct.*, vol. 4, no. 2, pp. 125–153, Mar. 1990, doi: 10.1016/0889-9746(90)90058-D.
- [30] C. D. Bertram, N. K. Truong, and S. D. Hall, “PIV Measurements of the Flow Field Just Downstream of an Oscillating Collapsible Tube,” *J. Biomech. Eng.*, vol. 130, no. 6, p. 061011, Dec. 2008, doi: 10.1115/1.2985071.
- [31] S. Kobayashi, D. Tang, and D. N. Ku, “Collapse in High-Grade Stenosis during Pulsatile Flow Experiments,” *JSME Int. J. Ser. C*, vol. 47, pp. 1010–1018, Jan. 2004, doi: 10.1299/jsmec.47.1010.
- [32] M. A. F. Zarandi, K. Garman, J. S. Rhee, B. T. Woodson, and G. J. M. Garcia, “Effect of tube length on the buckling pressure of collapsible tubes,” *Comput. Biol. Med.*, vol. 136, p. 104693, Sep. 2021, doi: 10.1016/j.compbiomed.2021.104693.
- [33] A. L. Hazel and M. Heil, “Three-dimensional airway reopening: the steady propagation of a semi-infinite bubble into a buckled elastic tube,” *J. Fluid Mech.*, vol. 478, pp. 47–70, Mar. 2003, doi: 10.1017/S0022112002003452.
- [34] G. S. Krenz and C. A. Dawson, “Flow and pressure distributions in vascular networks consisting of distensible vessels,” *Am. J. Physiol.-Heart Circ. Physiol.*, vol. 284, no. 6, pp. H2192–H2203, Jun. 2003, doi: 10.1152/ajpheart.00762.2002.
- [35] A. N. Gent, “On the Relation between Indentation Hardness and Young’s Modulus,” *Rubber Chem. Technol.*, vol. 31, no. 4, pp. 896–906, Sep. 1958, doi: 10.5254/1.3542351.

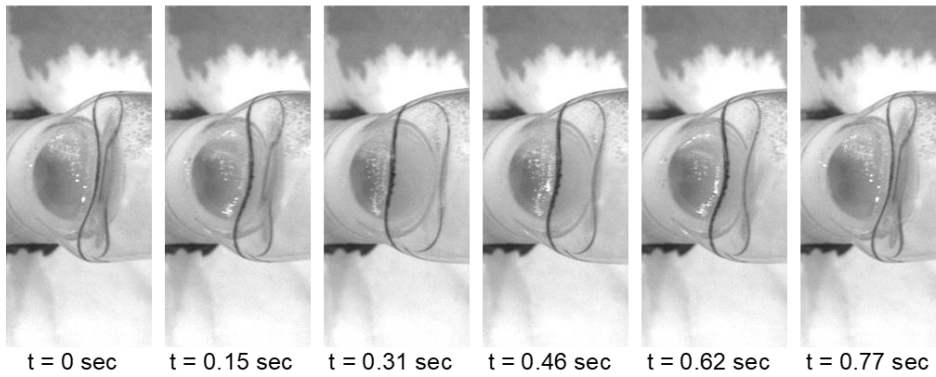
- [36] K. Larson, “Can You Estimate Modulus From Durometer Hardness for Silicones? Yes, but only roughly ... and you must choose your modulus carefully!,” Sep. 2017.
- [37] R. Zhang, “Experimental Studies of Pulsatile Flow Characteristics of Aortic Models under Normal and Diseased Conditions,” 2021, Accessed: Feb. 13, 2024. [Online]. Available: <https://library.ndsu.edu/ir/handle/10365/32359>
- [38] M. Klarhöfer, B. Csapo, Cs. Balassy, J. C. Szeles, and E. Moser, “High-resolution blood flow velocity measurements in the human finger,” *Magn. Reson. Med.*, vol. 45, no. 4, pp. 716–719, Apr. 2001, doi: 10.1002/mrm.1096.
- [39] “Pressure and Blood Flow.” Accessed: Jan. 16, 2024. [Online]. Available: <https://archive.math.arizona.edu/maw1999/blood/pressure.html>
- [40] “Elastic Properties of Blood Vessels - Arteries and Veins - The Cardiovascular System - Medical Physiology, 3rd Edition.” Accessed: Jan. 16, 2024. [Online]. Available: <https://doctorlib.info/physiology/medical/104.html>
- [41] “18.5C: Venous Blood Pressure,” Medicine LibreTexts. Accessed: Jan. 16, 2024. [Online]. Available: [https://med.libretexts.org/Bookshelves/Anatomy\\_and\\_Physiology/Anatomy\\_and\\_Physiology\\_\(Boundless\)/18%3A\\_Cardiovascular\\_System%3A\\_Blood\\_Vessels/18.5%3A\\_Systemic\\_Blood\\_Pressure/18.5C%3A\\_Venous\\_Blood\\_Pressure](https://med.libretexts.org/Bookshelves/Anatomy_and_Physiology/Anatomy_and_Physiology_(Boundless)/18%3A_Cardiovascular_System%3A_Blood_Vessels/18.5%3A_Systemic_Blood_Pressure/18.5C%3A_Venous_Blood_Pressure)
- [42] E. M. Gofur and B. Bordoni, “Anatomy, Head and Neck: Cerebral Blood Flow,” in *StatPearls*, Treasure Island (FL): StatPearls Publishing, 2023. Accessed: Jan. 16, 2024. [Online]. Available: <http://www.ncbi.nlm.nih.gov/books/NBK538134/>
- [43] K. Larry W., W. Jack, and C. David, *Physiology of Sport and Exercise 6th Edition*. Human Kinetics, 2015.
- [44] Y. Li, J. Sun, C.-K. Tang, and H.-Y. Shum, “Lazy snapping,” *ACM Trans. Graph.*, vol. 23, no. 3, pp. 303–308, Aug. 2004, doi: 10.1145/1015706.1015719.
- [45] Abraham. Savitzky and M. J. E. Golay, “Smoothing and Differentiation of Data by Simplified Least Squares Procedures,” *Anal. Chem.*, vol. 36, no. 8, pp. 1627–1639, Jul. 1964, doi: 10.1021/ac60214a047.
- [46] R. W. Schafer, “What Is a Savitzky-Golay Filter? [Lecture Notes],” *IEEE Signal Process. Mag.*, vol. 28, no. 4, pp. 111–117, Jul. 2011, doi: 10.1109/MSP.2011.941097.
- [47] E. Kresch and A. Noordergraaf, “Cross-sectional shape of collapsible tubes,” *Biophys. J.*, vol. 12, no. 3, pp. 274–294, 1972.
- [48] N. K. Truong and C. D. Bertram, “The flow-field downstream of a collapsible tube during oscillation onset,” *Commun. Numer. Methods Eng.*, vol. 25, no. 5, pp. 405–428,

May 2009, doi: 10.1002/cnm.1226.

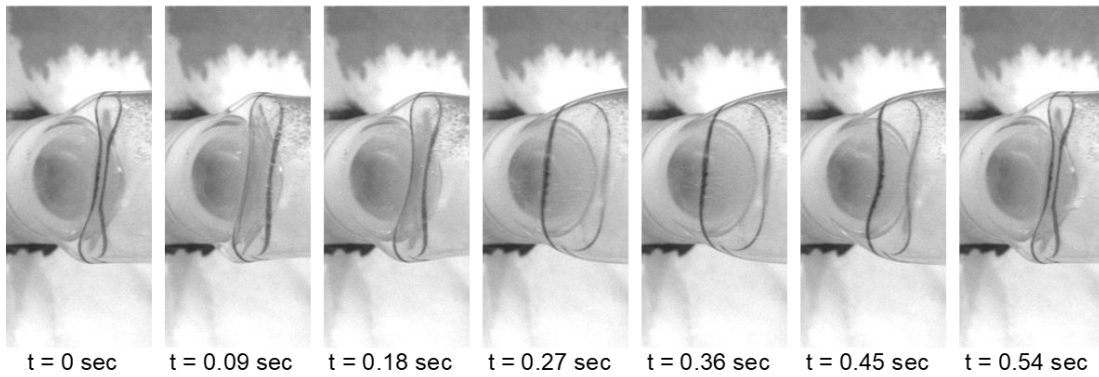
- [49] W. C. Hu, J. J. Wang, H. M. Tsao, and L. Y. Shyu, “Assessing the wall motion of pulmonary veins of the left atrium,” in *2008 Computers in Cardiology*, Sep. 2008, pp. 729–732. doi: 10.1109/CIC.2008.4749145.
- [50] X. He and D. N. Ku, “Unsteady entrance flow development in a straight tube,” *J. Biomech. Eng.*, vol. 116, no. 3, pp. 355–360, Aug. 1994, doi: 10.1115/1.2895742.
- [51] J. R. Womersley, “Method for the calculation of velocity, rate of flow and viscous drag in arteries when the pressure gradient is known,” *J. Physiol.*, vol. 127, no. 3, pp. 553–563, 1955, doi: 10.1113/jphysiol.1955.sp005276.
- [52] M. Lei, J. P. Archie, and C. Kleinstreuer, “Computational design of a bypass graft that minimizes wall shear stress gradients in the region of the distal anastomosis,” *J. Vasc. Surg.*, vol. 25, no. 4, pp. 637–646, Apr. 1997, doi: 10.1016/s0741-5214(97)70289-1.
- [53] D. N. Ku, “Blood Flow in Arteries,” *Annu. Rev. Fluid Mech.*, vol. 29, no. 1, pp. 399–434, 1997, doi: 10.1146/annurev.fluid.29.1.399.
- [54] B. Pier and P. J. Schmid, “Linear and nonlinear dynamics of pulsatile channel flow,” *J. Fluid Mech.*, vol. 815, pp. 435–480, Mar. 2017, doi: 10.1017/jfm.2017.58.
- [55] K. M. Saqr *et al.*, “Physiologic blood flow is turbulent,” *Sci. Rep.*, vol. 10, no. 1, Art. no. 1, Sep. 2020, doi: 10.1038/s41598-020-72309-8.
- [56] P. Zamboni, “Why Current Doppler Ultrasound Methodology Is Inaccurate in Assessing Cerebral Venous Return: The Alternative of the Ultrasonic Jugular Venous Pulse,” *Behav. Neurol.*, vol. 2016, p. e7082856, Feb. 2016, doi: 10.1155/2016/7082856.

## APPENDIX. RAW IMAGES DURING STEADY AND PULSATILE FLOW

$\Pi = -30$



$\Pi = -52$



$\Pi = -78$

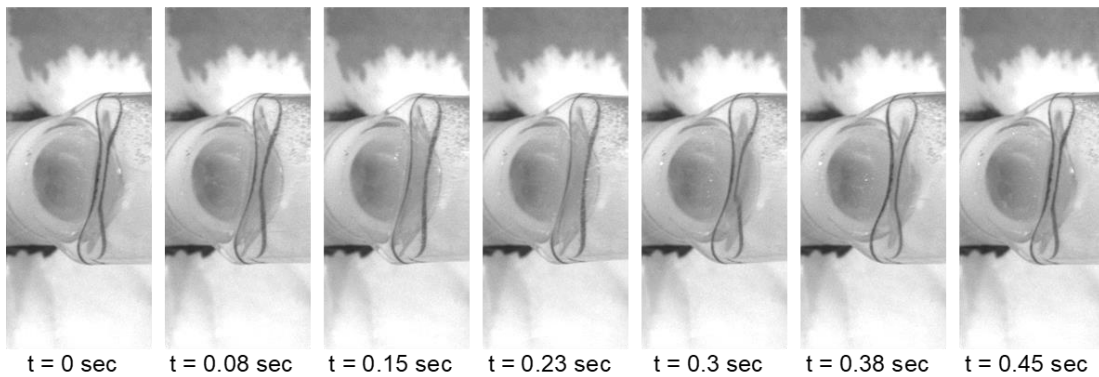


**Figure A1.** Images of the radial cross-section of the collapsible tube during the first cycle of self-excited oscillations at case 10 ( $\Delta P = 98$  mmHg) when  $\Pi = -30, -52$  &  $-78$  correspondingly from top to down.

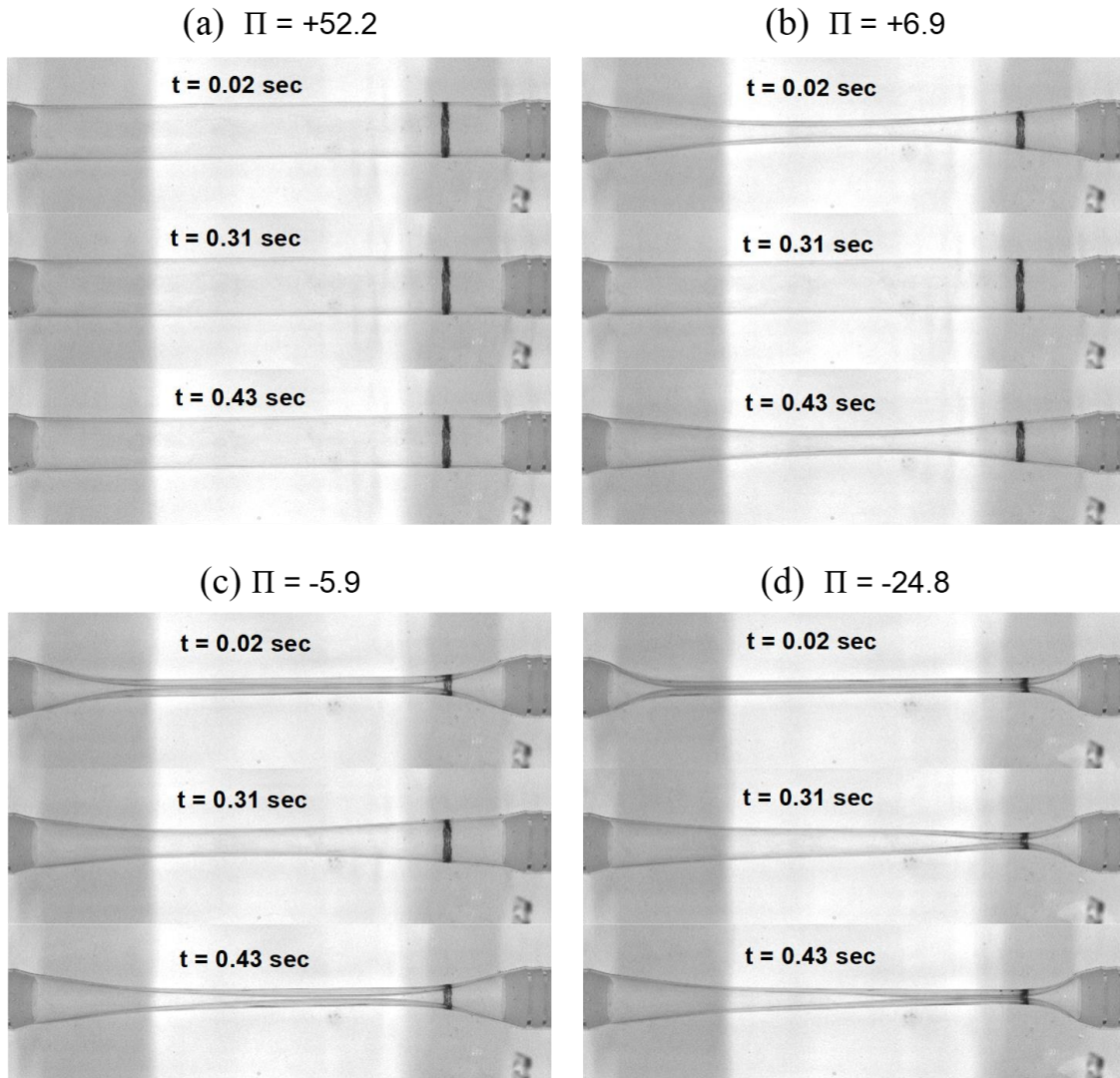


**Figure A2.** Pulsatile flow-induced tube collapsing at three different times of the cycle of baseline case for (a) Positive  $\Pi$ ; (b) Slightly positive  $\Pi$  (c) Slightly negative  $\Pi$ ; (d) Negative  $\Pi$ .

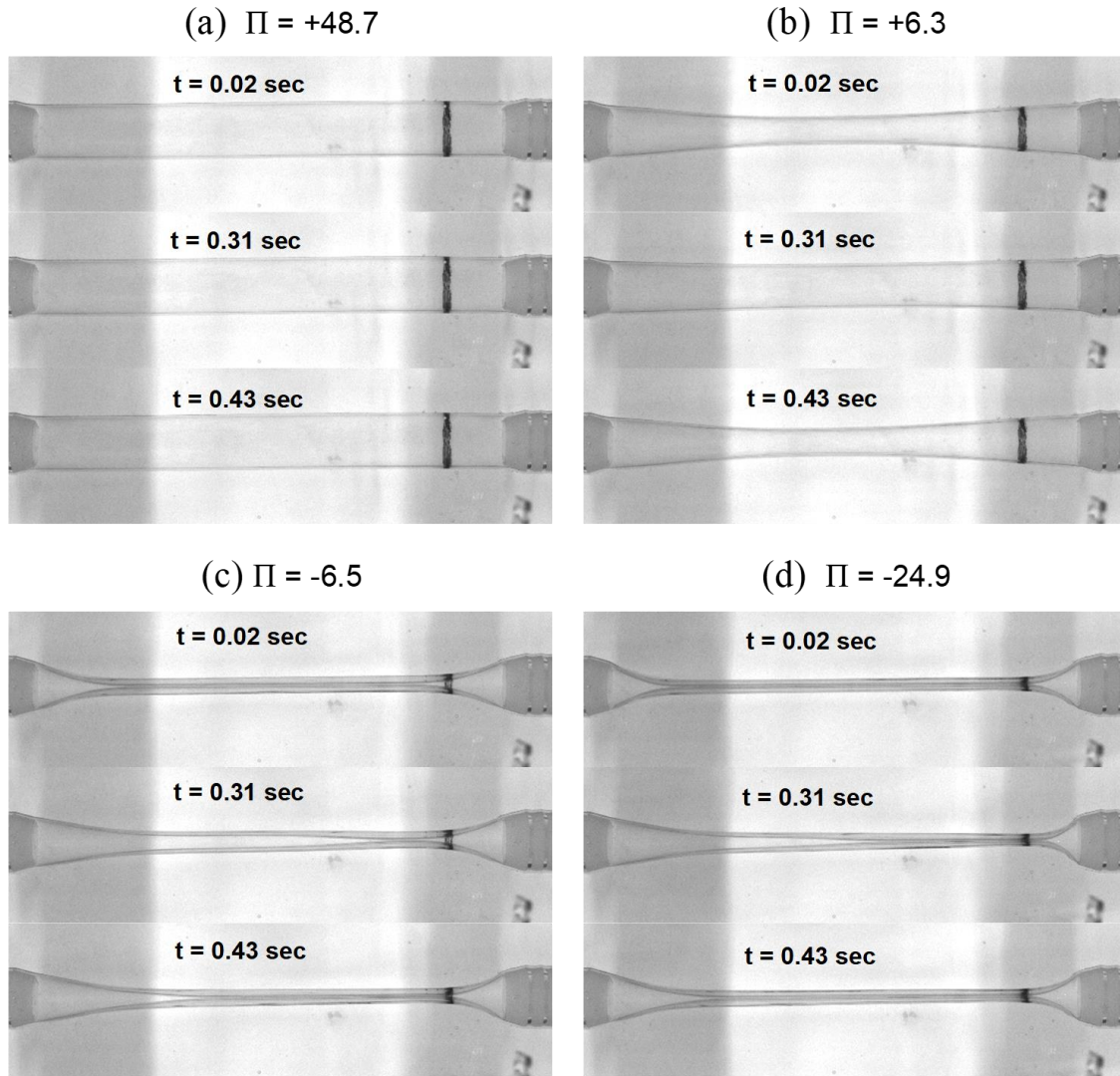


**Figure A3.** Pulsatile flow-induced tube collapsing at three different times of a cycle of half Re case for (a) Positive  $\Pi$ ; (b) Slightly positive  $\Pi$  (c) Slightly negative  $\Pi$ ; (d) Negative  $\Pi$ .



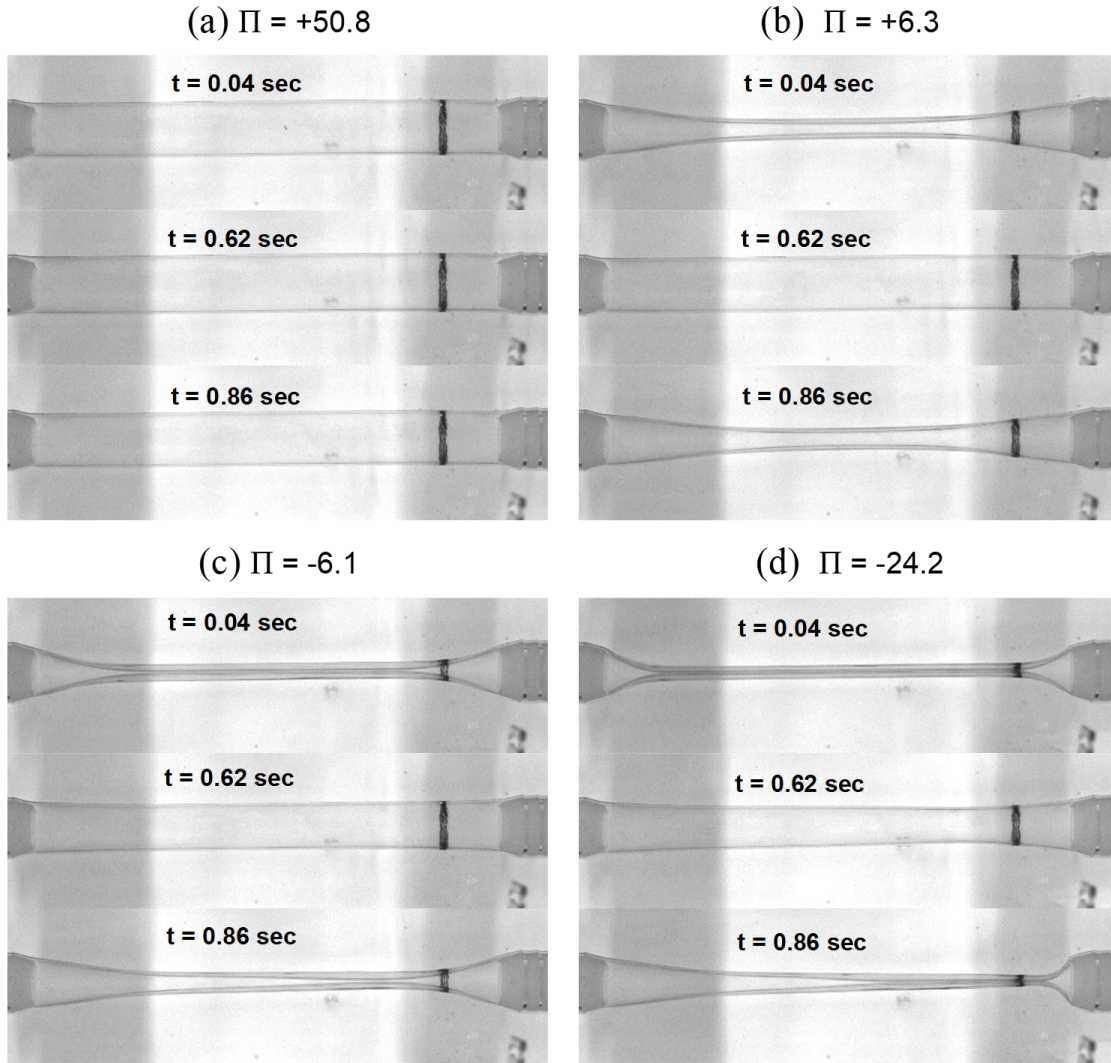


**Figure A4.** Pulsatile flow-induced tube collapsing at three different times of a cycle of half frequency (reduced  $Wo$  number) case for (a) Positive  $\Pi$ ; (b) Slightly positive  $\Pi$  (c) Slightly negative  $\Pi$ ; (d) Negative  $\Pi$ .